

4343



JNCASR  
621.381 528 4 P06



LIBRARY  
AWAHARLAL NEHRU CENTRE  
ADVANCED SCIENTIFIC RESEARCH  
JAKKUR POST  
BANGALORE - 560 064

**Polymer Field-Effect Transistors:  
Electrical Transport Properties and  
Studies of Photoinduced Charge Generation  
and Relaxation Processes**

**A Thesis Submitted in Partial Fulfillment of**

**The Requirements of The Degree of**

**Doctor of Philosophy**

**By**

**Soumya Dutta**




**Chemistry and Physics of Materials Unit  
Jawaharlal Nehru Centre for Advanced Scientific Research  
Bangalore 560 064 (INDIA)**

**March 2006**

To My Parents

## **Declaration**

I hereby declare that the thesis entitled “Polymer Field-Effect Transistors: Electrical Transport Properties and Studies of Photoinduced Charge Generation and Relaxation Processes” is an authentic record of research work carried out by me under the supervision of Prof. K. S. Narayan at the Molecular Electronics Lab, Chemistry and Physics of Materials Unit, Jawaharlal Nehru Centre for Advanced Scientific Research, Bangalore, India. The thesis has not previously formed the basis for the award of any Degree, Diploma, Associateship or Fellowship.



Soumya Dutta



**JAWAHARLAL NEHRU CENTRE FOR ADVANCED SCIENTIFIC RESEARCH**  
Jakkur, Bangalore 560064, India

**K. S. NARAYAN**

**PHONE:** 91 80 2208 2822  
**FAX:** 91 80 2208 2766  
**e-mail:** narayan@jncasr.ac.in

---

March 22<sup>nd</sup> 2006

## **Certificate**

Certified that the work described in this thesis titled "Polymer Field-Effect Transistors: Electrical Transport Properties and Studies of Photoinduced Charge Generation and Relaxation Processes" has been carried out under my supervision at the Molecular Electronics Lab, Chemistry and Physics of Materials Unit, Jawaharlal Nehru Centre for Advanced Scientific Research, Bangalore, India.

**Prof. K. S. Narayan**

---

## Acknowledgement

An endeavor such as researching and writing a Ph. D thesis cannot be completed by lone effort. There are several people who have contributed from different perspectives to assemble the piece of knowledge as presented in the form of this thesis. I would like to take this opportunity to acknowledge all those people for their indispensable supports.

First of all, I wish to express my sincere gratitude to my advisor Prof. K. S. Narayan for introducing me to such a challenging and topical field of research. His constant guidance, advice, encouragement, invaluable suggestions, piece of patience and trust have not only inspired me but also heightened my confidence in thinking the scientific problems independently. I also intend to express my sincere thanks to his family members who were equally supportive towards me during my stay in JNCASR.

I would like to thank Prof. C. N. R. Rao, FRS, Chairman of CPMU, JNCASR for providing a beautiful scientific atmosphere and tremendous facilities to conduct research work.

I owe my whole-hearted thanks to the present lab mates Dr. Vasuda, Dinesh, Arun, Dhritiman, Manohar and Hemanth for their restless support in all the way. I also thank to the past lab mates Dr. Alagiriswami, Dr. A. G. Manoj, Dr. B. Singh, Basavaraj, Ravi Kumar and Sajini for exchanging their own expertise to help me.

I am highly indebted to Prof. G. Horowitz (France), Prof. F. Biscarini (Italy) and Prof. G. Lanzani (Italy) for their hospitality and several scientific and non-scientific discussions during my stay in Europe. I would like to extend my gratitude to all the faculties of CPMU and TSU for their favorable assistance. I am also grateful to both Dr. K. K. Ghosh (Kolkata, West Bengal) and Dr. A. K. Bhattacharya (Burdwan, West Bengal) for their affectionate support to build my research mind and scientific attitude.

I wish to convey my appreciation to all the friends in JNCARS, IISc and abroad for providing unforgettable accompany and moral support during

## **Acknowledgement**

different stages of my Ph. D tenure. I thank to Dr. A. Ranganathan for her patience to do partial correction of the thesis. I also acknowledge the Administrative staff, Academic staff, and the Technical Staff for helping me with their respective field of expertise.

I would like to express my deep sense of gratitude to my parents and family members for their tremendous support and inspiration to maneuver the whole. Finally, I must express my deepest appreciation to my wife Aparna. Without her constant encouragement, inspiration, and enthusiasm, it would never be possible to be what I am.

---

## Preface

The thesis focuses on the electrical properties and photoinduced processes in polymer based field-effect transistors PFETs. The photoinduced drain current in the PFETs results from a variety of possible pathways, and is a consequence of a complex charge generation, recombination and transport processes. These processes are observed to be dependent on the gate voltage and demonstrate a coupling between the photoexcitation and transistor features.

Considerable increase in drain current upon irradiation, followed by an extremely slow relaxation upon terminating the illumination is the striking feature in poly(3-hexylthiophene) based transistor operated under accumulation mode. The time dependent photoresponse along with gate voltage dependence is studied over a wide temperature range. The relaxation of photoinduced current is modeled in terms of a sequential, hierarchical statistical process. These results are physically interpreted on the basis of spatial separation of charge carriers and governed by characteristic trap distributions. The more mobile excess positive charges (holes) drift towards the channel, whereas the nearly immobile excess negative charges (electrons) are trapped in the bulk, immediately after the generation, maintaining a distribution. Upon turning off the light source, the more mobile holes recombine with the trapped electrons resulting in a progressive slow process.

In depletion mode, the photoresponse becomes strongly dependent on gate voltage. Low dark current in the background, accompanied by large photosensitivity in this mode is exploited to observe memory effect including write, read, store and erase operations. The optoelectronic processes can then be explained on the basis of photogeneration of charge carriers, largely within the depleted region along with highly reduced cross section of recombination in the high field region. The effects of light intensity, duration of light-exposure and temperature on the memory effect are also investigated.

The unique combination of gate bias and light as input parameters for charge transport in polymer transistor is evident in the spectroscopic studies of

## **Preface**

---

the drain current in PFET structure. The measurement and analysis of the results, obtained from light incident from the top and bottom side of the transparent gated-device are carried out to provide spatial information of the gate voltage dependent photocarrier generation region.



---

---

## Table of Contents

<b>Dedication</b>	<b>i</b>
<b>Declaration</b>	<b>ii</b>
<b>Certificate</b>	<b>iii</b>
<b>Acknowledgement</b>	<b>iv</b>
<b>Preface</b>	<b>vi</b>
<b>Table of Contents</b>	<b>viii</b>
<b>1 Introduction.....</b>	<b>1</b>
1.1 Historical Background.....	1
1.2 Charge-Transport Properties of Conjugated Polymers.....	5
1.2.1 Quasiparticles as Charge Carriers.....	6
1.2.2 Doping in Conjugated Polymers.....	9
1.2.3 Hopping Transport.....	10
1.2.4 Trap Limited Transport.....	15
1.3 Photoconduction in Conjugated Polymers.....	18
1.3.1 Exciton Formation.....	19
1.3.2 Exciton Transport.....	22
1.3.3 Exciton Dissociation.....	23
1.4 Optoelectronic Device Perspectives.....	27
1.4.1 Photodetectors, Photovoltaics, Solar Cells.....	27
1.4.2 Organic Light Emitting Devices (OLEDs).....	29
1.4.3 Organic Field-Effect Transistors (OFETs).....	30
1.5 Motivation.....	31
<b>2 Organic/Polymer Field-Effect Transistors.....</b>	<b>33</b>
2.1 Introduction.....	33
2.2 Device Operation and Electrical Characterization.....	33

## Table of Contents

---

2.2.1	Basic Requirement for OFET.....	34
2.2.2	Qualitative Description of Transistor Operation.....	35
2.2.3	Theoretical Modeling of Transistor characteristics.....	39
2.2.4	Conductivity Versus Mobility.....	44
2.2.5	Concept of Threshold Voltage and Switch-on Voltage....	45
2.2.6	Field-Effect Mobility Versus Bulk Mobility.....	46
2.2.7	Dependence of Field-Effect Mobility on Gate Voltage and Temperature.....	48
2.2.8	Nature of Self-localized Charge Carriers in PFETs.....	50
2.3	Device Fabrication.....	53
2.3.1	Deposition of Semiconductors.....	54
2.3.2	Deposition of Metals and Their Role in Electrical Performance.....	57
2.4	Progress in Electrical Performance of OFET.....	59
2.4.1	Progress in <i>p</i> -channel OFETs.....	59
2.4.2	Progress in <i>n</i> -channel OFETs.....	62
2.4.3	Progress in Ambipolar OFET.....	63
<b>3</b>	<b>Materials, Fabrication and Measurements.....</b>	<b>67</b>
3.1	Introduction.....	67
3.2	Materials.....	67
3.2.1	Poly(3-hexylthiophene) (P3HT).....	67
3.2.2	Polyvinyl alcohol (PVA).....	71
3.2.3	Hexamethyldisilazane (HMDS).....	72
3.3	Fabrication Method.....	73
3.4	Measurements.....	75
3.4.1	Absorption Coefficient Measurement.....	75
3.4.2	Transistor Output Characteristics and Transfer Characteristics.....	76
3.4.3	Capacitance-Voltage Measurements.....	77
3.4.4	Transient Photocurrent Measurements.....	77

3.4.5	Intensity Modulated Photocurrent Spectrum (IMPS).....	79
3.4.6	Optical Microscopy and Electron Microscopy.....	80
3.4.7	X-ray Diffraction (XRD) and Grazing Incidence X-ray Diffraction (GIXRD) Measurements.....	80
<b>4</b>	<b>Slow Relaxation of Photoinduced Drain Current in PFET.....</b>	<b>81</b>
4.1	Introduction.....	82
4.2	Dark Characteristics of Polymer Field-Effect Transistors.....	82
4.2.1	Output and Transfer Characteristics of Polymer Field-Effect Transistors.....	82
4.3	Photoinduced Modulation of Transistor Characteristics.....	85
4.3.1	Photoresponse of Polymer Field-Effect Transistors at Low Temperature.....	85
4.3.2	Slow Relaxation of Photoinduced Conductance in PFET.....	87
4.3.3	Inappropriateness of Stretched Exponential Decay Law in PFET.....	90
4.3.4	Experimental Verification of Charge Dynamics in PFET.....	92
4.3.5	Model of Spatial Charge Separation.....	92
4.3.6	Importance and Gate Bias Dependence of Fitting Parameters.....	97
4.3.7	Build-up of Photoinduced Charge Carriers in PFET.....	98
4.3.8	Photoresponse of PFET under Short Pulse Mode.....	99
4.3.9	Validity and Limitation of the Model of Spatial Charge Separation.....	100
4.4	Summary.....	102

## Table of Contents

---

<b>5</b>	<b>Optoelectronic Memory Effect in PFET.....</b>	<b>103</b>
5.1	Introduction.....	103
5.2	Memory Effect in Transistor Under Depletion mode.....	104
5.2.1	Photoinduced Charge Dynamics in Depleted Transistor.....	104
5.2.2	Memory Operation in Polymer Field-Effect Transistor.....	105
5.2.3	Qualitative Description of Memory Effect.....	106
5.2.4	Dependence of Memory Effect on Light Intensity.....	112
5.2.5	Dependence of Memory Effect on Duration of Light Pulse.....	114
5.2.6	Effect of Temperature on Memory Effect.....	115
5.2.7	Equivalence of Metastable State and Accumulation Mode.....	116
5.2.8	Absence of Memory Effect in Accumulation Mode.....	117
5.3	Comparison Between the Photoinduced Charge Distribution in Different Modes of Transistor.....	118
5.4	Summary.....	121
<b>6</b>	<b>Photocurrent Spectroscopy in PFET.....</b>	<b>123</b>
6.1	Introduction.....	123
6.2	Spectral Response of Photocurrent at Low Temperature.....	123
6.2.1	Photocurrent Spectrum for Different Gate Bias.....	124
6.2.2	Light Intensity Dependence of Modulated Photocurrent.....	126
6.3	Spectral Response of Photoinduced Drain Current at Room Temperature.....	127
6.3.1	Photoinduced Effect versus Bolometric Effect.....	127
6.3.2	Photocurrent Spectrum of Top-illuminated Polymer Field-Effect Transistor.....	129

6.3.3	Effect of Modulating Frequency and Gate Voltage on Photocurrent Spectrum.....	131
6.3.4	Photocurrent Spectrum of Bottom-illuminated Polymer Field-Effect Transistor.....	133
6.4	Photocurrent Spectroscopy in Transparent-Gated Photo-FET.....	134
6.4.1	Photocurrent Spectrum of Transparent PFET for Top-illumination.....	135
6.4.2	Photocurrent Spectrum of Transparent PFET for Bottom-illumination.....	136
6.4.3	Estimation of Depletion Width and Associated Electric Field from Spectral Analysis.....	137
6.4.4	Resolved Spectral Features of Photocurrent in Depletion Mode.....	140
6.4.5	Simulated Photocurrent Spectrum in Depletion Mode and Analysis.....	142
6.5	Summary.....	143
<b>7</b>	<b>Summary and Future Directions.....</b>	<b>145</b>
	<b>Bibliography.....</b>	<b>149</b>
	<b>List of Publications.....</b>	<b>161</b>

# Chapter 1

## Introduction

### 1.1 HISTORICAL BACKGROUND

Over the couple of decades, conventional insulating polymers (“plastics”) have traditionally been emerged as substitutes for structural materials like wood, ceramics etc. and also as materials for electrical insulation. Since the first report of doping in conjugated polymer providing metallic conductivity, the subject has evolved and grown encompassing several phenomena and applications [1–3]. At present, the studies of conjugated and conducting polymer-based electronics have a stage not only from the viewpoint of fundamental understanding but also from the technological standpoint. The overall progress of plastic electronics is largely motivated due to inexpensive manufacturing process, facile processing technique, chemical tenability, flexibility and large area processing advantages.

The ability to synthesize a variety of conjugated polymers, which are soluble in easily-handled solvents, has boosted the possibilities of device fabrication and electronic applications [4–6]. The promising mechanical properties along with equally accessible optical and electronic properties of conjugated polymers have really been explored after the invention of organic light emitting diode (OLED) [7,8] and organic field effect transistor (OFET) [9–11]. Following these major breakthroughs, a large number of research has been conducted from their individual device perspectives [12,13] to the integrated transistor-driven display technology [14–16]. The solution processibility of conjugated polymers enabling the use of polymer blends as active materials has been largely exploited in the development of photodetector (PD) [17–20], photovoltaic (PV) [21] and solar cell [7,22]. Recent advancement of polymer electronics has offered extensive outcomes such as prototype all-polymer integrated circuits (ICs) [23], printing technology based flexible FETs [24,25], light emitting FETs [26], memory device [27], active matrix flat panel

## 2 / Introduction

displays (AMFPDs) etc. More recently, several challenges such as organic sensors [28], low-end smart cards, radio-frequency identification (RFID) tags [29] etc. have been proposed to extrapolate the commercial interest.

Conjugated polymers fall in the category of organic macromolecules, which at least consist of one backbone chain with alternating double- and single-bonds. The electronic properties of conjugated polymers differ from the conventional saturated polymer due to different hybridization schemes. According to the molecular orbital theory, when two atoms bond to form a molecule, the atomic orbitals overlap forming bonding (lower energy) and antibonding (higher energy) orbitals. The probability of electron-occupancy of these molecular orbitals is governed by Pauli's exclusion principle. In the ground state, electrons occupy the bonding orbital, which is also called the highest occupied molecular orbital (HOMO). On the other hand, the

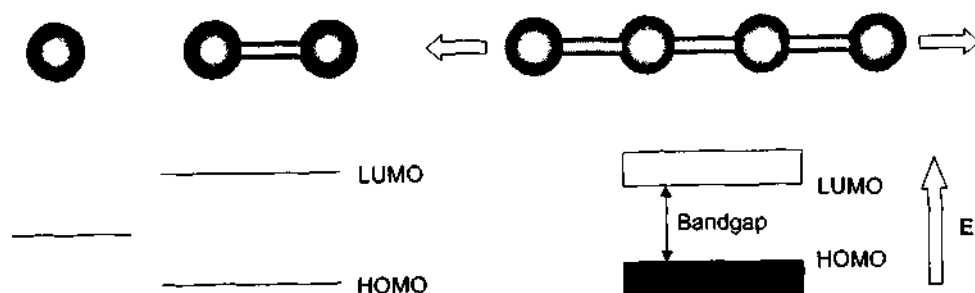


Fig. 1.1 Classical band picture: from a single isolated atom to polymer chain.

antibonding orbital, called the lowest unoccupied molecular orbital (LUMO), becomes empty. The intermolecular interactions in long polymer chain lead to further splitting of each molecular orbital resulting the formation of narrow bands, as shown in Fig. 1.1. The energy gap between the HOMO and LUMO provides the information related to primary excitation of the material.

The electronic structure of carbon (C) is represented as  $1s^2 2s^2 2p^2$ , which becomes  $1s^2 2s^1 2p_x^1 2p_y^1 2p_z^1$  by promotion of one of the 2s electrons to the 2p orbital. In case of a single-bonded polymer chain (e.g. polyethylene), the four outer orbitals of C atom become equivalent and combine with the four nearest

neighbors by strong, directed  $\sigma$ -bonds forming a tetrahedral  $sp^3$  hybrid structure (Fig. 1.2). In the simplest approximation, the transition of an electron from the

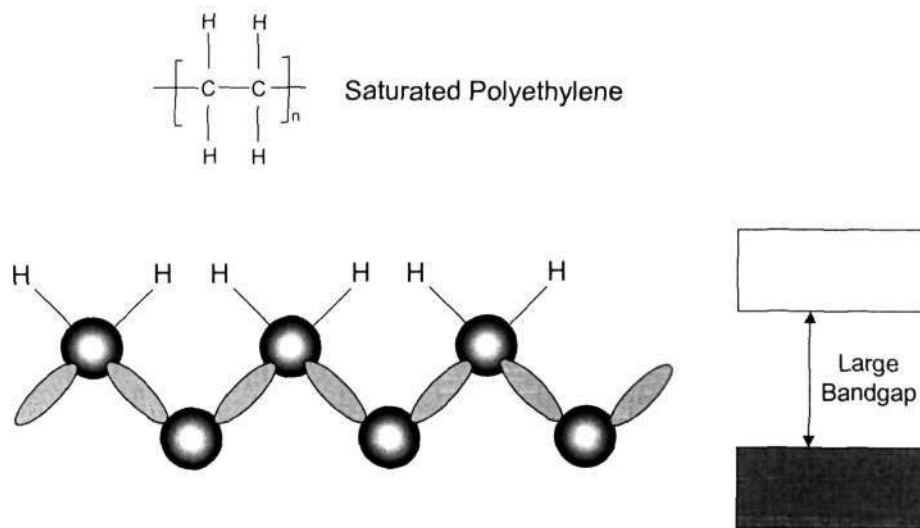


Fig. 1.2  $Sp^3$  hybridization in saturated polyethylene resulting large bandgap.

bonding orbitals to the corresponding antibonding orbitals requires large amount of excitation energy. This explains the reason why some polymers are insulators and they are transparent in the entire visible range of the spectrum. In case of a conjugated polymer, the C atoms are threefold coordinated (e.g. polyacetylene) leading to  $sp^2$  hybridization. Three equivalent orbitals  $2s^1 2p_x^1 2p_y^1$  bind with nearest neighbors creating three co-planar strong  $\sigma$ -bonds, directed  $120^\circ$  to each other. The remaining orbital  $2p_z^1$  of each C atom of the pair overlaps each other with comparatively weaker  $\pi$ -bond, in the direction perpendicular to the  $sp^2$  hybridized plane. Each  $\pi$ -bond splits into bonding and antibonding molecular orbitals, called the  $\pi$  and  $\pi^*$ , respectively. However, by considering the presence of one  $\pi$  electron per repeated CH unit, one may expect the material to behave like a quasi-one-dimensional metal with half-filled band, as displayed in Fig. 1.3. As pointed out by Peierls [30], a one-dimensional metal is highly unstable against a periodic lattice distortion leading to alternating bond lengths throughout, also called *dimerization*. This renders doubling of the unit cell and opens up a gap at the Fermi level depending on the



#### 4 / Introduction

difference of the bond lengths, as shown in Fig. 1.4 [31]. The origin of semiconducting properties of the conjugated polymers lies solely on the

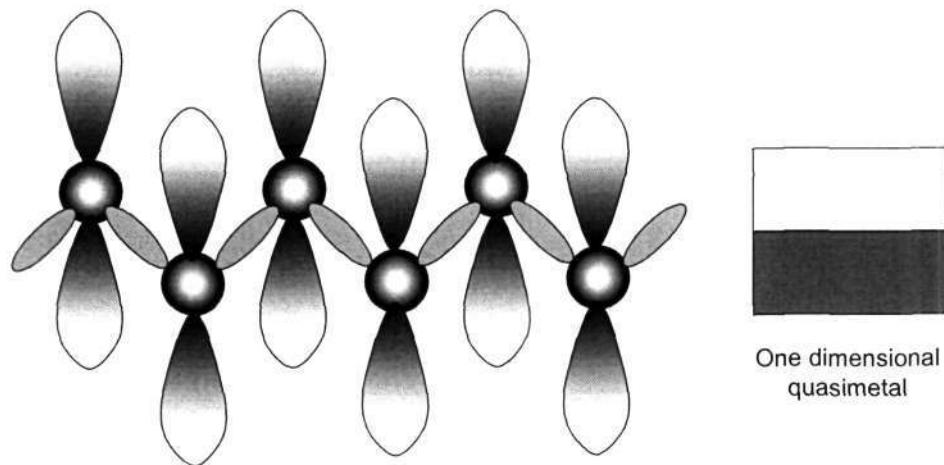


Fig. 1.3  $Sp^2$  hybridization in one-dimensional quasimetal.

existence of the extended  $\pi$  bands producing a HOMO-LUMO gap in the range 1–3 eV. This energy gap determines that most of the conjugated polymers can be excited by optical (visible - near infrared) or thermal excitation. Briefly, a conjugated polymer can be considered as a system consisting of in-plane

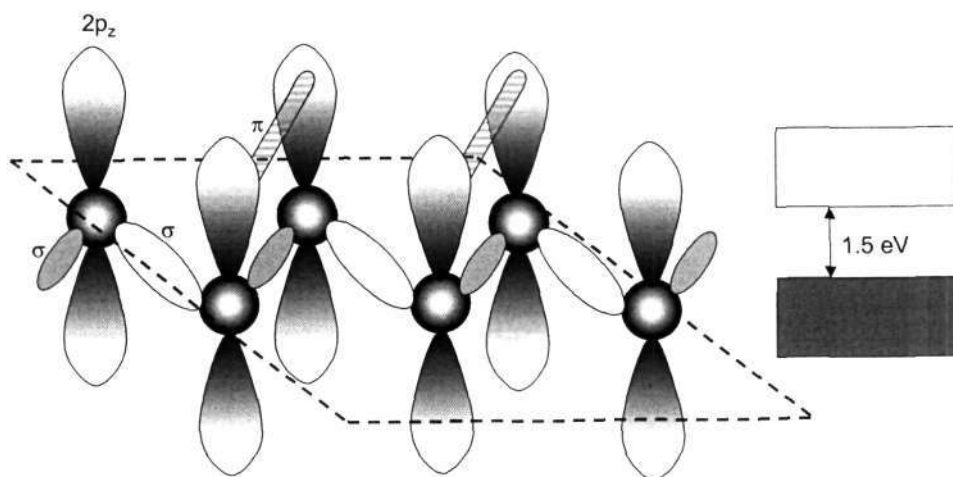
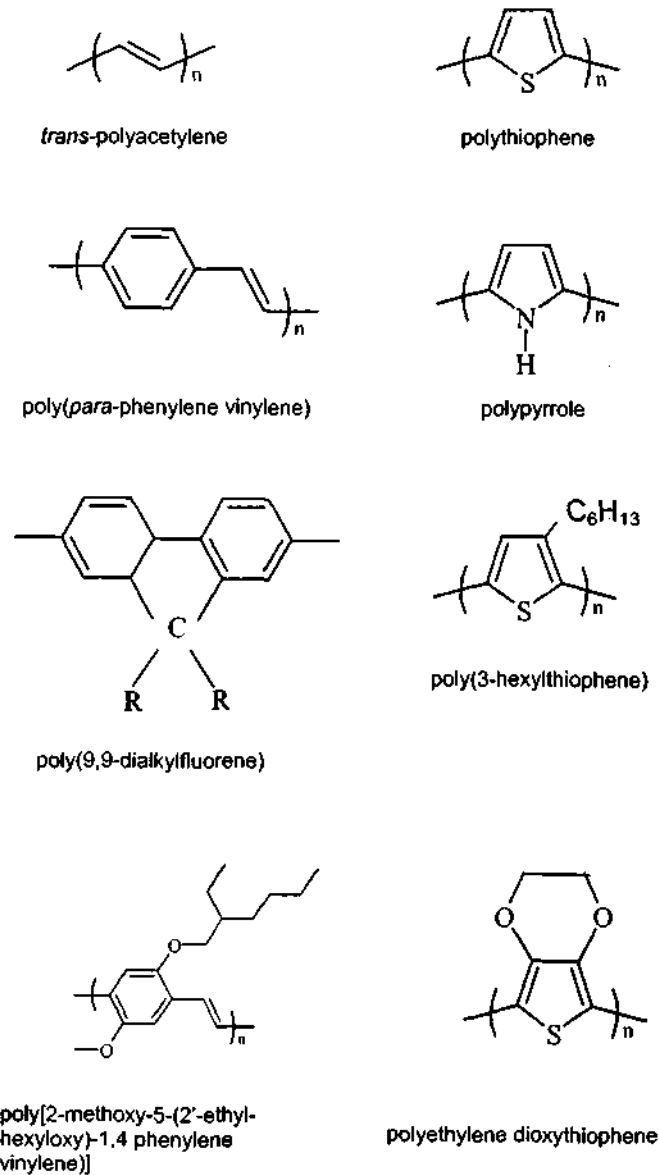


Fig. 1.4  $Sp^2$  hybridization with Peierls distortion in  $\pi$ -conjugated system.

skeleton provided by the three  $\sigma$  bonds, which bind the molecule intact. In addition, conjugation between the loosely bound  $\pi$ -electrons with  $p_z$  orbitals perpendicular to the molecular plane, provides a major contribution to the

transport process. A list of few important conjugated polymers with their molecular structure is displayed in Fig. 1.5.

## 1.2 CHARGE TRANSPORT PROPERTIES OF CONJUGATED POLYMERS



**Fig. 1.5** List of few important conjugated polymers with their schematic structure.

The charge transport process in conjugated polymers differ from that in conventional inorganic semiconductors such as Si, Ge, and GaAs. In case of conventional semiconductors, the atoms are held together with very strong

## 6 / Introduction

covalent bonds (e.g. energy as high as 76 Kcal/mol for Si), resulting charge transport through highly delocalized states. But the polymer systems are mainly based on weak intermolecular interaction forces (typically van der Waals interaction) with energy less than 10 Kcal/mol and having comparatively poor crystalline order. As a consequence, the charge transport in conjugated polymer predominantly takes place through hopping between localized states. This limits the room temperature mobility ( $\mu$ ) of the order of  $1 \text{ cm}^2 \text{ V}^{-1} \text{ s}^{-1}$  as compared to that of the traditional inorganic semiconductors (typically  $\sim 10^3 \text{ cm}^2 \text{ V}^{-1} \text{ s}^{-1}$  at room temperature). The primary difference between delocalized (also called band transport) and localized transport mechanisms lies on the temperature dependencies of carrier mobility. In band transport, mobility decreases with temperature due to phonon scattering, whereas in most of the organic semiconductors it increases with temperature as a consequence of phonon-assisted hopping transport.

### 1.2.1 Quasiparticles as Charge Carriers

The charge carriers in conjugated polymer have been interpreted in terms of self-localized excitations, which are quasi-particles with structural deformation over several repeating units. These excitations can be classified mainly into (i) *solitons* [32,33], (ii) *polarons* [34] and (iii) *bipolarons* [35], which directly contribute to charge transport in different cases.

(i) **Solitons:** In case of polymer with degenerate ground state, such as trans-polyacetylene, the order of single and double bonds can be interchanged without changing the energy. The double-degeneracy is removed due to symmetry-breaking at the bond-alteration domain wall, giving rise to the formation of a mid-gap state. This defect is known as *soliton*, which extends over few (5 – 10) monomer units separating two degenerate bond-alteration schemes. Three types of solitons can be considered depending on their charge and spin states. The deformation of polymer without any charge transfer (consisting of zero charge and spin  $\frac{1}{2}$  state) is known as neutral soliton. Upon addition or removal of electrons, a polymer chain undergoes structural distortion. This manifests spinless (spin 0) charged (negatively or positively) state and is referred to as the negative or positive soliton depending on the nature of charge state. Thus

solitons are expected to appear, only in degenerated ground state polymer, as

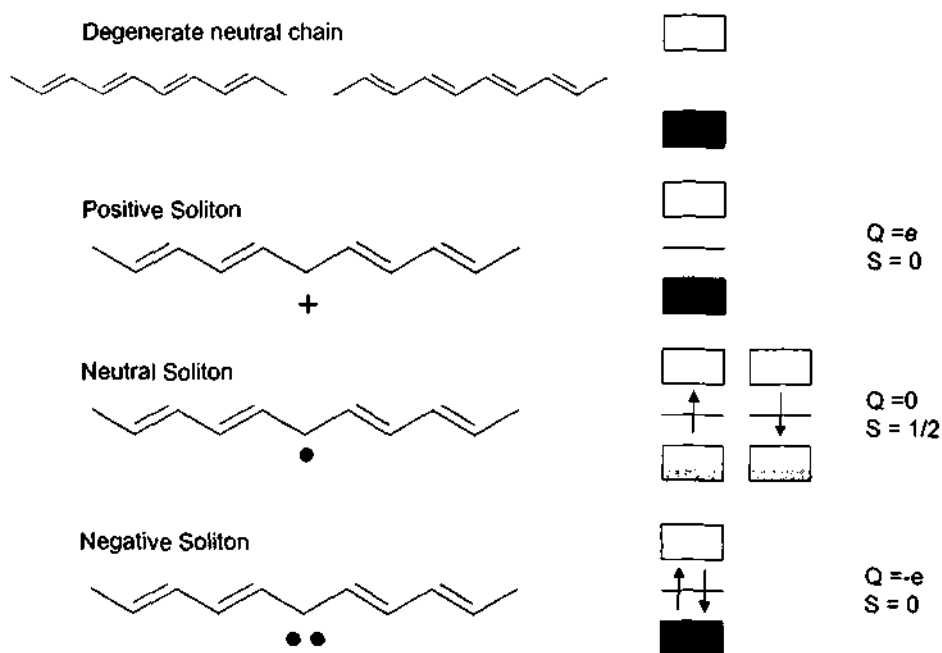


Fig. 1.6 Various types of *solitons* with their spin and charge state.

either spin-less charge or charge-less spin species. The existence of soliton (typically 400 solitons per  $10^6$  C-atoms) can be detected by electron spin resonance experiment [36]. Different types of solitons are displayed in Fig. 1.6.

(ii) **Polarons:** Upon doping the polymer, the excess isolated electron or hole is self-trapped within a time scale  $\sim 100$  femtoseconds, undergoing a deformation in the chain [34]. This deformation accompanied by the excess charge carriers is referred to as *polaron*, which contributes to the hopping transport in non-degenerated and degenerated conjugated polymers. The strong electron-phonon coupling is considered to be responsible for the formation of polarons in conjugated system. A polaron, which can travel along the polymer chain without changing its shape, can be represented by localized solitary waves. The size of the polaron, either of smaller radius or of larger radius, is determined by the strength of the electron-phonon coupling. These quasiparticles are classified as positive polaron or negative polaron according to the nature of charge carriers involved. The polarons are typically composed of

## 8 / Introduction

single-charged and  $\frac{1}{2}$  spin states. The existence of polarons can be identified by

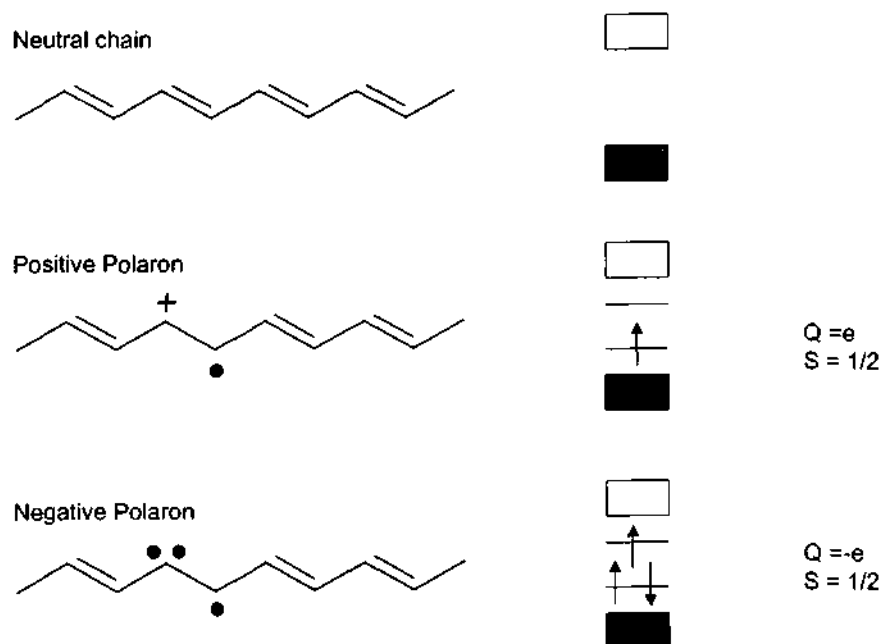


Fig. 1.7 Various types of *polarons* with their spin and charge state.

the two additional energy levels that are located symmetrically about the centre of the gap, as shown in Fig. 1.7. The chain length is considered to provide a strong impact in deciding the location of the energy levels with respect to HOMO and LUMO. The energy states belong to definite parity (even or odd) under the consideration that the conjugated system preserves inversion symmetry even when the side groups would tend to violate it. The transitions among the levels are governed by the selection rules, which require parity transformation between the concerned levels.

(iii) **Bipolarons:** In case of doped polymer with non-degenerated ground state, the conduction is observed to increase by several orders of magnitude without any appreciable change in magnetic susceptibility. Since the possibility of soliton formation can be ruled out in this case, the concept of a new quasiparticle with spinless and doubly charge is introduced. This is known as *bipolaron* and can be formed due to the binding state of two like charges with opposite spins in the same conjugation length. In order to stabilize the bipolaron, repulsion between the two like charges and the entropic term must

be compensated by the influence of nearby oppositely charged ions that donated the charges to the chain. The system is subjected to introduce two subgap

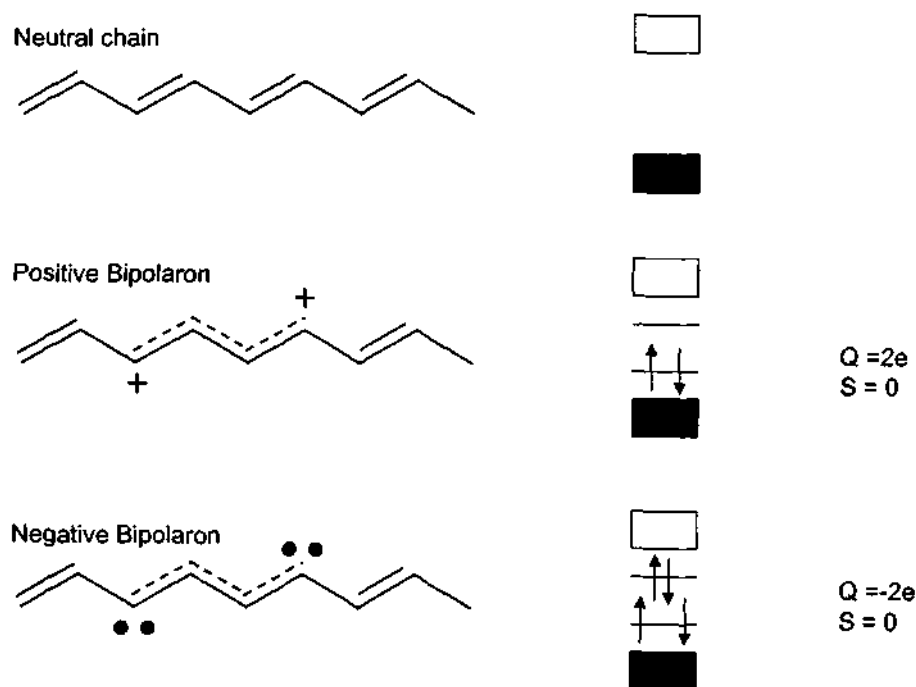


Fig. 1.8 Various types of *bipolarons* with their spin and charge state.

energy levels due to the formation of bipolarons (either positive or negative) (Fig. 1.8). The stability of a bipolaron is thus strongly influenced by the temperature and the concentration of charge carriers. Low charge concentration or higher temperature increases configurational entropy, promoting the dissociation of a bipolaron into two polarons. Photoinduced absorption, chemical doping, charge modulation spectroscopy etc. have been successfully adopted to detect the existence of bipolarons in several non-degenerated ground state polymers.

### 1.2.2 Doping in Conjugated Polymers

In order to increase the conductivity, the conjugated polymers can be doped to generate excess number of quasiparticles but in a totally different manner as compared to doping of the conventional semiconductors. In conjugated polymers, doping undergoes through a chemical redox reaction that involves

partial addition (reduction) or removal (oxidation) of electrons to/from the  $\pi$ -backbone. Typically there are existing three different processes to dope a polymer, namely (i) *chemical doping*, (ii) *photogeneration*, and (iii) *charge injection*. In chemical doping scheme, a double bond is broken, followed by charge transfer between the polymer chain and the dopant. This leads to an increase in conductivity. Photogeneration is another important process to increase the conductivity as far as application is concerned. It creates pairing of two opposite charge carriers and finally dissociation into isolated charge carriers to contribute in the transport process. This process will be discussed later. The charge injection is applied to a polymer semiconductor, sandwiched between two metal electrodes with appropriate work functions. The electrons are injected into the  $\pi^*$  band through one electrode, accompanied by the removal of electrons (i.e. injects holes) from the  $\pi$  band through the other electrode. This process is vastly used in organic light emitting device (OLED), leading to radiative recombination of the injected electrons and holes in the system.

### 1.2.3 Hopping Transport

Various approaches with certain approximations have been proposed to

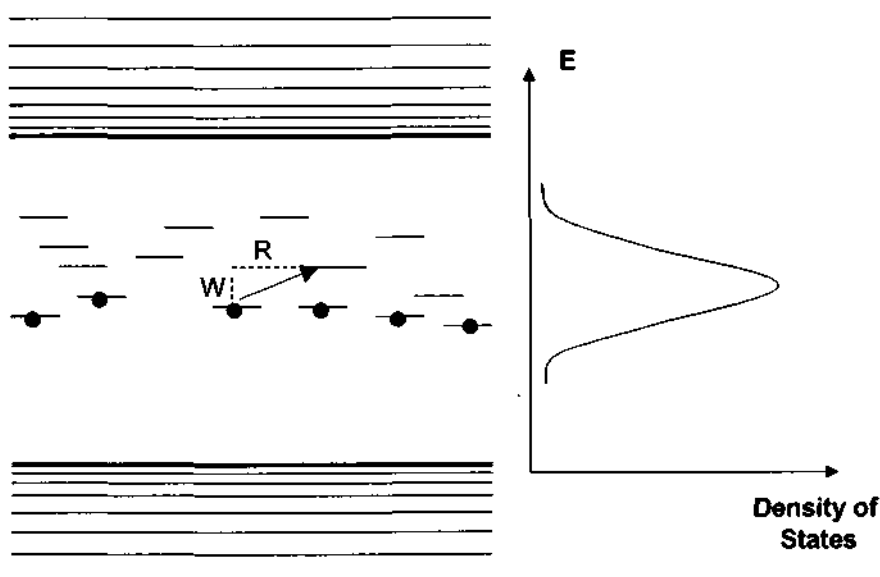


Fig. 1.9 Schematics for the hopping-model.

explain the conduction mechanism in conjugated polymer-based system. Several similarities between the conjugated polymers and the disordered or amorphous materials have been observed due to the commonality in aperiodic crystal structure. Unlike well-defined band structure of crystalline solid, localized energy states are likely to appear within the band gap of disordered system. As a consequence, the transport occurs via *phonon-assisted quantum mechanical tunneling*, also termed as *hopping* mechanism, between the energetically favorable states. Three different conduction channels are discussed in this section.

(i) **Extended state conduction:** Conduction process of this category involves the transport of thermally-excited electrons into the extended states that are beyond the mobility edges ( $E_c$ ). Considering a constant density of states (DOS) and constant mobility, the conductivity at any temperature can be expressed as

$$\sigma \propto \sigma_0 \exp[(E_c - E_f)/k_B T] \quad (1.1)$$

where  $E_f$ ,  $k_B$  and  $T$  are the Fermi energy level, Boltzmann constant and the temperature in absolute scale, respectively. This model can be applied to an isolated one-dimensional (1D) chain, where the conduction is thermally activated in nature.

(ii) **Conduction in band tails:** In a disordered system, the localized states exist between the mobility edges and  $E_f$ . Conduction within this region takes place by thermally activated hopping. Electrons are likely to hop from one localized state to the other by exchanging energy  $W(E)$  with a phonon. The mobility, in such circumstance, is expected to be thermally activated and can be written of the form

$$\mu_{\text{hop}} \propto \mu_0 \exp[-W(E)/k_B T] \quad (1.2)$$

and the conductivity

$$\sigma_{\text{hop}} \propto \sigma_0 T' \exp\left[-\frac{E_c - E_f + W}{k_B T}\right] \quad (1.3)$$



assuming a power dependence of DOS with respect to energy.

(iii) *Conduction in localized states at the Fermi energy:* For a disordered material, the subgap localized states are randomly distributed in space as well as in energy. The Fermi energy level  $E_f$  lies at the centre of the gap along with the localized occupied states below it and occupied states above, under no thermal agitation (Fig. 1.9). The charge carriers hop between the states either by absorbing or by emitting phonons, which dictate the upward or downward hopping in the energy landscape, respectively. A carrier may either hop a small distance with high activation energy or hop over a long distance with low activation energy. The temperature dependence of carrier transport strongly depends on the density of localized states. Most hopping models are based on the Miller-Abrahams [37] expression for the probability that one carrier jumps over a distance  $R$  from a starting state of  $E_s$  to the target state of energy  $E_t$

$$\Gamma(R, E_s, E_t) = \nu_{\text{ph}} \exp\left[-2\alpha R - \frac{\eta(E_t - E_s)}{k_B T}\right] \quad (1.4)$$

where the term inside the parenthesis is often termed as the hopping parameter,  $\nu_{\text{ph}}$  is the attempt-to-jump frequency ( $\sim 10^{12}$ - $10^{13}$  Hz),  $\alpha$  the inverse localization radius, and  $\eta$  the unity step function. The first term of the hopping parameter signifies the overlapping of the wavefunctions and the second term is related to the probability of finding a phonon of energy  $W = (E_t - E_s)$ . By further manipulation and representing DOS at  $E_f$  as  $N(E_f)$ , the conductivity takes the form

$$\sigma = (1/6)e^2 R^2 N(E_f) \nu_{\text{ph}} \exp(-2\alpha R - W/k_B T) \quad (1.5)$$

With lowering temperature, the phonon gets frozen, minimizing the probability of a carrier to hop to a higher energetic nearest neighbor. At this juncture, the carriers tend to hop to a larger distance rather than to the nearest neighbors for occupying an energetically more favorable state. This process is so-called *variable range hopping mechanism*. The spatial distance between the two states has to be optimized for conduction to take place. According to the Mott's

approach [38], the average energy spacing between states near Fermi energy level is given by

$$W = \frac{3}{4\pi R^3 N(E_f)} \quad (1.6)$$

The average hopping distance can be estimated by making  $d\Gamma/dR = 0$  and substituting Eq. 1.6, as

$$R_{avg} = \left[ \frac{9}{8\pi\alpha N(E_f)k_B T} \right]^{1/4} \quad (1.7)$$

Finally, the conductivity is found as

$$\sigma = \sigma_0(T) \exp\left[-(T_0/T)^{1/4}\right] \quad (1.8)$$

This is the famous Mott's " $(1/T)^{1/4}$  law" for 3D system. In general, for hopping with dimensionality  $d$  is of the form

$$\sigma = \sigma_0(T) \exp\left[-(T_0/T)^{1/(1+d)}\right] \quad (1.9)$$

This law holds good for amorphous semiconductor, moderately doped polyacetylene and several other polymers. In case of heavily doped system, the model is likely to be modified by considering the cluster of the localized states unlike their random distribution [39]. The temperature dependence of conductivity also changes accordingly with an additional parameter  $T_1$  as

$$\sigma = \sigma_0 \exp\left[-\frac{T_0}{T_1 + T}\right] \quad (1.10)$$

It leads to constant conductivity for  $T \ll T_1$  and to activated behavior for  $T \gg T_1$ , as observed in heavily doped polyacetylene [40].

It is to be noted that Mott's derivation of VRH model is based on several simplified assumptions like energy independence of DOS at  $E_f$ , neglect of

correlation effects in the tunneling process, neglect of electron-electron interactions etc. When the Coulomb interaction between the electrons is strong, a linear gap opens up in the DOS at  $E_f$ . Efros and Shklovskii [41] reported that in this regime conductivity can be expressed as

$$\sigma = \sigma_0 \exp\left[-(T_0/T)^{1/2}\right] \quad (1.11)$$

with the activation energy  $T_0 = (6.2 e^2/k_B \epsilon \xi)$  where  $\epsilon$  and  $\xi$  are the dielectric constant and the localization length respectively [42]. It has been reported that when VRH is assisted by electron-electron interaction, a universal  $\sigma_0 (\approx e^2/h)$ , being independent of temperature, may arise. This is completely different from the VRH, assisted by electron-phonon interaction.

Adequate efforts have been attempted to obtain the conductivity of the disordered materials by considering different DOS. While for amorphous semiconductors, one usually assumes an *exponential* DOS, for organic materials it is presumed that DOS is *Gaussian* distribution in nature with width  $\Sigma$  [43] and is given by

$$g(E) = \frac{N}{\Sigma\sqrt{2\pi}} \exp\left(-\frac{E^2}{2\Sigma^2}\right) \quad (1.12)$$

where  $N$  is the total density of localized states. The parameter  $\Sigma$  is a measure of energy disorder, which could be fluctuations in the polarization energy as well as dipolar interactions or impurity molecules. The model based on averaging carrier jump rates yields the mobility under low field [44] as

$$\mu = \mu_0 \varphi(N) \exp\left[-\left(\frac{C\Sigma}{k_B T}\right)^2\right] \quad (1.13)$$

and so the conductivity is  $\sigma \propto \exp[-(C\Sigma/k_B T)^2]$ . Here  $C$  and  $\varphi$  are two parameters depending on the density of localized states. The same relationship between temperature and conductivity can also be arrived using different

approaches like Monte Carlo simulations [43], analytical theories [45], and percolation theory considering nearest neighbor hopping [46].

#### 1.2.4 Trap Limited Transport

In the preceding section, the conduction was discussed on the basis of phonon-assisted hopping transport through the localized states. Due to the weak electronic coupling between organic molecules, disorder is of primary interest to understand the conductance in these materials. Disorder manifests itself in energetic variations of the electronic states of different molecules and in the structural variations of the solid state. However, in the case of disordered materials, one could expect the trap limited dispersive transport.

A defect state can act either as a trap or a recombination centre, depending on its location, capture probability and releasing probability of charge carriers. It is worth to mention that the traps lie close to the conduction band (LUMO levels) or valence band (HOMO) are shallow traps and the ionization energy

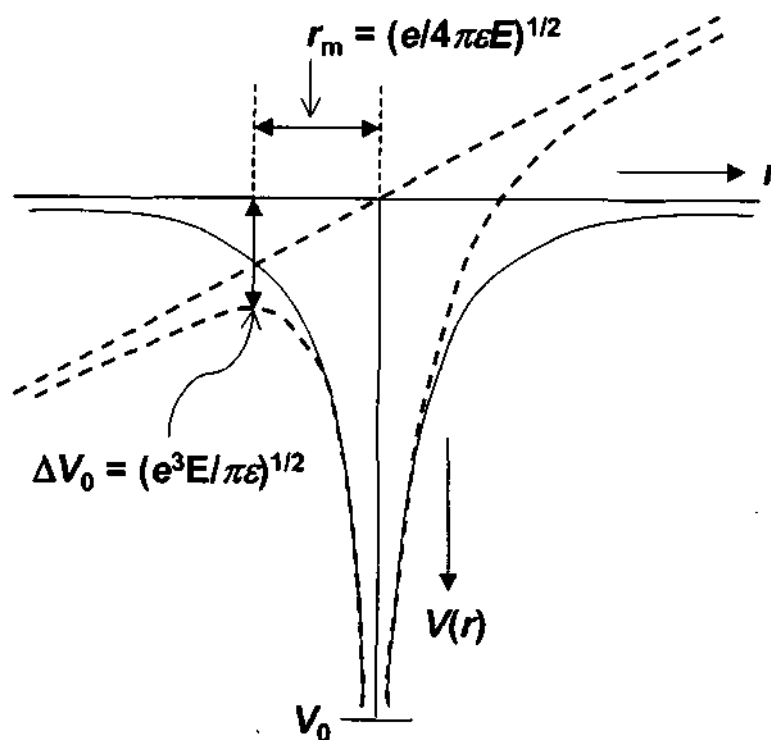


Fig. 1.10 Potential surface of 1D coulombic well with a superimposed external electric field.

can be closely compared to the thermal energy ( $\sim k_B T$ ). Similarly for the deeper trap levels, the traps lie relatively far away from their band edges and the ionization energy can be several orders higher than  $k_B T$ . Therefore the probability of a trapped charge to be re-emitted back to its respective band edges to contribute current must be very less. The trap distribution may be discrete, an exponential or Gaussian in nature.

(i) **Poole-Frenkel Effect:** If an electron trap is regarded as a positively charged centre at a fixed position in a solid, the potential energy of an electron is

$$V(r) = \frac{-e^2}{4\pi\epsilon r} - eEx \quad (1.14)$$

where the field  $E$  is applied in the  $x$ -direction,  $\epsilon$  the permittivity of the medium and other symbols have their usual meanings. It was first pointed out by Frenkel [47] and then modified further by Vermilyea [48]. In the absence of an externally applied field, the maximum value of  $V(r)$  is zero that occurs at infinite distance from the trap. Under the applied field,  $V(r)$  is reduced in one side of the trap by an amount of  $(e^3 E / \pi \epsilon)^{1/2}$  at a distance  $(e / 4 \pi \epsilon E)^{1/2}$  from the trap (Fig. 1.10). This results in increase of the ratio of free charge carrier density to trapped charge density and also increases the mobility.

(ii) **Space-charge-limited Current:** When the generation rate exceeds the collection rate or in other words, if trapping rate is larger than the de-trapping rate, charges are accumulated. Consequently the occupation of charge carriers modifies the applied electric field and influences the conduction process. This process is called the space-charge-limited current, which is non-ohmic in nature. The current-voltage relationship can be derived using Poisson's equation for the plane parallel electrode configuration. Considering trapped charges are comparable to the conducting charges, one can introduce a parameter  $\theta$  as

$$\frac{\rho_{\text{free}}}{\rho_{\text{free}} + \rho_{\text{trap}}} = \theta = \frac{N_c}{N_{\text{trap}}} \exp\left(-\frac{E_c - E_{\text{trap}}}{k_B T}\right) \quad (1.15)$$

where  $\rho_{\text{free}}$ ,  $\rho_{\text{trap}}$  are the free and trapped charge densities, respectively,  $N_c$  is the effective density of states (DOS) available in the conduction band with lowest energy  $E_c$  and  $N_{\text{trap}}$  is the density of trap at energy state  $E_{\text{trap}}$ . Using Poisson's equation of the form  $dE/dx = [(\rho_{\text{free}} + \rho_{\text{trap}})/\epsilon]$  and neglecting the diffusion term, current density can be written as

$$J = \mu\theta\epsilon E \frac{dE}{dx} \quad (1.16)$$

where  $\mu$  and  $\epsilon$  are the mobility and permittivity respectively. On integration and applying the boundary condition that  $E = 0$  at  $x = 0$  (position of the electrode), current-voltage equation is arrived as

$$J = \frac{9}{8} \mu\epsilon\theta \frac{V^2}{L^3} \quad (1.17)$$

This is the famous Mott-Gurney law showing non-linear current-voltage relation, where  $V$  is the applied voltage and  $L$  the distance between the two electrodes [49]. Considering the Poole-Frenkel effect along with further modification, the relation turns into

$$J = \frac{9}{8} \mu\epsilon\theta \frac{V^2}{L^3} \exp\left[\frac{0.891}{k_B T} \left(\frac{e^3 V}{\pi\epsilon L}\right)^{1/2}\right] \quad (1.18)$$

It is to be noted that Poole-Frenkel eventually modifies Eq. 1.17 increasing  $\theta$ .

(iii) **Continuous-time random walk:** The first theoretical and discrete model to describe the dispersive kind of transport phenomenon is known as continuous-time random walk (CTRW). The model is based on the assumptions that any material can be sub-divided into several cells, each of which contains a large number of microscopic hopping sites for electron or holes. The time spent by a charge in a particular cell prior in moving to the next cell is assumed to be described by a statistical distribution function  $\psi(t)$ <sup>2</sup>. The transfer rate of charge from one cell to the next is determined by the following equation

$$\frac{dP(l,t)}{dt} = \int_0^t \Phi(t-t') \sum_{l'} [\nu(l-l')P(l',t') - \nu(l'-l)P(l,t')] dt' \quad (1.19)$$

where  $P(i, t)$  is the probability that  $i$ -th cell is occupied at time  $t$ ,  $\Phi(t)$  is the relaxation function related to  $\psi(t)^2$ ,  $v(l-l')$  is the transition probability.

(iv) **Multiple-Trapping Model:** The multiple-trapping (MT) model (also called multiple-trapping and release model) is a continuum limit of the CTRW. In this model, the coexistence of the continuous electron and hole transport states associated with high concentration of traps for electrons and holes is assumed. While moving through transport states, a charge carrier encounters trap, which then captures with a capture rate  $\omega_i$  and subsequently releases with a rate  $r_i$ . The instantaneous charge density  $n(x, t)$  at a position  $x$  is then sum of the charge density in transport states  $p(x, t)$  and the charge density in traps  $p_i(x, t)$  i.e.

$$n(x, t) = p(x, t) + \sum_i p_i(x, t) \quad (1.20)$$

with the continuity equation and rate equation

$$\frac{\partial n}{\partial t} = -\mu_0 E \frac{\partial p}{\partial x} \quad \text{and} \quad \frac{\partial p_i}{\partial t} = p \omega_i - p_i r_i \quad (1.21)$$

On further modification, the transport equation becomes

$$\frac{\partial n}{\partial t} = -\mu_0 E \int_0^t Q(t-t') \frac{\partial n(x, t')}{\partial x} dt' \quad (1.22)$$

where  $Q(t-t')$  is a relaxation function related to the amount of time spent by the charge carriers. This equation is a continuum limit of CTRW equation. However, MT model is much more appealing than CTRW, because the former deals with the charge capture and release and does not use the artificial division of the materials into cells.

### 1.3 PHOTOCONDUCTION IN CONJUGATED POLYMERS

The bandgap energy of conjugated polymers usually lie in the range between 1 eV and 3 eV. The photogeneration process takes place primarily via an intermediate state, called the *exciton*, which is a quasiparticle consisting of

electron-hole pair with a finite binding energy. There is a big controversy over the binding energy of exciton. In some publications, it has been argued that the binding energy of exciton is much less than thermal excitation at room temperature so that the photoexcitation directly creates free carriers analogous to the conventional semiconductors [50,51]. But the most acceptable explanation of photogeneration is through the formation of exciton with binding energy  $\sim 0.4$  eV [52]. Photoinduced charge transport in solid organic polymers is likely to follow the route through: (i) exciton formation, (ii) exciton diffusion to a dissociation site, (iii) exciton dissociation into positive and negative charge carriers and finally (iv) charge (majority) transport under the influence of applied field.

### 1.3.1 Excitation Formation

Upon photoexcitation to the organic/polymeric semiconductor, two oppositely charge carriers bind each other by electrostatic interaction and thus

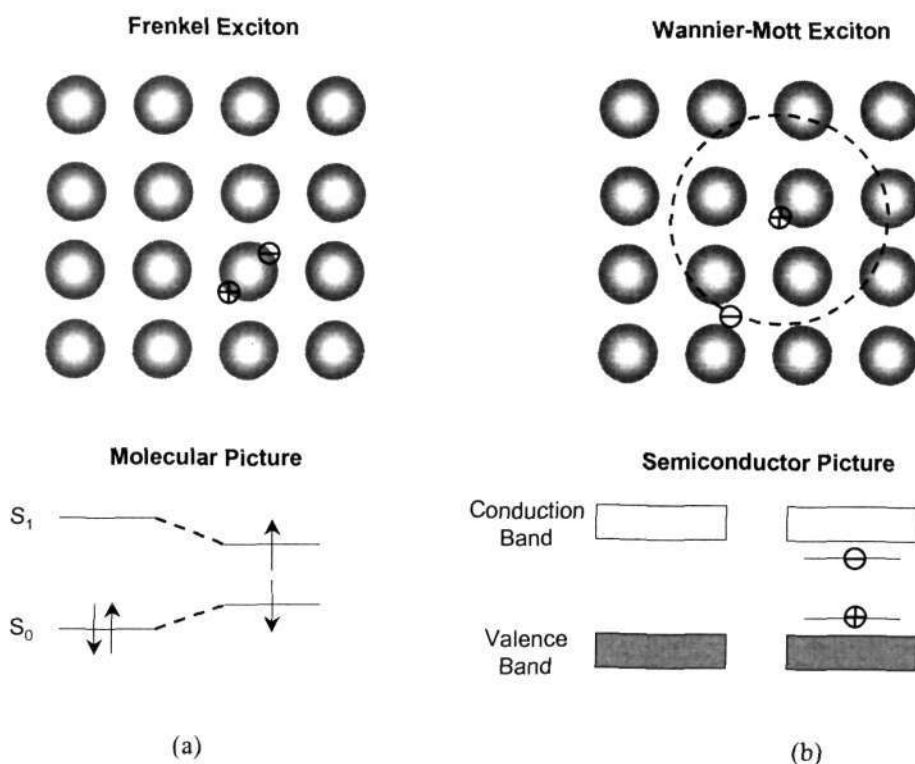


**Fig. 1.11** Schematic of (a) Frenkel exciton showing the energy level diagram of discrete molecular states and (b) Wannier-Mott exciton with the corresponding semiconductor band diagram.



forming a mobile molecular excited state, which is usually referred to as *exciton*. Typically excitons are singlets (though triplet excitons were also observed in polymers) due to the opposite spin of electron and hole. An exciton, being electrically neutral, does not contribute to the charge transport but it transports the energy from one site to the other depending on the diffusion length (~ several nm). The extent of delocalization of excitons strongly depends on the interplay between intermolecular interactions and the Coulomb interactions. Depending on the degree of delocalization and the binding energy, the excitons are classified as Frenkel, Wannier-Mott or charge-transfer.

*Frenkel excitons* are created due to strongly correlated electron-hole pair localized on a single molecule. The radius of this kind of excitons is quite comparable to the size of the molecule or sometimes smaller than that of intermolecular distance ( $< 5 \text{ \AA}$ ) (Fig. 1.11a). It is considered that these excitons are neutral particles that can diffuse site to site. The local electric field of the exciton polarizes the surrounding lattice, eventually generating polaron-type of quasiparticles. The translational states of Frenkel excitons have the form of propagating waves that can be described in terms of Hamiltonian. Frenkel excitons are rarely identified in inorganic semiconductors due to having strong overlap between neighboring lattice atoms to nullify the localization effects.

*Wannier-Mott (WM) excitons* are generated in uncorrelated crystalline materials in which overlap between neighboring lattice atoms reduces the Coulombic interaction between the electron and the hole involved. Consequently, this results in large exciton radius (~ 40-100  $\text{\AA}$ ) with relatively weak binding energy (Fig. 1.11b). The binding energy of WM exciton of  $n$ -th order excited state is given by

$$E_n = -\frac{m^* e^4}{2\hbar^2 \epsilon^2 n^2} \quad (1.23)$$

where  $\epsilon$  is the dielectric constant,  $\hbar = h/2\pi$  ( $h$  being the Planck's constant) and  $m^*$  is the effective mass of WM exciton. The energy levels are discrete and can be identified spectroscopically for optically active semiconductors. This type of excitons is most common species in traditional inorganic semiconductors with

binding energy ranging from several meV to 60 meV for different materials. At ambient temperature, the WM excitons in most of the inorganic semiconductors are dissociated and the associated energy levels are broadened too strongly to suppress the signature as compared to the regular optical absorption.

The *charge-transfer (CT) exciton* belongs to an intermediate between a Frenkel and a WM state, being neither extended nor tightly bound to a single molecular site. Theoretical description of such exciton is difficult to express. There are several approaches to understand the nature of CT exciton. Sometimes it is considered that the CT excitons are composed of an unrelaxed polaron pair with the positive and negative polarons located on discrete, identifiable and adjacent molecules [53]. A model, based on the self-consistent field approximation, has been proposed to express the delocalized CT exciton recently. One-electron Hamiltonian for a system with low exciton density consists of kinetic energy term, electron-hole interaction term and a periodic pseudopotential term. This model holds satisfactory in ionic or covalently bonded semiconductor, where pseudopotential is negligible compared to the electron-hole interaction. But it is no longer reasonable in a weakly bonded molecular crystal, where CT exciton gets localized.

In particular, one could expect that the binding energy of excitons is higher in conjugated polymers than that in conventional inorganic semiconductors. First of all, the dielectric constant of conjugated polymers is smaller than that of inorganic semiconductors, increasing the binding energy. Secondly, the weak intermolecular interactions promote to generate Frenkel type of exciton in some materials. However, it is to be mentioned that excitons in many polymeric semiconductors have not been directly observed. This is mainly due to the superposition of inhomogeneous absorption edge broadening and excitonic features, which obscures the signature of exciton from the normal absorption spectra. Due to specific geometry of polymeric strand, it is more reasonable to divide excitons into two different groups; namely (i) *Intrachain excitons* and (ii) *Interchain/Charge-transfer excitons*. *Intrachain excitons* are composed of electron-hole pair in a single chain within the same conjugation

element and predominantly appeared in polymer system. *Interchain/Charge-transfer excitons* are the species in which electron and hole belong to two different molecules or two different polymeric chains with different bandgap energies.

### **1.3.2 Excitation Transport**

Although excitons are initially localized on a single molecule and electrically neutral, these quanta of energy can travel through the solid even up to several hundreds of molecules away from the source of creation. These quasiparticles normally transport the energy without the migration of net electric charge. The transport may be either *radiative* in which an exciton emits a photon that is absorbed by another part of the solid to create a second exciton, or *non-radiative* like electromagnetic wave packet transport, hopping transport, and long-range resonant transfer through the distribution of exciton. The models can be well described by diffusion equation irrespective of the transport processes in nature. Electromagnetic wave packet transport occurs when the exciton binding energy is relatively large compared to intermolecular hopping potential energy. This transport is a coherent process due to the fact that the incident wavelength ( $\lambda \sim 500$  nm) is much larger than the lattice spacing ( $\sim 10$  nm) or inverse absorption length ( $\alpha^{-1} \sim 50$  nm). This generates excitons to have well-defined phase relationship. The time required to transfer the exciton from one molecule to the other is much faster than that it takes for the atomic nuclei to rearrange. Thus it is not a phonon-assisted process, as result of which it can travel a long distances until gets scattered. The time period of excitonic motion, before being scattered, is termed as coherence time ( $\tau_c$ ). For molecular organic materials  $\tau_c$  is typically  $< 10^{-13}$  sec. At times greater than  $\tau_c$ , exciton encounters scattering due to strong electron-phonon interactions, which break the coherence and the transport process is turned into hopping mechanism. Another important transport process is long-range ( $\sim 10$  nm) resonance transfer, which involves Förster dipole-dipole interaction to cascade the energy. The main criterion for the process to take place is overlapping between the donor

luminescence and the acceptor absorption, rather than the periodic order in the solid.

### 1.3.3 Excitation Dissociation

The created exciton has two fates during its temporal evolution. One is that exciton eventually separates and escapes from recombination. This contributes to the photocurrent. The probability is termed as *quantum yield* or sometimes *quantum efficiency* ( $\eta$ ), and by definition the amount of free charges collected per absorption of a single photon. The other possibility is that exciton may recombine, which results in fluorescence (radiative recombination) or an

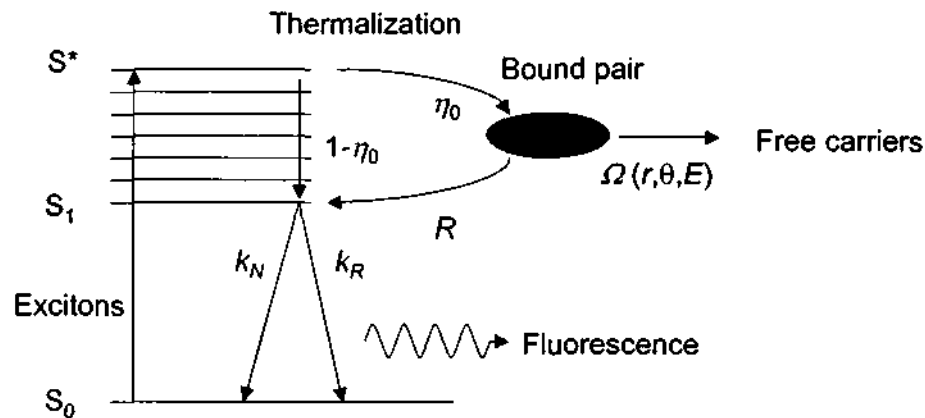


Fig. 1.12 Schematic representation of carrier photogeneration process as described by Onsager model.

increase in thermal energy of the medium (non-radiative recombination). Excitons can be dissociated by either thermal energy or electric field or both. In conjugated polymers, the value of typical exciton binding energy lies in the range of  $E_{exc} \sim 0.4 - 1$  eV. To compensate the binding energy, one may need several thousand degrees of Kelvin, which is not a reasonable option. Another way to dissociate exciton is to apply external electric field  $E_{ext} > (E_{exc} / e r_{exc})$ . For a conjugated polymer, the exciton radius  $r_{exc}$  is on the order of 1 nm, yielding minimum field required  $\sim 10^6$  V/cm.

(i) **Onsager Theory:** A large number of studies have been done to understand the interplay between the exciton dissociation into charge carriers

**24 / Introduction**

and recombination process in disordered system. The oldest theory in this field was proposed by Onsager in 1930s, which is known as Onsager's theory [54,55]. In this scheme, the electrons that are excited from neutral  $S_0$  state to a highly excited state  $S^*$ , thermalize at a distance  $r_0$  (thermalization length) to form the exciton. The fraction is called the primary quantum efficiency  $\eta_0$ . The ultimate probability for dissociation into free carriers is  $\Omega(r, \theta, E)$ , where  $\theta$  is the angle between the vector of the bound pair  $r$  and the applied electric field  $E$ . The recombination rate is determined by  $R = 1 - \Omega(r, \theta, E)$ . Some of the states  $S^*$  may relax to the first excited singlet state  $S_1$  with probability of  $1 - \eta_0$  and then decay to ground state  $S$  via radiative or non-radiative route with rate constant of  $k_R$  or  $k_N$  respectively. The overall quantum efficiency is given by

$$\eta = \eta_0 \int \Omega(r, \theta, E) g(r, \theta) d\tau \quad (1.24)$$

where  $g(r, \theta)$  is the initial spatial distribution of thermalization length. The main outcomes of this model are: (i) a strong dependence on the electric field in the middle regime, nonzero values at low field and saturation at high field, (ii) a weak increase with temperature, (iii) a strong dependence on the incident

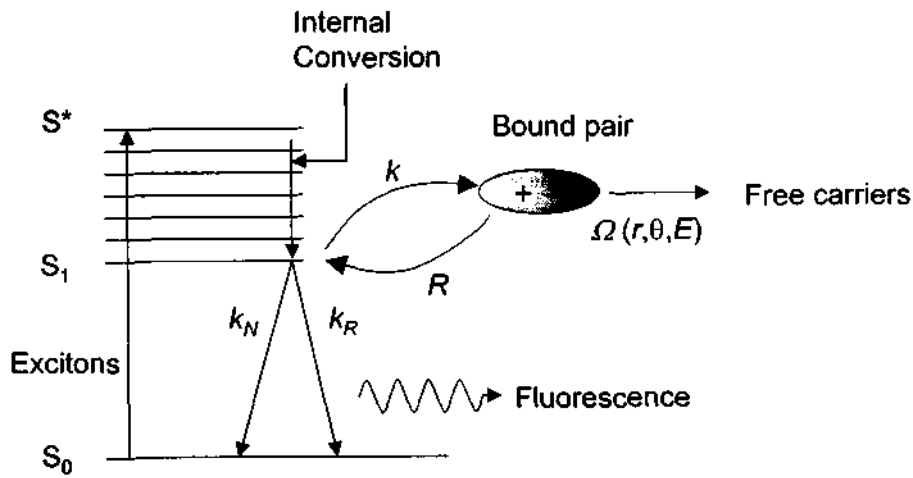


**Fig. 1.13** Schematic representation of the charge carrier photogeneration in the case of complete internal conversion in organic materials.

photon, (iv) a large thermalization length of about few nanometers. However,

the drawbacks of this model are the strong influence of incident energy on photogeneration and the large thermalization length, which are inconsistent with experimental results. The entire process is displayed in Fig. 1.12.

(ii) **Noolandi and Hong Theory:** The violation of Onsager theory was observed in electric field-induced fluorescence quenching measurement on x-phthalocyanine in which the photogeneration efficiency was insensitive to the excitation wavelength [56]. To avoid such shortcoming of the model, Noolandi and Hong proposed more reasonable explanation [57]. According to this model, the highly excited state  $S^*$  may lose the total excess energy fully or partially via *internal conversion*, as shown in Fig. 1.13. This leads to a quantum yield, which is fully or partially insensitive to excitation energy.

(iii) **Braun Theory:** Another shortcoming of Onsager theory, as mentioned earlier, is large thermalization length ( $\sim 20$  to  $30 \text{ \AA}$ ) in case of polymers or doped polymers. But from spectroscopic evidence, a charge transfer exciton

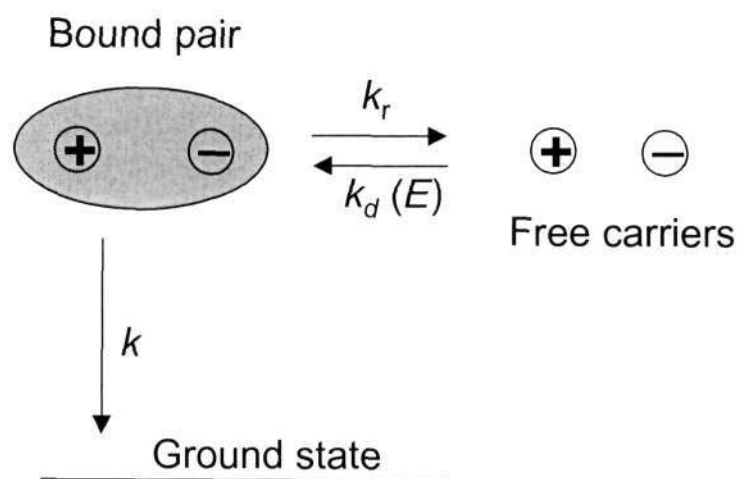


**Fig. 1.14** The kinetics of the bound pair dissociation.

involves mainly nearest neighbor ( $5 \text{ \AA}$ ) electron transfer [58,59]. The puzzling question is that how a charge pair could evolve from an initial nearest neighbor to the much larger thermalization length. The discrepancy was removed in the context of Braun theory. According to this theory, the bound pair could be the

lowest lying singlet, or triplet charge transfer state that can be created either by direct optical excitation or when an excited neutral donor (or acceptor) encounters an acceptor (or donor). The bound pair dissociates into free carriers with an electric-field dependent rate constant  $K_d(E)$  or decays to the ground state either radiatively or non-radiatively with a rate constant  $k$  (Fig. 1.14). The photogeneration efficiency in this model is given by,

$$\eta(r, T, E) = \frac{K_d(E)}{K_d(E) + k} \quad (1.25)$$

When a distribution of charge separation distances exists, the efficiency can be expressed as

$$\eta(T, E) = N_f \int \eta(r, T, E) g(r, \theta) dr \quad (1.26)$$

where  $g(r, \theta)$  is the distribution function of intrapair separation, and  $N_f$  is a normalization factor for the function  $g(r, \theta)$ . The integration should be taken over a distribution of intrapair distances. The Braun theory provides similar result to the theory described by Onsager, but with considerable small intrapair radius.

(iv) **Effect of Spatial Distribution on Photogeneration:** In both Onsager theory and Braun theory, the spatial distribution of initial thermalization length of the form of isotropic delta function has been taken into consideration. In highly disordered system, the individual excited state experiences different physical and chemical environments. This may result in spatial distribution of initial intrapair distances. It is statistically reasonable to assume isotropic distribution, so that the overall quantum efficiency takes the form

$$\eta(T, E) = N_f \eta_0 \int \eta(r, T, E) g(r) dr \quad (1.27)$$

where  $N_f$  is a normalization factor for the function  $g(r)$ .

(v) **Surface Enhanced Photogeneration:** The long-living excitons, which are widely observed in the bulk of the polymer semiconductor, diffuse to the

$$\frac{dn(x)}{dt} = \alpha I_0 \eta \exp(-\alpha x) - D \frac{d^2 n(x)}{dx^2} - \frac{n(x)}{\tau} - \gamma n^2(x) \quad (1.28)$$

surface and dissociate into free charge carriers. The process can be expressed mathematically by the following conservation equation

where  $\alpha$  is the linear absorption coefficient,  $\eta$  the average quantum efficiency,  $I_0$  the intensity of the incident light,  $D$  the diffusion coefficient,  $\tau$  the average lifetime of the exciton and  $\gamma$  the rate constant of bimolecular recombination. The steady state solution of the above equation incorporating appropriate boundary condition gives the number of charge carriers that are created. The surface-enhanced dissociation has been extensively adopted to explain the photogeneration in organic materials, particularly when the efficiency depends on the ambient condition. This approach is flexible for both the excitons as well as free charge carriers, but it fails to establish a valid relationship between the efficiency and temperature.

#### **1.4 OPTOELECTRONIC DEVICE PERSPECTIVES**

Apart from being a model system for understanding the photophysics of disordered materials, conjugated polymers provide a broad spectrum of contemporary interest in technological implication. Despite several limitations, polymer based electronic devices have shown tremendous potential in variety of applications due to tractable physical and chemical properties. The photoresponsive property, luminescence property and self-assembling property of conjugated polymers have been extensively exploited in photodiodes, photovoltaics, solar cells, organic light emitting diodes (OLEDs), organic field effect transistors (OFETs) etc. This section focuses a brief overview of all the devices.

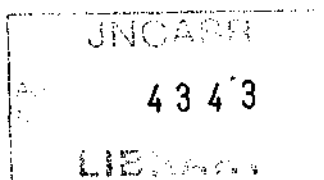
##### **1.4.1 Photodetectors, Photovoltaics, Solar Cells**

Significant photoresponse of semiconducting polymers offers considerable progress in fabricating high-sensitive photodetectors and high-efficiency solar cells. An efficient polymer based photoresponsive device encompasses the following processes: (i) absorption of light, (ii) exciton generation, (iii) exciton diffusion, (iv) exciton dissociation into free charge carriers, (v) transport into



the medium and finally (vi) collection of free charge carriers by the electrodes. Typical device architecture of photodiode (or photodetector) consists of a sandwich configuration between two asymmetrical metal-electrodes with different workfunctions, which enables to dissociate the created excitons [17]. But in most of the cases workfunction difference is not sufficient for charge generation. The device performance was, to some extent, improved by introducing a Schottky-type junction between the conjugated polymer and one of the metal electrodes [60]. However, this approach was also not enough for effective charge generation. An alternative approach to overcome the limitation has been adopted successfully by fabricating heterojunction device either in bilayer or in bulk-heterojunction configuration. The bulk-heterojunction configuration preferably offers enhanced photoresponse since the effective photogeneration area covers the whole layer of the composite, compared to the narrow geometrical interface zone in bilayer device. Fullerene C<sub>60</sub> is commonly used as electron acceptor in bulk-heterojunction device together with conjugated polymers as hole acceptor. Using this technique, charge generation efficiency rises to ~ 100% due to fast charge transfer in sub-picosecond time scale [61,62]. A substantial improvement in the field of photodiodes and digital image sensors has been reported elsewhere [17–19].

The discovery of ultra-fast charge transfer in conjugated polymer/fullerene composite has provided the opportunity to develop photovoltaics and solar cells [63]. The basic differences between photodetectors and photovoltaics are: (i) in the case of former, charge generation takes place under reverse bias condition, whereas in the case of latter photoinduced voltage is developed under open-circuit conditions (under no external bias); (ii) in current (amplitude)-voltage (I-V) characteristic, photodetectors shows a minimum at null voltage under photoexcitation, whereas in photovoltaics the minimum of I-V gets shifted from zero voltage depending on the photovoltage developed. However, the recent reports with different strategies such as tandem cell configuration, addition of electron blocking layer, annealing, etc. have implemented to increase the conversion efficiency up to ~ 5% [61,64,65,66]. Several bottleneck problems



associated with complexities like weak red absorption, less stability, poor transport etc. are yet to be overcome to obtain highly efficient solar cells.

#### 1.4.2 Organic Light Emitting Devices (OLEDs)

A notable key difference between the organic and inorganic LEDs, lies on the fact that in the former device, carriers are directly injected unlike the latter in which charge carriers emanate from the dopants. An organic/polymeric LED consists of a thin uniform layer of organic or polymer semiconductors ( $\leq 100$  nm thick) which is sandwiched between a semitransparent anode, Indium tin oxide (ITO) and a reflective cathode (Ca, Mg, Ag, Al). When an electrical potential difference is applied between the high work function anode (usually indium tin oxide, ITO) and the low work function cathodes (Ca, Al, Mg or In), the following steps are likely to take place; (a) injection of holes from the anode and electrons from the cathode, (b) the transport of carriers throughout the bulk medium, (c) recombination of electrons and holes (excited singlet and triplet states, so-called excitons), (d) finally emission takes place from the recombination zone. Since most of the organic/polymeric semiconducting materials are intrinsically known to be *p*-type and therefore they are better suited to transport positive charges, the recombination of electrons and holes usually takes place in the vicinity of the cathode. As a consequence, the lifetimes and efficiencies of a single layered OLED are always limited [67]

A couple of decades ago, Tang and his coworkers revived the research on Electro Luminescence of organic compounds, developing a new generation of LEDs with organic fluorescent dyes [67]. In his discovery, he used Alq<sub>3</sub> and diamine as the electron transport and hole transport materials to fabricate the bilayer organic LED. In his work, he utilized fluorescent based dye doped systems to achieve high efficiency relatively higher than that of single-layered devices. The lifetimes and efficiencies were greatly enhanced by confining the charges to promote recombination in the interfacial layer by shifting the zone considerably [68].

621.381528  
12664

The first high efficiency polymer OLED, also called PLED, was fabricated using solution-processable precursor of poly(p-phenylene vinylene) (PPV), sandwiched between hole-injecting indium titanium oxide (ITO) and electron-injecting low workfunction metal [8]. Since their discovery in 1990 polymer light-emitting diodes (PLEDs) have been considered as promising candidates for large-area applications as a result of easy processing and mechanical flexibility. Additional attractive features of PLEDs as compared to other at display systems are high contrast and resolution, the absence of viewing-angle dependence, low power consumption, low voltage operation, fast response times, and the wide range of available colors. Most attention has been focused on PLEDs that contain the conjugated polymer poly (-p-phenylene vinylene) (PPV) or its derivatives, because of the high external conversion efficiency. Later with similar approach poly(cyanoterephthalylidene) has been used as active materials for OLED with 4% internal efficiency [69].

Though theoretical expectation of efficiency should reach up to 25% using singlet-triplet calculation, recent advancement of platinum containing polymer provided 63% luminescence efficiency [70]. Asymmetrical charge transport in conjugated polymer leads to exciton formation nearer to one of the two electrodes. Based on the fact, the efficiency is quite low due to the enhancement of non-radiative recombination near to the electrode/organic interface. In addition, highly mobile charge carriers can pass through the organic layer(s) and reach the electrode without forming exciton, eventually lead to further reduction in device efficiency. Significant improvement in OLED and PLED has been carried out implementing several strategies like heterojunction LED with both electron- and hole- transporting layers, doping the active organic layer with high photoluminescent dye etc. [71,72]. Since then, there has been tremendous attention paid to the further development of OLEDs to equalize the race against conventional LED based on inorganic materials [68,73,74].

#### **1.4.3 Organic Field-Effect Transistors (OFETs)**

The principle of the field-effect transistor (FET) was first proposed by Lilienfeld in 1930 [75]. Basically, a FET operates as a capacitor where one plate

is a conducting channel between two ohmic contacts, the source and the drain electrodes [76]. The density of charge carriers is modulated by the voltage applied to the second plate of the capacitor, the gate electrode. At low source-drain bias, the carrier density in the conducting channel may be varied independently using the gate voltage. The architecture of organic FETs is usually that of the thin-film transistor (TFT) first introduced by Weimer in 1962 [77] and currently used in most amorphous silicon transistors [78].

OFET differs from the conventional inorganic metal-insulator-semiconductor FET (MISFET) mainly by two important reasons: (i) OFET is operated in accumulation mode due to absence of inversion layer, (ii) OFETs can be ambipolar unlike unipolar inorganic FET. The combination of several efficient strategies and novel synthesis of organic materials have been implemented to achieve high mobility of the order of  $\sim 1 \text{ cm}^2 \text{ V}^{-1} \text{ s}^{-1}$  and even more. Their values are 3 orders in magnitude less than that of conventional FETs. It is to be noted that despite having mobility less than that of inorganic counterpart, tremendous efforts have been attempted in developing the former due to its several other prospective features like low-cost processing, tractability, flexibility in polymer materials. Parallel achievements on memory devices [27], light emitting FETs [26], ambipolar FETs [79,80], integrating OFETs into a single chip [23] etc. have provided an extra pace in the frontier research. There are several issues in terms of speed, mobility, stability and packaging, which are yet to be overcome efficiently. A comprehensive review on theoretical aspects, device configurations and the recent issues related to OFET are discussed in chapter 2.

### 1.5 MOTIVATION

OFETs/PFETs have undergone tremendous improvements in the last 5 years. The possibility of realizing FETs with measurable, demonstrable properties with relatively less efforts (in terms of processing and infrastructural requirements) provides a good platform to address several fundamental issues related to primary charge excitations and electrical transport in these issues. The

added novelty in the present case was the invention of the polymer FET at JNCASR in 2001 [81], which could be optically controlled. The asymmetrical charge transport in this device geometry along with highly responsive photodetection due to an internal amplification process was observed. The combination of device physics and photophysics provides unique opportunity to highlight and address the challenging aspects related to fundamental photoinduced processes and their applications. The detailed studies of the optical induced response of the FET were the need of the hour and form the backbone of the thesis.

The structure of this report is as follows: The relevant aspects of PFET, which form the base of this thesis is explored in chapter 2. The materials properties, device fabrication and the experimental techniques are described in chapter 3. The modification of the electrical charge transport process and the control of gate voltage over this modification are the major objectives of this thesis work. The dynamical aspects related to charge generation and their distribution in determining the relaxation process are demonstrated with various possible models in chapter 4. The novel memory features by exploiting the inherent slow decay process along with the gate voltage control are presented in chapter 5. Finally, the spatial information of charge generation and their distributions are discussed in chapter 6. Apart from the quantitative and qualitative studies, the possible applications of the device are also discussed in all the above-mentioned chapters.

## **Chapter 2**

### **Organic/Polymer Field-Effect Transistors**

#### **2.1 INTRODUCTION**

The invention of organic field-effect transistors (OFETs) is considered to be a landmark in the field of modern electronics enabling inexpensive processing technique. The first approach to fabricate FET using organic semiconductors was reported by Barbe and Westgate in 1970 [82] though the performance of the device was not so promising. The discovery of conducting polymers has turned around the future of electronics in a very fascinating direction due to the tractable mechanical and semiconducting properties of the materials, low-cost processing, possibility of large area electronics etc. The polymer FET (PFET) based on polyacetylene was first reported in 1983 [9] and there were marginal, incremental improvements in the performance. Remarkable improvements were demonstrated after a period of four years for polythiophene-based FET device structures [83,84]. Later on, organic small molecules [85] and conjugated oligomers [86] have attracted a considerable interest towards this field of transistors. For the past decades, significant number of researchers have shown interest in the subject areas of modification in synthesis, purification procedures, device fabrication methods, and engineering the metal/organic interfaces in order to improve the overall device performance. Issues related to stability and durability apart from device performance of PFETs and OFETs also needs to be addressed for these systems to be an alternative to amorphous Si-based TFTs.

#### **2.2 DEVICE OPERATION AND ELECTRICAL CHARACTERIZATION**

The simple and most prototypical device structure of OFET/ PFET device typically comprises of three electrodes, namely, source, drain and gate along with organic (polymer) layers. In principle, the operation of metal-insulator-semiconductor FET structure (OFET/PFET) is based on the control of charge

density within the semiconductor through the external gate voltage. The purpose of source and drain is to serve barrier-free charge-injection to the semiconductor upon application of certain external voltage; the gate electrode is isolated from the active semiconductor by a thin dielectric layer, describing the field-induced charge distribution near the semiconductor/insulator interface. High electric field at a trap-free interface between the semiconductor and the insulator

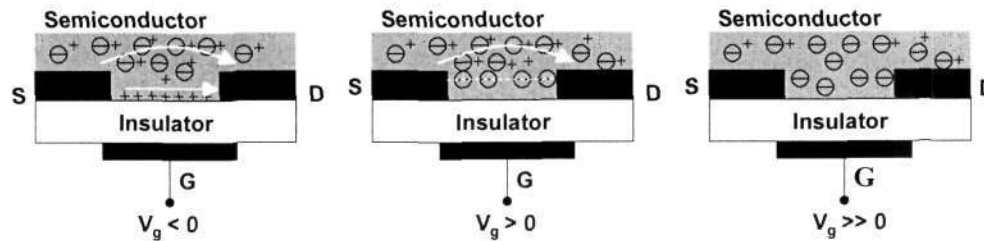


**Fig. 2.1** Schematic representation of charge distribution in PFET for accumulation ( $V_g < 0$ ), depletion ( $V_g > 0$ ) and highly depletion ( $V_g \gg 0$ ) modes.

renders bending of the energy band towards or away from the Fermi level depending on the polarity of the applied gate voltage. For example, in case of  $p$ -type semiconductor, the energy bands bend towards upward direction when the gate is subjected to a negative voltage. This results in accumulation of positive charges at the interface that provides a highly conducting (on) state, called the *accumulation* or *enhancement* mode. On the other hand, upon applying positive gate bias, the positive charges are pushed away from the interface due to opposite band bending, which leads to depletion of mobile charges. The positive charges within the depletion zone flow out from the device via the ohmic drain-source contacts. This mode of operation is called *depletion* mode, which possesses low conducting (off) state of the device (Fig. 2.1). The electrical performance of the FET is characterized mainly in terms of two parameters *field-effect mobility*, representing the speed, and *on/off current ratio*, describing the switching performance of the device.

### 2.2.1 Basic Requirements for OFET

There are stringent conditions that must be encountered to obtain a good quality OFET/PFET device. Initially, the semiconducting layer must be free

from defects which correspond to the absence of subgap energy levels. In reality, organics/polymers are disordered and it is expected that the degree of conjugation at the bend or twist will be lowered and the associated  $\pi$  and  $\pi^*$  states will move deep into the bands.

Secondly, the interface between the semiconductor and the insulator must be clean and free from surface states that may also act as traps for mobile charge carriers. For a definite insulator with permittivity  $\epsilon$ , the maximum surface charge density under accumulation mode can be estimated using the relation  $n_{\max} = \epsilon E_b / e$ , where  $E_b$  is the dielectric strength. This is of the order of  $10^{13}$  charge/cm<sup>2</sup> for silicon dioxide (SiO<sub>2</sub>) as a typical insulator used for fabricating FET devices. However, this value is low compared to the number of carbon atoms/cm<sup>2</sup>, typically  $10^{15}$  for polyacetylene. Since the polymers generally do not possess any dangling bond, as the bonding takes place only along the chain, one can expect the cleaner interface by avoiding any contamination during the exposure to oxygen and/or moisture during the fabrication process. Furthermore, there is an essential approach to improve the interface by depositing the semiconductor film with regular crystallinity.

Thirdly, fabrication of the semiconductor devices requires control of the concentration of the extrinsic charge carriers (typically  $\sim 10^{15}$ - $10^{18}$  charges/cm<sup>2</sup>) in order that the widths of depletion regimes are of the order of few hundreds of nanometer. In addition, the dopant species are required to be rather immobile at the operating temperature. This poses a critical challenge to use the conjugated polymers in this field. It has been found, in practice, the dopant ( $\sim 10^{16}$ - $10^{17}$  cm<sup>-3</sup>) concentrations that are utilized in poly (3-alkylthiophenes) (P3ATs) based FET structures during the preparation processes by chemical or electrochemical oxidation of the monomers, are mobile and interfere with the operation of the device [87]. Apart from the issue associated with the dopant mobility, controllable and homogeneous doping in conjugated polymer is quite awkward.

### 2.2.2 Qualitative Description of Transistor Operation



The operating modes of PFET differ from the conventional inorganic MISFETs, albeit the basic principle of both the devices is similar. PFET does not operate in *inversion* mode unlike traditional MISFET, but operates in *accumulation* mode [88]. In the case of conventional inorganic MISFET

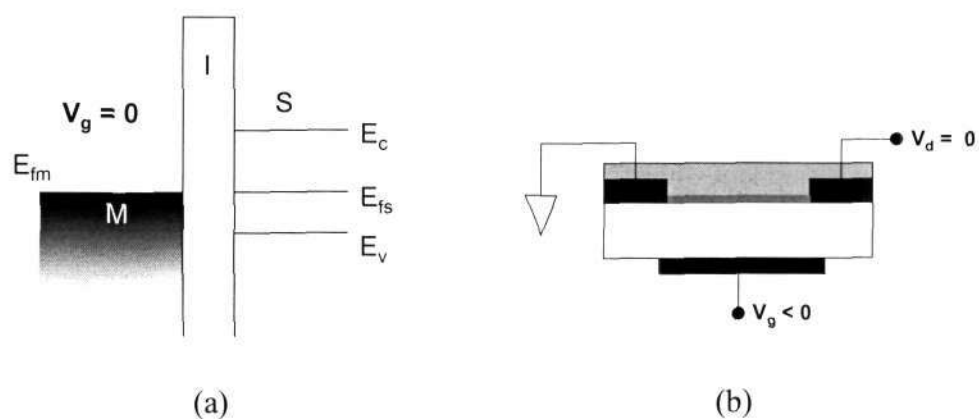


**Fig. 2.2** (a) Energy diagram of metal-insulator-semiconductor (MIS) structure for flatband condition ( $V_g = 0$ ).  $E_{fm}$ ,  $E_c$ ,  $E_v$  and  $E_{fs}$  represent Fermi level of metal, lowest energy level of conduction band, highest energy level of valence band and Fermi level of semiconductors, respectively. (b) Schematic diagram of FET structure with coplanar geometry under flatband condition.

structures, the channel region gets isolated from the bulk of the semiconductor due to the formation of a depletion layer in between. But in the case of OFET/PFET under accumulation mode, there is no distinct separation between

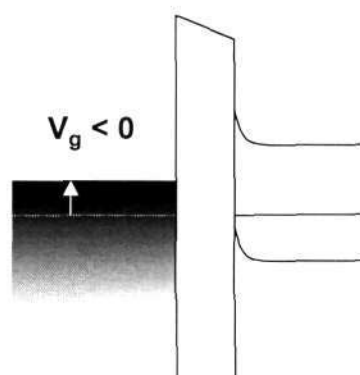


**Fig. 2.3** Energy diagram of MIS structure in accumulation mode ( $V_g < 0$ ).

the channel and the bulk, except the abrupt gradient of charge concentration. In contrast, OFET/PFET operates only in *accumulation* mode and the reason

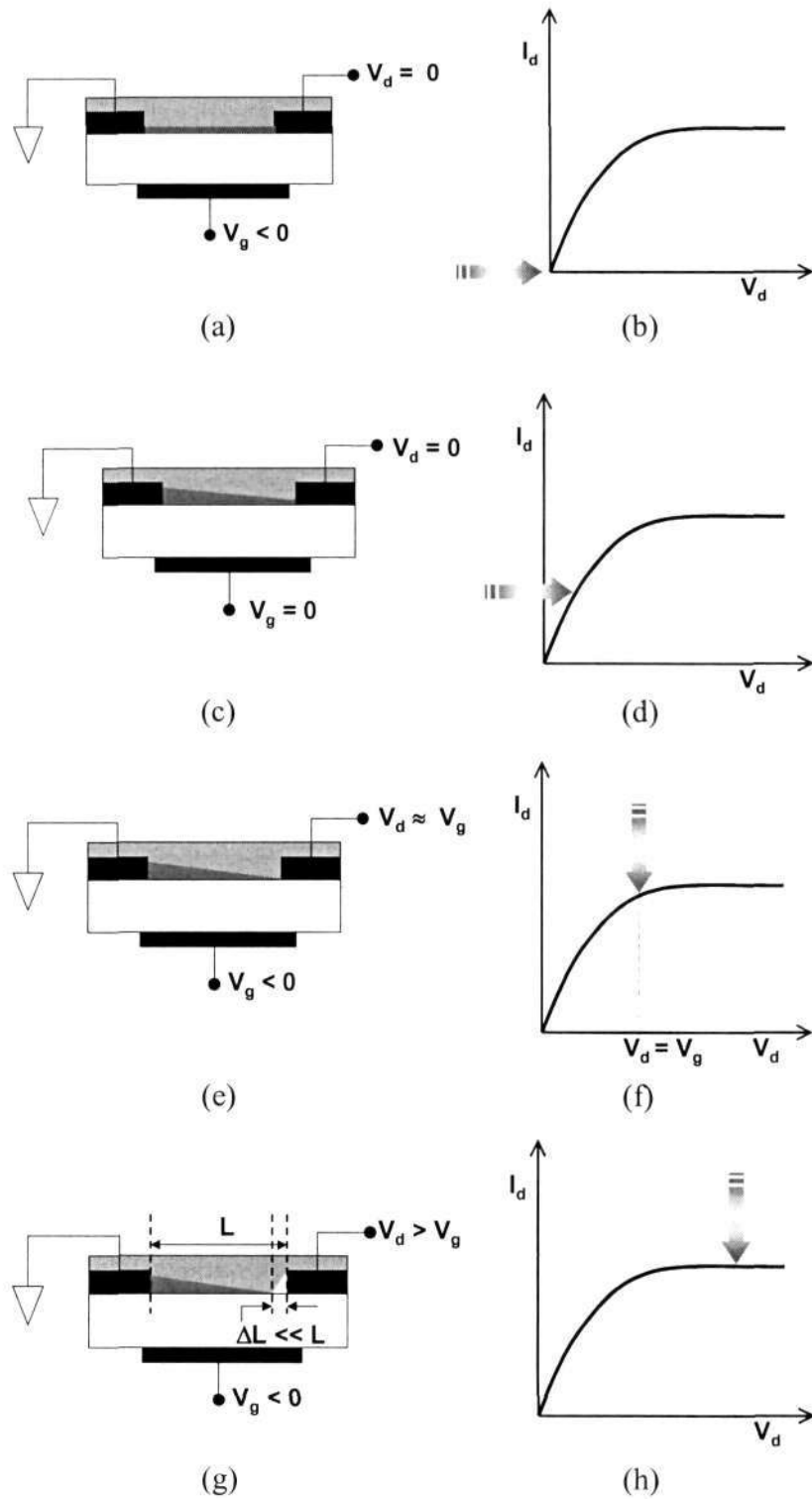


**Fig. 2.4** Schematic representation of charge distribution and the corresponding output characteristics of PFET in accumulation ( $V_g < 0$ ). The gray regions, white regions and deep gray regions indicate the semiconductor, insulator and conducting channel, respectively..

behind why those devices are not operable in inversion mode is clearly not yet

understood [88]. This invokes a noticeable contribution from the bulk in output characteristics of OFET/PFET. Though the operating modes of OFET/PFET differ from the conventional inorganic MISFETs, the operation principle remains always the same.

The operation of OFET/PFET is classified into two different modes namely accumulation and depletion modes and they are differentiated with the polarity of gate voltage and it is denoted by  $V_g$ . Under  $V_g = 0$ , no band-bending takes place and the condition is known as *flat-band* condition (Fig. 2.2a & 2.2b). For a *p*-type semiconductor, drain is subjected to negative bias ( $V_d$ ) with respect to source (ground) and the current flows from the source to drain. Upon applying negative  $V_g$  ( $V_g < 0$ ), the energy bands bend towards upward direction, while drawing positive charge carriers near the interface region of width typically 3-5 nm (Fig. 2.3). This mode is known as accumulation mode. The region containing large charge concentration that is responsible for the high conducting state is called the *channel* (Fig. 2.4 a-h). It is noteworthy to mention that a uniform distribution of surface charge density persists in the channel region when the drain-source are short-circuited ( $V_d = 0$ ). With increase in  $V_d$  ( $V_d < 0$ ), a gradient of charge density from the source to the drain appears along the channel due to its spatial dependency along the channel. This situation promotes a reasonable amount of  $I_d$ , which continues to increase almost linearly with  $V_d$  ( $0 < |V_d| < |V_g$ ). This region in current-voltage characteristic is referred to as *linear region* (Fig. 2.4c & 2.4d). As  $V_d$  is increased, it eventually reaches a point ( $V_d \approx V_g$ ) where the channel depth at the drain reduces to zero due to no effective voltage difference between the gate and the drain. The corresponding drain voltage is known as the *pinch-off* or *saturation* voltage (Fig. 2.4e & 2.4f). Beyond this voltage, the pinch-off point moves towards source, forming a small-depleted region around the drain. The carriers that arrive at the pinch-off point are injected from that point to the depleted zone around the drain. Since the number of charge carriers arriving at pinch-off point is essentially invariant with respect to the drain voltage, the current thereafter saturates to a constant value. This region is called the *saturation* region (Fig. 2.4g & 2.4h). In addition

to this feature, ohmic current arising due to the residual conductivity from the bulk must be taken into account along with thickness dependency of the semiconducting layer.

Upon reversal of  $V_g$  ( $V_g > 0$ ), the energy bands bend downward at the interface to compensate the corresponding electric field (Fig. 2.5a & 2.5b). This leads to charge depletion at the interface, resulting in low conductivity. Under

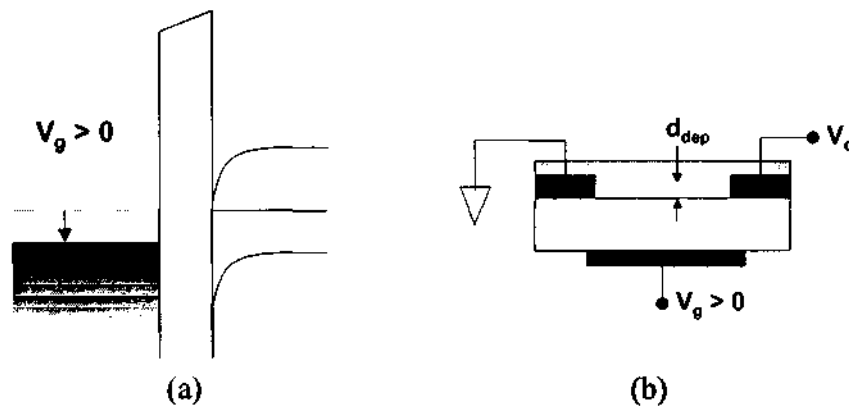


**Fig. 2.5** Energy diagram of MIS structure in depletion mode ( $V_g > 0$ ) and the corresponding charge distribution in PFET.

this circumstance, even if the drain-source voltage ( $V_d$ ) is raised to a negative value, there should be no drain-source current ( $I_d$ ) ideally. However, appreciable current flows through the bulk as anticipated from the residual bulk conductivity (Fig. 2.1b). This residual conductivity can be reduced to some extent by applying highly positive voltage to the gate ( $V_g \gg 0$ ), when the entire semiconductor is depleted from any mobile-charge carriers.

### 2.2.3 Theoretical Modeling of Organic/Polymeric Transistor Characteristics

In order to derive the transistor characteristic of OFET/PFET structure quantitatively, it is convenient to assume the idealized conditions: (i) the gradient of transverse field that is directed perpendicular to the channel is much larger than that of longitudinal field along the channel, (ii) there are no interfacial traps or difference in Fermi level between the gate and the semiconductor, (iii) carrier mobility is constant throughout the channel, and (iv)

reverse leakage current is negligibly small. The first condition essentially means that the charge induced by the transverse field is much more effective than that by the longitudinal field. This eventually requires the channel length to be quite

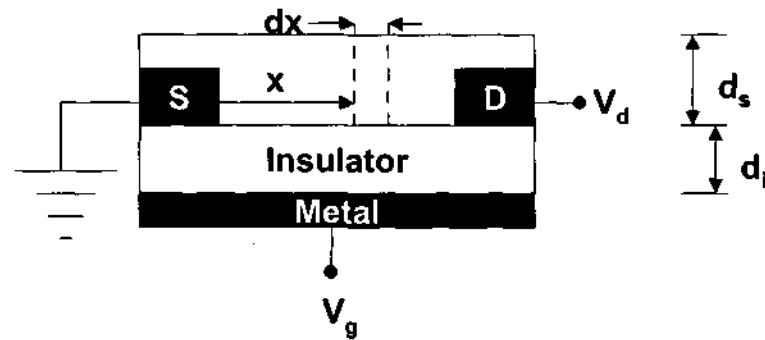


Fig. 2.6 Schematic representation of PFET with coplanar geometry.

larger compared to the insulator thickness. The condition is called *gradual channel approximation*, and it was first introduced by Shockley for modeling the traditional FET device characteristics [76].

The field-induced surface charge density is represented by the product of capacitance of the insulator per unit area ( $C_i$ ) and  $V_g$ . When a negative drain-source voltage is applied, a gradient of surface potential appears along the channel (say,  $x$ -direction). Under this circumstance, the conductivity is contributed by the following terms: (i)  $V_g$ -induced surface charge density and (ii) doping-induced charge density in the bulk of the semiconductor. In order to obtain the expression for transistor characteristics, we consider an incremental and infinitesimal section  $dx$  at a distance  $x$  from the source (i.e. source is at  $x = 0$ ) (Fig. 2.4). The conductance per unit area of this section is given by

$$dG = \frac{1}{dx} [Ne\mu Wd_s + C_i(V_g - V_x)W] \quad (2.1)$$

where  $N$  is the doping concentration,  $\mu$  the mobility of majority charge carriers,  $e$  the electronic charge,  $W$  the channel width and  $d_s$  the thickness of the semiconductor. If a current  $I_d$  flows, then the voltage dropped across the element is

$$dV_x = \frac{I_d}{dG} = \frac{I_d}{W} \left[ \frac{dx}{Ne\mu d_s + C_i(V_g - V_x)} \right] \quad (2.2)$$

On integration throughout, Eq. (2.2) turns into

$$\int_0^{V_d} [Ne\mu d_s + C_i(V_g - V_x)] dV_x = \frac{I_d}{W} \int_0^L dx \quad (2.3)$$

After rearranging the above equation, the current-voltage relationship follows

$$I_d = \frac{W\mu C_i}{L} \left( V_g - \frac{V_d}{2} \right) V_d + \frac{Ne\mu W d_s}{L} V_d \quad (2.4)$$

One can modify Eq. (2.4) further by introducing a small offset voltage ( $V_0$ ) equal to the difference between the Fermi levels of the semiconductor and the gate electrode, and the modified equation is as follows

$$I_d = \frac{W\mu C_i}{L} \left( V_g - V_0 - \frac{V_d}{2} \right) V_d + \frac{Ne\mu W d_s}{L} V_d \quad (2.5)$$

The first term is same as the conventional *inversion mode* MISFET devices and the additional term, is ohmic in nature, evidenced due to the doping in the bulk. This sizable contribution can only be removed by getting rid of unintentional doping. But the most efficient way to improve the performance of FET is to reduce the thickness of the semiconductor [89]. For a thinner sample ( $d_s \ll L$ ), transistor characteristic is governed by

$$I_d = \frac{W\mu C_i}{L} \left( (V_g - V_0)V_d - \frac{V_d^2}{2} \right) \quad (2.6)$$

The linear term predominates at lower drain voltage whereas the second term takes over as the drain voltage approaches to saturation voltage  $V_{d,sat} = V_g$  (assuming  $V_g \gg V_0$ ), which can be obtained by optimizing Eq. (2.6) with respect to  $V_d$ . In a saturation regime, one may consider that current-voltage (I-V) characteristic is independent of  $V_d$  and can be expressed as

$$I_d = \frac{W\mu C_i}{2L} V_g^2 + \frac{Ne\mu W d_s}{L} V_g \quad (2.7)$$

However, in reality, the saturation voltage exceeds  $V_g$  due to the presence of the residual charge in the bulk, which requires more voltage to be depleted at the drain region.

In depletion mode, when  $V_g \geq 0$ , the channel disappears and the current conducts through the undepleted bulk region (Fig. 2.1b). In order to establish the current-voltage relationship in depletion mode, it is essential to find the depletion width as a function of  $V_g$ . The extent of the depleted region can essentially be derived using *delta-depletion solution* [90]. Invoking the depletion approximation, in particular, Gauss's equation stands for

$$\frac{d^2V}{dx^2} = -\frac{Ne}{\epsilon_s} \quad (2.8)$$

where  $\epsilon_s$  is the permittivity of the semiconductor. Using the boundary conditions  $V = 0$  at  $x = 0$ ;  $V = U_s$  at  $x = d_{\text{dep}}$  and  $dV/dx = 0$  at  $x = d_{\text{dep}}$ , the extent of depletion zone becomes

$$d_{\text{dep}} = \sqrt{\frac{2\epsilon_s U_s}{Ne}} \quad (2.9)$$

Here  $U_s$  denotes the surface potential of the semiconductor. Noting that  $V_g$  in the ideal structure is dropped partly across the insulator ( $V_i$ ) and partly across the semiconductor, i.e.

$$V_g = U_s + V_i \quad (2.10)$$

where voltage drop across the insulator  $V_i = Ned_{\text{dep}}/C_i = (Ned_{\text{dep}}/\epsilon_i)d_i$ ,  $d_i$  and  $\epsilon_i$  are the thickness of the insulator and the permittivity of the insulator. Then Eq. (2.10) can be re-written as

$$V_g = U_s + \frac{Ned_{\text{dep}}}{\epsilon_i} d_i \quad (2.11)$$

Using Eqs. (2.9) and (2.11) and rearranging, one gets the expression for depletion width as

$$d_{\text{dep}} = \frac{\epsilon_s}{C_i} \left[ \left( 1 + \frac{2C_i^2 V_g}{Ne\epsilon_s} \right)^{1/2} - 1 \right] \quad (2.12)$$

The drain-source current in depletion mode (for  $V_g = 0$ ) can be written as

$$\begin{aligned} I_d &= \frac{Ne\mu W}{L} \int_0^{V_d} (d_s - d_{\text{dep}}) dV_x \\ &= \frac{Ne\mu W}{L} \left[ (d_s + P)V_d + \frac{2P}{Q} \left[ 1 - (1 + QV_d)^{3/2} \right] \right] \end{aligned} \quad (2.13)$$

with  $P = \epsilon_s/C_i$  and  $Q = 2C_i^2/Ne\epsilon_s$ . In a special case, for either low drain-source voltage ( $V_d \approx 0$ ) or high doping concentration ( $Q \approx 0$ ), this expression tends to

$$I_d = \frac{Ne\mu W d_s}{L} V_d \quad (2.14)$$

This is the ohmic current, which also appears in accumulation mode and carries the identity of negligible depletion. If depletion is not negligible, then the current reaches a maximum value and saturates due to the complete depletion at the drain contact. The corresponding voltage, called the pinch-off voltage  $V_p$ , can be derived by manipulating Eq. (2.12) as

$$V_p = \frac{Ned_s}{2C_s} \left( 1 + 2 \frac{C_s}{C_i} \right) \quad (2.15)$$

This gives rise to a maximum current for  $V_d \geq V_p$  of the form

$$I_d = \frac{WN^2 e^2 \mu d_s^2}{6LC_s} \left( 1 + 3 \frac{C_s}{C_i} \right) \quad (2.16)$$

The performance of FET, especially in digital application, is characterized by on/off ratio, which is defined as the ratio of the saturation current to that under  $V_g = 0$ . There are two extremes for on/off ratio; one is for heavy doping and the other for weak doping. For heavy doping, on/off ratio takes the form

$$\frac{I_{d,\text{on}}}{I_{d,\text{off}}} = 1 + \left( \frac{\mu}{\sigma} \right) \frac{C_i V_d}{2d_s} \quad (2.17)$$



where  $\sigma = Ne\mu$ , is the conductivity of the semiconductor. On the other hand, for lightly doping, it turns out to be

$$\frac{I_{d,on}}{I_{d,off}} = \frac{(\mu C_i/2)V_{d,sat}^2 + Ne\mu d_s V_d}{(N^2 e^2 \mu d_s^2 / 6C_s)(1 + 3C_s/C_i)} \quad (2.18)$$

Considering  $(\mu C_i/2)V_{d,sat}^2 \gg Ne\mu d_s V_d$  and  $3C_s/C_i \gg 1$ , the on/off ratio reduces to

$$\frac{I_{d,on}}{I_{d,off}} = \left(\frac{\mu}{\sigma}\right) \frac{C_i^2}{Ned_s^2} V_{d,sat}^2 \quad (2.19)$$

It is evident from Eq. (2.17) that high on/off ratio essentially requires thin films of semiconductor with high ratio of mobility to conductivity and insulators with high capacitance per unit area. In case of a lightly doped semiconductor, the on/off ratio will be enhanced due to low current in off-state, which is evidenced in the Eq. (2.19).

#### 2.2.4 Conductivity Versus Mobility

For a conjugated polymer, the conductivity does not vary linearly with the carrier concentration like inorganic semiconductor but it was observed that the relationship follows a power law behavior [91,92]. This is a consequence of the variable range hopping transport, which prevails in conjugated system. In such system the density of states at the Fermi level increases with doping. It is thus expected that both the conductivity and the field-effect mobility should increase upon doping. In the steady state, the field-induced charge will populate the lowest unoccupied states at the Fermi level. With increased doping, there is a higher density of states (DOS), which eventually enhances hopping process at the Fermi level and hence a higher mobility is observed for more heavily doped samples. The observed dependence of the conductivity on the concentration of dopants can be fitted by a power law

$$\sigma \propto N^\gamma \quad (2.20)$$

which leads to the relationship between the conductivity and the mobility as

$$\mu \propto \sigma^\delta \quad (2.21)$$

with  $\delta = 1 - (1/\gamma)$ . It was observed for a wide range of polymer materials that an empirical universal relationship appears between the conductivity and the mobility with  $\delta \approx 0.76$  [92]. The same relationship has been reported using simulation based on three-dimensional Mott's VRH model [93]. Thus the mobility is controlled by the quantity of dopant present irrespective of whether the dopant is intentionally or unintentionally introduced. The ratio ( $\mu / \sigma$ ) decreases with increasing conductivity and so does the on/off ratio. This means that doping increases the mobility and allows higher frequency transistors to be constructed though with a poor on/off ratio.

### 2.2.5 Concept of Threshold Voltage and Switch-on Voltage

The device geometry operation of OFET/PFET too differs from that of conventional inorganic MISFET. In general, a typical *n*-channel MISFET consists of two  $n^+$  regions diffused in a *p*-type substrate to form the drain and the source electrodes. An insulating layer is grown on top of the *p*-substrate, followed by deposition of the gate electrode atop the insulator. When the gate terminal is subjected by a voltage with proper sign (positive for an *n*-type channel), an inversion layer is induced at the insulator-semiconductor interface, thus forming a conducting channel between the source and drain. This has two consequences: First, the source and drain regions, along with the conducting channel between them, are isolated from the substrate by a *depletion layer*. Secondly, the conducting channel only forms after the gate voltage is beyond the so-called *threshold voltage*, that is, the onset voltage for the strong inversion regime. In fact, the threshold voltage is the gate bias where the Fermi level at the insulator-semiconductor interface crosses the middle of the gap [76]. On the contrary, the scenario is merely different in OFETs, which operate in the accumulation regime under the influence of negative gate bias for *p*-type semiconductor. In such geometry, there is no depletion layer to isolate the conducting channel from the substrate. Consequently the concept of threshold voltage in OFET has no clear physical basis [94]. Nevertheless, classical MISFET theory is often used to extract a threshold voltage, denoted by  $V_{th}$ ,

from the transfer characteristics of OFETs in accumulation mode. In order to take the  $V_g$ -dependence of field-effect mobility into account, several groups have extracted the transport parameters by using an empirical relation  $\mu = K(V_g - V_{th})^\gamma$  where  $K$ ,  $\gamma$ ,  $V_{th}$  are the fit parameters. However, further analysis using the empirical relation or classical MISFET theory has resulted in temperature dependence of  $V_{th}$  as high as 15 V in the temperature range 300–50 K [95]. This is practically unreasonable. Despite the apparent  $V_{th}$  as the characterization parameter, it is preferable to use *switch-on voltage* or *turn-on voltage* ( $V_{so}$ ), which signifies the gate voltage corresponding to the flatband condition, i.e., when there is no band bending in the semiconductor [96]. Below the switch-on voltage, there is no appreciable variation of channel current with  $V_g$ , while the channel current increases with  $V_g$  above  $V_{so}$ . For an unintentionally doped semiconductor layer,  $V_{so}$  is determined by fixed charges in the insulator layer or at the semiconductor-insulator interface and is observed to be in the range of 1–2.5 V, being a temperature independent factor [96].

### 2.2.6 Field-Effect Mobility Versus Bulk Mobility

The electrical performance of FET is commonly characterized by the mobility, thus by definition, the average drift velocity acquired by the charge carriers under the influence of unit electric field. In particular, mobility signifies the switching strength of the gate voltage to control the drain-source current and the on/off ratio. In case of PFET (or OFET), charge transport is solely governed by two types of mobility associated with the field-effect dominated current and the bulk dominated current. The field-effect current is contributed by the induced charge near the semiconductor/insulator interface whereas the dopant density influences the bulk counterpart in the system. When the bulk conductivity is not negligible, one can clearly observe the crossover from field-effect dominated current to bulk dominated current in the transfer characteristics of a disordered organic transistor. The decoupling of those two processes mainly arises due to the dependence of mobility on the dopant density of such material unlike the conventional inorganic single crystalline semiconductors.

The field-effect mobility is estimated from the transfer characteristics of the device. Since the output characteristics of transistor has linear and saturation regions, as manifested in Eq. 2.5, the mobility can be defined by two ways. In linear region (for low values of  $V_d$ ), mobility can be expressed as (from Eq. 2.6)

$$(\mu)_{\text{linear}} = \left( \frac{L}{WC V_d} \right) \frac{\partial I_d}{\partial V_g} \Bigg|_{\text{linear}} \quad (2.22)$$

Similarly for the saturation region it takes of form (from Eq. 2.7)

$$(\mu)_{\text{saturation}} = \left( \frac{L}{WC} \right) \frac{\partial^2 I_d}{\partial V_g^2} \Bigg|_{\text{saturation}} \quad (2.23)$$

Alternatively, the field-effect mobility in saturation regime is also estimated from the slope of the plot of  $(I_d)^{1/2}$  against  $V_g$  for  $|V_d| > |V_g|$ . Typically, the mobility calculated in the saturation regime is much higher than that of calculated value in the linear regime and the reason being is that later factor is having more negatively affected by deviations from linearity in the transistor characteristics ( $I_d$  versus  $V_d$  curves), at low  $V_d$ . The field-effect mobility is a very sensitive parameter and depends on several internal and external factors. It is mainly affected by semiconductor/insulator interface, orientation of the polymers or organic molecules, morphology, grain size (for organic molecules and oligomers), carrier density, impurity concentration etc. It is also influenced by the external parameters  $V_g$  and temperature.

The concept of switch-on voltage can be used to extract the dopant density and the bulk mobility [97]. For a small  $V_d$ , the depletion layer becomes almost uniform in thickness and can be re-written as

$$d_{\text{dep}} = \frac{\epsilon_s}{C_i} \left[ \left( 1 + \frac{2C_i^2 (V_g - V_{so})}{Ne\epsilon_s} \right)^{1/2} - 1 \right] \quad (2.24)$$

In pinch-off condition,  $V_g - V_{so} = V_p$ , at which the extent of depletion layer equals the thickness of the semiconductor, the dopant density can be extracted from the following relation

$$N = \frac{2V_p}{e(d_s^2/\epsilon_s + 2d_s d_i/\epsilon_i)} \quad (2.25)$$

In order to determine the bulk mobility, we consider the flatband condition ( $V_g = V_{so}$ ) and impose the condition that the bulk conduction should follow ohmic behavior. With the knowledge of the dopant density obtained from Eq. (2.25), therefore bulk mobility can thus be estimated, as follows.

$$\mu_{\text{bulk}} = \left[ \frac{LI_d}{NeWd_s V_d} \right]_{V_g=V_{so}} \quad (2.26)$$

The current in depletion mode is modeled by

$$I_d = \frac{Ne\mu_{\text{bulk}}WV_d}{L} (d_s - d_{\text{dep}}) \quad (2.27)$$

For example, it was observed that for P3HT sample N,  $\mu_{\text{lin}}$  and  $\mu_{\text{bulk}}$  are on the order of  $10^{16} \text{ cm}^{-3}$ ,  $10^{-3} \text{ cm}^2 \text{ V}^{-1} \text{ s}^{-1}$  and  $10^{-5} \text{ cm}^2 \text{ V}^{-1} \text{ s}^{-1}$  respectively [97].

### 2.2.7 Dependence of Field-Effect Mobility on Gate Voltage and Temperature

The gate voltage dependency of field-effect mobility is a common feature in the case of OFET. The variation of the mobility as a function gate voltage is more evident in the transfer characteristics showing continuously varying slope of  $I_d$  with respect to  $V_g$ . The kind of observable trend can be explained on the basis of multiple trapping and release (MTR) model, which is widely used to model the electrical response of amorphous hydrogenated-silicon TFTs [98]. The model has been successfully adopted in OFETs based on oligothiophene [99,100]. This model is, however, limited to the disordered materials where the mobility changes with temperature. According to MTR model, the deeper traps are filled first and then carriers can be released with the aid of thermal agitation. At low gate bias, nearly all induced charges are trapped into these localized states where their mobility is very low. As the gate bias increases, the Fermi level approaches to the delocalized band edge and the traps will be filled. Above threshold gate voltage, we assume that all trap states are filled and effective mobility reaches a critical value, which corresponds to the value of *trap-free mobility*. Recent reports on oligothiophene-based OFET devices, an exponential DOS type of distribution has been proposed to corroborate the  $V_g$ -dependent

mobility to get deeper insight in current-voltage (I-V) characteristics [100]. In spite of possessing basic and valid insights in transistor characteristics, this model shows several discrepancies. Firstly, the trap-free mobility found in sexithiophene (6T)- and dihexyl sexithiophene (DH6T)-based OFETs is low. Despite the charge transport through extended states that is assumed in MTR model, the estimated concentrations of traps are rather high when compared to the total density of molecules in the materials. Finally, the measurements on single crystals show that the trap-free mobility of 6T could be at least one order of magnitude higher than that obtained from the model. This kind of inconsistencies has been rectified by introducing the effect of contact resistance that arises at the drain and source electrodes [101]. It is to be noted that the corrected mobility does not saturate with gate bias, in contrast with the uncorrected counterpart as in the case of latter, the observed mobility saturates to a trap-free's mobility value.

Temperature is another crucial parameter having a profound impact on the field-effect mobility of OFET and PFET devices. Early report on temperature dependency of mobility in FETs based on poly(thienylene vinylene) (PTV) and pentacene showed an Arrhenius-type behavior [92]. Moreover, the gate voltage-dependent activation energy was also observed. This was interpreted in the framework of polaronic type of hopping transport mechanism. The spatial disorder induces localized states that are located deep in the gap. The induced charge carriers primarily occupy these deep states. At more gate bias, the Fermi level moves towards the energy level typical of the polaronic levels in the material. The charge transport takes place by thermal activation from the localized polaronic states at the Fermi level to a large density of localized states at certain transport level. In this model the activation energy was referred to as the polaronic binding energy. However, the situation becomes different for heavily doped conjugated polymer-based FET, because the DOS within the gap is high so that the charge transport is dominated by variable range hopping at the Fermi level.

A comprehensive model has been developed more recently to express the gate voltage- and temperature-dependent mobility. This model is based on VRH with an exponential distribution of localized states [102]. According to this model, an applied gate voltage gives rise to the accumulation of charge carriers, which occupy the lower-lying states of the organic semiconductor. With increase in gate bias, the newly introduced charge carriers occupy the states at relatively high energies so that they require less activation energy to hop away to the nearest neighbouring site. This results in a higher mobility with increasing gate voltage. Using the percolation theory the mobility is expressed as

$$\mu = \frac{\sigma_0}{e} \left[ \frac{\pi(T_0/T)^3}{(2a)^3 B_c \Gamma(1-T/T_0) \Gamma(1+T/T_0)} \right]^{T_0/T} \left[ \frac{(C_i V_g)^2}{2k_B T_0 \epsilon_s} \right]^{T_0/T-1} \quad (2.28)$$

Here,  $a$  is an overlap parameter that characterizes the tunneling of charges from one site to other,  $T_0$  is the characteristic temperature of the exponential distribution, which was observed to be approximately 380–385 K (for pentacene and polythienylene vinylene),  $\sigma_0$  and  $B_c$  are constants, and  $B_c$  represents the critical number of bonds reached at percolation onset.

A different approach has been proposed recently to locate the origin of temperature and gate voltage dependency of mobility in 6T-based OFETs, when a high density of trapped charges as compared to that of free charges is present in the system [103]. In this model, the standard FET theory has been modified using a power law relationship between  $\mu$  and  $V_g$  with a temperature-dependent exponent. The observed stretched-exponential behavior of the transients is due to the slow relaxation of the trapped carriers and the retrapping events. Moreover, in this system an abrupt drop of the field-effect mobility was observed beyond 200 K. This drop was attributed to the concomitant increase in creation of new trap states rather than that of exponential ionization from the traps.

### 2.2.8 Nature of Self-localized Charge Carriers in PFETs

The charge species involved in polymer field-effect transistors are likely to be self-localized instead of being free charge carriers as in the case of their traditional inorganic counterparts. It is thus essential to identify the nature of the excess charge carriers that are induced by gate bias. Charge modulation

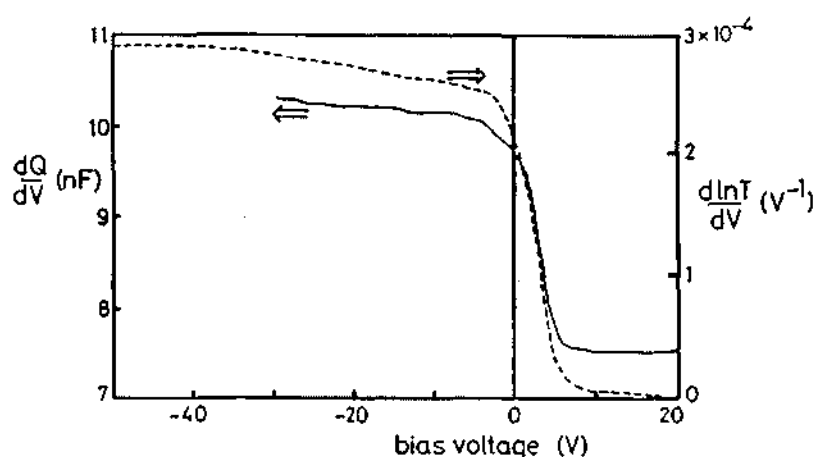


Fig. 2.7 The differential optical transmission,  $\partial \ln T / \partial V$  at 0.8 eV and differential capacitance  $\partial Q / \partial V$  versus  $V_g$  for a polyacetylene MIS structure. Courtesy: Ref. [104]

spectroscopy (CMS) is one of the powerful techniques to directly probe the charge carriers existing in the conducting layer of FET without isolating the chains in solution or introducing the presence of perturbing counter ions. The basic principle of the experimental technique is to modulate the charge density by modulating the gate bias in a transparent/semi-transparent metal-insulator-semiconductor (MIS) diode structure and to monitor the associated change in transmission coefficient using lock-in measurements. CMS technique was used to adopt in MIS structure consisting of polyacetylene as a semiconducting layer on top of insulating silicon dioxide and heavily doped silicon as gate in a row [104]. With increasing gate bias in accumulation mode, there was a clear reduction of transmission in the energy scale ranging from 0.4 eV to 1.2 eV with a peak around 0.8 eV, as shown in Fig. 2.7. This indicates the accumulation of charge carriers in the polymer chain reducing the differential transmission signal, defined as  $\Delta T^* / T^*$ , where  $T^*$  is the transmission coefficient



of the system. In particular, the energy value assigned to 0.8 eV correspond to the population of mid-gap states or the formation of localized *solitons*. The prominent signature of soliton formation was justified by scaling the differential variation of transmission ( $\partial \ln T^* / \partial V_g$ ) with that of the induced charge ( $\partial \ln Q / \partial V_g$ ), as the gate bias was varied. The similarity between the two curves is evident as in the case of soliton-like states observed in polyacetylene film.

The kind of similar trend was observed in MIS-diode structure based on regioregular poly(3-hexylthiophene) (RRP3HT), where RRP3HT is a non-

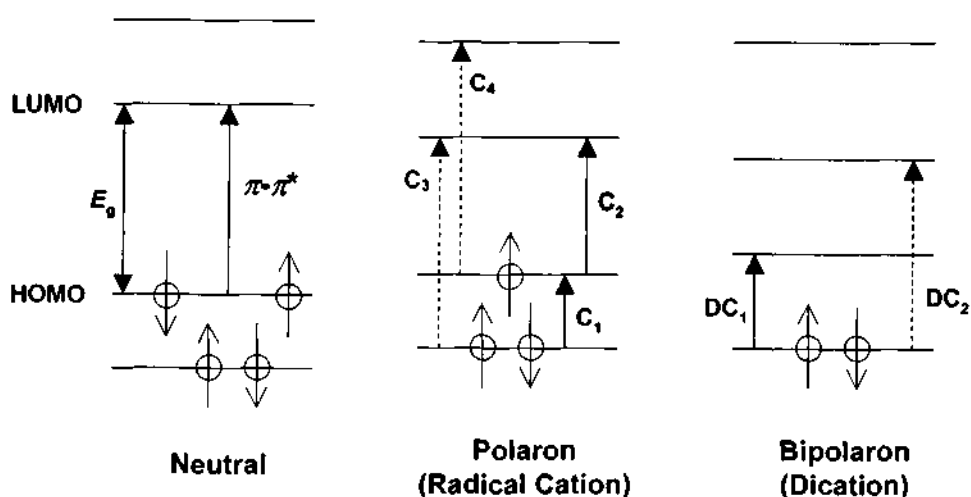


**Fig. 2.8** The molecular energy levels of a 1D thiophene chain for neutral, singly and doubly charged species.

degenerate ground state polymer with the highest ever known field-effect mobility [105,106]. In such system, the induced charged species are stored as either *polaron* or *bipolaron* and/or mixed of both. According to the molecular energy level scheme of one-dimensional thiophene chain, there should be utmost four transitions for polarons and two for bipolarons. However, considering symmetry criteria for isolated chain, two of the polaronic transitions and one of the bipolaronic transitions are optically allowed. In particular, three structureless sub-band features appeared in CMS study of the device. The nature of the features was unchangeable upon variation of temperature, modulating frequency and voltage except marginal change in the magnitude. The conclusion of the results can be summarized as: (i) The charge species in MIS diode or PFET structure are likely to be polaronic kind of species rather than

diode or PFET structure are likely to be polaronic kind of species rather than bipolaronic in nature. Because in case of bipolarons, one should expect a noticeable feature as a function of temperature and voltage since the bipolarons are unstable at higher temperature and low carrier concentration. (ii) The appearance of three transitions is a signature of polaron as for bipolarons maximum two transitions are possible (Fig. 2.8). (iii) The strongest feature corresponding to the C3 transition is an indication of strong interchain interaction. Thus the charge transport in RRP3HT-based PFET is polaronic in nature. The similar polaronic feature has also been confirmed recently by using electron spin resonance (ESR) spectroscopy on MIS diode structure consisting of regioregular poly(3-alkylthiophene) (RRP3AT) as the semiconducting buffer layer [107].

### 2.3 DEVICE FABRICATION

The fabrication of silicon-based or traditional inorganic semiconductor-based MISFET structure involves either diffusion or implantation based processes, where source and drain electrodes deposition followed by the growing of insulating layer, normally thermally grown silicon oxide, and finally deposition of the metal electrodes. In OFETs (or PFETs), the semiconductor is not a bulk substrate but a thin film and so the device structure is fabricated in an *inverted* architecture like TFTs. Typically the OFET structures are designed in two different categories. In *coplanar* (or *bottom-contact*) geometry, all the layers are on the same side of the semiconductor, whereas in *staggered* (or *top-contact*) geometry, the gate and the source-drain are on opposite sides of the semiconductor layer.

Coplanar configuration is the most adopted geometry for OFETs due to its significant advantages especially in integrated circuit (IC) applications. It is easier to fabricate the bottom-contact device with miniaturized dimension using different types of lithographic techniques without damaging the soft polymer films. In addition to that, the bulk-controlled current becomes less effective in this geometry. The main demerit of this device structure is high contact

resistance at the drain and source regions, which dominates in case of short-channel device and has injection limited nonlinear transport. The origin of high resistance lies on the fact: (i) under etching of the drain and source electrodes forming air gap between the electrodes, semiconductor and the insulator [108], (ii) small contact area between metal and semiconductor ( $\approx d_m \times W$ , where  $d_m$  is the thickness of the metal deposited) [109]. On the other hand, in staggered geometry the contact resistance is less susceptible than that in the coplanar geometry as the contact area in former (in particular, overlap of the source and gate contacts) is large enough. Besides this, there is a component of electric field pointing vertically up that can induce injection from the top of the source. But there are severe limitations in this architecture like (i) restricted channel length due to lack of lithographic technique, (ii) possibility of damage of the polymer film, (iii) bulk dominated current depending on the thickness of the semiconductor film.

Most of the PFETs have been constructed on highly doped silicon wafers covered with a thermally grown silicon oxide layer. The highly doped substrate acts as the gate electrode. In case of coplanar structure, the source and drain electrodes are designed on top of the insulating layer using standard microlithography techniques prior to the deposition of semiconductor. In a staggered configuration, the semiconductor is deposited, followed by the thermally evaporated metal electrodes (drain and source) using shadow-mask with desired dimension.

### 2.3.1 Deposition of the Semiconductor

The most crucial step for FETs is the deposition of semiconductor. There are various deposition techniques that are adopted depending on the nature of the semiconducting material.

*Vacuum Evaporation* is a useful method to deposit the organic small molecule on the insulating surface by heating the material under high vacuum conditions. The organic material is placed on a high-temperature withstanding metal boat (made of molybdenum, Tungsten or stainless steel) and that is placed

few centimeters beneath the substrate. The base pressure of the deposition system is an important parameter to control the mean free path of the sublimed organic molecules and presence of unwanted atoms and molecules, which results in contamination in the polymer film. The pressure range is of the order of  $10^{-9}$  torr in UHV organic molecular beam deposition [110] to  $10^{-3}$  torr for simple, glass-wall vacuum sublimation system [111]. Substrate temperature and deposition rate also influence the thin film morphology and so to the transport characteristics of OFETs [112]. The advantages of vacuum deposition are (i) easy control in thickness value, and (ii) purity of the film with the possibility of high ordered film by monitoring the deposition rate and the temperature of the substrate. The main drawback of this kind of deposition technique is the requirement of sophisticated instrumentation, which deters the low-cost processing of its counterparts.

**Solution-Processed Deposition** is the most elegant and easy way to obtain high quality polymer film over a large area. This technique involves the homogeneous deposition of polymer film from its solution by using *spin-casting* [H. Sirringhaus 1998], *drop-casting* [113], *printing technology* [25], *dip-coating* [114] or *Langmuir-Blodgett (LB)* technique [115]. A basic requirement for this technique is good solubility of the polymer in known common organic solvents. But most of the polymers, in pristine form, are sparingly soluble in nature. This hindrance was circumvented by grafting solubilizing groups to the polymer backbone [116] or by using a soluble precursor polymer, which finally converted to the conjugated polymer by an appropriate physical or chemical treatments [11,117].

*Spin-casting* is one of the most widely used methods for solution-processed deposition, where the substrate is rotated at a speed of few hundred to few thousand round per minute after dropping an appropriate amount of solution on it. Uniform thickness can be maintained by optimizing the coating parameters such as viscosity of the solution and rotation speed. Typically the film thickness is proportional to the viscosity and inversely proportional to the rotation speed. *Drop-casting* is another deposition scheme in which the solution is allowed to

dry slowly in inert or ambient atmosphere. This is comparatively a slow-growing process with natural evaporation of the solvent. A comprehensive study dealing with the comparison between spin- and drop-casting and their influence in mobility and orientation of the film has been carried out recently [118]. *Printing technology* is the technique that has attracted contemporary interest for the development of organic electronics towards future direction. This method involves printing of the conducting or conjugated polymers, which can be used as a form of *suspension* or *ink*. The primary goal of this technique includes the fabrication of ICs at a far greater production speed, lower cost, and with less manufacturing complexity incorporating the possibility of processing at room temperature in ambient atmosphere. *Dip-coating* is one of the efficient processing method to achieve large area devices in both side of the substrate. In this process, the substrate is dipped into the polymer solution in a repeated and automated manner. *Langmuir-Blodgett (LB)* technique has also been explored in polymer electronics. It allows a fine control of both the structure and thickness of the film. This technique is limited to amphiphilic molecules that consist of a hydrophobic chain and a hydrophilic head group. Though most of the common organic molecules or polymers for FETs are not of this category, LB-grown OFET and PFET have been reported elsewhere [115,119,120]. However, the necessitate mixing of the electrically active compound with an inactive compound substantially reduces the mobility as compared to that of a vacuum-evaporated film.

The major challenge in solution-processed technique lies on the interface property between the insulator and semiconductor, which is mainly the weak Van der Waal interaction leading to less mobility. The interface quality can be improved by using surface modification treatment prior to the deposition of the semiconductor [15,121]. In principle, silane-based compounds are used to develop the self-assembled monolayers on top of the dielectric. The surface treatment has led to the increase of the mobility even up to two orders of magnitude [121]. The purpose of surface treatment is to make the dielectric surface more hydrophobic in nature, which in turn attracts the side chain of the

polymers forming a highly ordered interface. An alternative method to improve the interface is surface-directed, self-organized bilayer of two organic bulk phases with spontaneous solvent evaporation and this recent work has been demonstrated by Sirringhaus and his co-workers [122].

### 2.3.2 Deposition of Metals and Their Role in Electrical Performance

Prior to (bottom contact) or after (top contact) the semiconductor deposition, metals such as Gold (Au,  $\phi_m = 5.1$  eV), Aluminum (Al,  $\phi_m = 4.2$  eV), Magnesium (Mg,  $\phi_m = 3.7$  eV), Calcium (Ca,  $\phi_m = 2.8$  eV), Silver (Ag,  $\phi_m = 4.6$  eV) provide drain and source contacts. The choice of the metals, depending on their work function ( $\phi_m$ ), is a crucial factor in determining the efficient charge transport mechanism in OFETs/PFETs. In most of the cases, the noble metal Au is the leading encompassing candidate used for the drain and

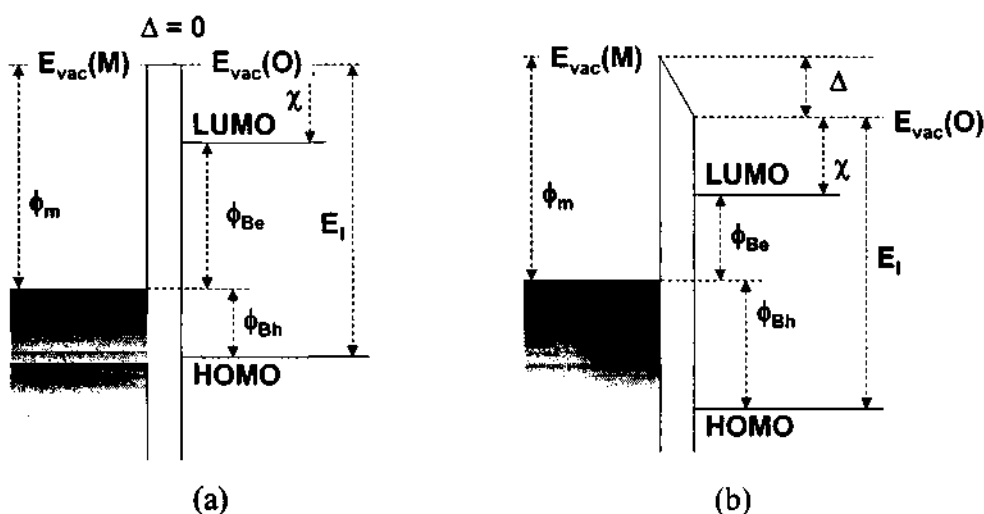


Fig. 2.9 Schematic diagram of metal-semiconductor interface (a) without any shift in energy level  $\Delta = 0$  and (b) with a finite shift  $\Delta$  due to interfacial electric dipole layer.

source contacts due to its matched work function to the HOMO level of the organic/conjugated polymers ( $\sim 5$  eV). Aluminum is generally used as gate electrode rather than drain and source electrodes, because it is unstable in air with high tendency to be oxidized. Indium tin oxide (ITO)-coated glass is also used more often due to its transparent behavior coupled with metallic feature.

Apart from the inorganic metals, water-soluble conducting polymer poly(3,4-ethylenedioxythiophene)/poly(4-styrenesulfonate) (PEDOT/PSS) is widely used to enhance the whole transport properties of organic/polymeric FETs.

The metal/semiconductor interface at the contacts plays a major role in the electrical performance of OFETs in terms of efficient carrier injection to the organic semiconductor. The efficiency of injected holes (or electrons) from the metal contact to HOMO (LUMO) of the organic semiconductor depends on the energy barrier  $\phi_{\text{Bh}}$  ( $\phi_{\text{Be}}$ ) and the holes (electrons) have to overcome the metal/semiconductor interface (Fig. 2.9). The origin of energy barrier is the position of the HOMO (for holes) and LUMO (for electrons) relative to the Fermi level of the metal that is used for the source or drain contacts. It is more straightforward from the energy level diagram that  $\phi_{\text{Bh}}$  is the difference between the ionization potential ( $E_{\text{I}}$ ) and the work function of the metal and similarly  $\phi_{\text{Be}}$  is the difference between the electron affinity, denoted by  $\chi$ , and  $\phi_{\text{m}}$ . However, it has been reported that this assumption is not always valid. A finite shift of the vacuum level ( $\Delta$ ) of the organic semiconductor was observed at the metal/semiconductor interface, whose magnitude and sign depend on the specific metal/organic combination [123,124,125]. This shift can be attributed to an ultrathin, interfacial electric dipole layer that can be as high as 1.5 eV [124–128]. The issue, related to barrier formation, becomes more evident in case of *n*-channel OFETs. In this context, it is essential to mention that despite the low work function of Al, it provides poor electron injection efficiency. This is likely due to (i) the oxidation of Al, which creates an insulating layer of aluminum oxide, and (ii) the formation of dipole barrier. For example, in case of N, N'-diphenyl-1,4,5,8-naphthyl-tetracarboxylimide (DP-NTCDI), the vacuum level in the semiconductor side of the interface with Al moves upwards by -0.2 eV, whereas for Au contact it moves downward by 0.9 eV [124]. As a result, the electron injection barrier is higher for the Al contact than that for the Au contact.

## 2.4 PROGRESS IN ELECTRICAL PERFORMANCE OF OFET

The performance of OFET in terms of mobility, on/off ratio, stability etc. has been improving continuously since its invention. Considerable research efforts have also resulted in an increase in field-effect mobility by five orders of magnitude over the past two decades. The typical route of impressive improvements can be summarized by the following processes: (i) synthesis of a new organic semiconductor or use of a known one for the first time as an active layer; (ii) optimization of the film deposition parameters for the active layer to obtain superior morphology and structural orientation; and (iii) optimization of injection from the source and drain contacts. Typically OFETs can be divided into two categories, *p*- and *n*-channels, according to the nature of charge carriers that form the conducting channel at the semiconductor/insulator interface. However, it is noteworthy to specify that *p*- or *n*-channel does not imply the type of doping unlike the inorganic counterparts, but it signifies the more mobile charge carriers, either holes or electrons respectively. Recently, extensive research is being conducted on design and optimization of *ambipolar OFET*, consisting of both type of charge carriers with balanced mobility.

### 2.4.1 Progress in *p*-channel OFETs

Most of the conjugated polymers and organic molecules that are used for OFET, offer *p*-type behavior in the output characteristics. The unintentional doping while synthesis and the appearance of electron-trapping centres at the semiconductor-insulator interface during fabrication process make them as convenient *p*-type conductors. The most widely used *p*-type organic semiconductors are pentacene, thiophene oligomers, and RRP3AT as active materials. One of the first solution-processable organic semiconductor, used for an efficient FET structure, was P3HT, in which the presence of alkyl side groups enhanced the solubility of the polymer chain [129]. The mobility value of the OFET based on P3HT, spun from the chloroform solution, was reported to lie in the range of  $10^{-5} - 10^{-4} \text{ cm}^2 \text{ V}^{-1} \text{ s}^{-1}$ . The insertion of side group(s) didn't affect the electrical property when mobility was comparable to that of obtained



from the electrochemically prepared polythiophene based PFET [130]. A comparative study of P3AT transistors as a function of the side chain showed that the mobility decreases from  $1\text{-}2 \times 10^{-4} \text{ cm}^2 \text{ V}^{-1} \text{ s}^{-1}$  for poly(3-butylthiophene) and P3HT to  $6 \times 10^{-7} \text{ cm}^2 \text{ V}^{-1} \text{ s}^{-1}$  for poly(3-decylthiophene) [131]. Regioregular P3HT based FET device structures consisting of 98.5% or more head-to-tail linkages have shown dramatic increase in mobility when compared to that of regiorandom P3AT based FETs [113]. With drop-casting method, the mobility was boosted to  $0.045 \text{ cm}^2 \text{ V}^{-1} \text{ s}^{-1}$  due to formation of a self-assembled lamella structure of RRP3HT film [113]. A comprehensive study on the correlation between the mobility and the deciding factors such as degree of regioregularity, deposition technique and orientation of polymer stacking atop the insulator surface was reported [118]. Highly regioregular P3HT (> 91% head-to-tail linkage) forms lamella with an edge-on orientation ( $\pi$ - $\pi$  stacking in the plane of the substrate) when spun from chloroform. High field-effect mobilities of  $0.05\text{-}0.1 \text{ cm}^2 \text{ V}^{-1} \text{ s}^{-1}$  were obtained for 96% RRP3HT based FET devices. In contrast, spin-coated films of P3HT with low regioregularity (81% head-to-tail linkage) causes lamella with a face-on orientation ( $\pi$ - $\pi$  stacking perpendicular to the substrate) resulting low field-effect mobility of the order  $2 \times 10^{-4} \text{ cm}^2 \text{ V}^{-1} \text{ s}^{-1}$ . However, drop-cast of 81% regioregular P3HT reproduces the edge-on orientation of lamella structure that increases the mobility by an order of magnitude ( $\sim 10^{-3} \text{ cm}^2 \text{ V}^{-1} \text{ s}^{-1}$ ). This study states that in addition to the degree of the order of the film, the method of deposition also influences the  $\pi$ - $\pi$  stacking direction relative to the substrate, which in turn has direct impact on the mobility of the materials. The mobility of RRP3HT is also influenced by the solvents used and the surface modification of the insulator. The mobility was observed to vary by almost two orders of magnitude, depending on the solvents, and the highest mobility was obtained using chloroform as the solvent for RRP3HT [113]. Modification of the insulator surface prior to deposition of RRP3AT improves the mobility. In case of RRP3HT-based FET, it has been observed that treatment of silicon dioxide with hexamethyldisilazane (HMDS) or alkyltrichlorosilane replaces the hydroxyl group at the silicon dioxide surface

with methyl or alkyl groups. The apolar nature of these groups apparently attracts the hexyl side-chains of P3HT, favoring lamella with an edge-on orientation. Mobilities of  $0.05\text{-}0.1\text{ cm}^2\text{ V}^{-1}\text{ s}^{-1}$  have been achieved using HMDS treatment to the insulator surface [15]. Recently, OFETs based on RRP3HT have been fabricated using dip-coating technique. The highest field-effect mobility value of  $0.18\text{ cm}^2\text{ V}^{-1}\text{ s}^{-1}$  has been recently reported. The origin of the high mobility was attributed to the formation of rod-like morphology [114,132]. However, exposure of RRP3AT to air causes an increase in conductivity, subsequent degradation of the transistor, and low on/off ratio is due to doping with oxygen. It has been shown to achieve high on/off ratios when the samples were at inert conditions[15,25].

Poly(9,9-dioctylfluorene-co-bithiophene) (F8T2) is another promising polymer semiconductor and more environmentally stable than P3HT [133]. F8T2 possesses a thermotropic, nematic liquid crystalline phase above  $265\text{ }^\circ\text{C}$  and oriented in plane on a rubbed polyimide alignment layer eventually quenched to room temperature to form a macroscopic domain. The carrier mobility is higher in the case of oriented films along the rubbing direction rather than in isotropic films and can be as high as  $0.02\text{ cm}^2\text{ V}^{-1}\text{ s}^{-1}$  and on/off ratio of  $10^5$  at room temperature [133,134]. The most promising aspect is the implementation of this conjugated polymer in ink-jet printing technology to design all-polymer transistor inverter-circuit with channel length down to  $5\text{ }\mu\text{m}$  [134]. The influence of different deposition techniques and surface modification of dielectric interface has been thoroughly reported [121]. A twenty-fold improvement over mobility on bare silicon oxide has been observed upon treating the dielectric surface with octadecyltrichlorosilane self-assembled monolayer.

Numerous efforts have been carried out on thiophene oligomers to improve and optimize the organic-based transistor characteristics. Especially sexithiophene (6T) played a major role in the evolution of the field of organic transistors. The first report on 6T-based FET, which was also the first report on a small conjugated molecule, showed the mobility on the order of  $10^{-3}\text{ cm}^2\text{ V}^{-1}\text{ s}^{-1}$

[86]. The importance of the ordering of the film was first realized with 10-100-fold increase of thiophene oligomers upon substitution of dimethyl at the both ends of oligomers [135]. The argument was confirmed using dihexylsexithiophene (DH6T) to obtain the mobility as high as  $0.05 \text{ cm}^2 \text{ V}^{-1} \text{ s}^{-1}$  due to the very regular microscopic arrangement [136]. Later on, proper purification treatment of the source materials, a high mobility of  $0.03 \text{ cm}^2 \text{ V}^{-1} \text{ s}^{-1}$  and on/off ratio  $\sim 10^6$  obtained are the highest reported values for unsubstituted 6T-based OFETs [137]. The variation of field-effect mobility with different polymer dielectric layer was studied thoroughly on DH6T/ polymethylmethacrylate (PMMA) ( $0.04\text{-}0.08 \text{ cm}^2 \text{ V}^{-1} \text{ s}^{-1}$ ), DH6T / polyimide ( $0.09\text{-}0.10 \text{ cm}^2 \text{ V}^{-1} \text{ s}^{-1}$ ) and DH6T / parylene ( $0.095\text{-}0.13 \text{ cm}^2 \text{ V}^{-1} \text{ s}^{-1}$ ) FET based materials [110].

Most of the impetus and recent research has been carried out on OFET consisting of *pentacene* (an organic molecule with five aligned condensed benzene rings belonging to the family of polyacenes). Over the past decade, pentacene has been proved to be a leading candidate for OFET due to its morphology and the crystalline property. Pentacene can be deposited using organic vapor phase deposition technique [138], solution processed method [139] and even pulse-laser deposition technique [140]. The successful implementation of pentacene in OFET was first reported in 1992 with field-effect mobility of  $2 \times 10^{-3} \text{ cm}^2 \text{ V}^{-1} \text{ s}^{-1}$ . The crystalline pentacene with controlled growth has remarkably high value of field-effect mobility ranging from 0.038 [112] to 0.62 [141] to  $1.5 \text{ cm}^2 \text{ V}^{-1} \text{ s}^{-1}$  [142].

#### 2.4.2 Progress in *n*-channel OFETs

The major problem in fabricating *n*-channel OFETs is the presence of traps. Even few traces of  $\text{O}_2$  are enough to degrade the device and acts as an electron trap. The protons of water, which can attach to the functional groups by hydrogen bond, also serve as additional trap-sites for electrons. However, the deciding factors for the device engineering are the electron affinity of the semiconductor and the energy level matching between the semiconductor and the metal electrodes (source and drain) to promote efficient electron injection.

An early study on using lutetium ( $\text{Pc}_2\text{Lu}$ ) and thulium ( $\text{Pc}_2\text{Tm}$ ) bisphthalocyanines-based  $n$ -channel OFET was reported, where the mobilities between  $2 \times 10^{-4}$  and  $1.4 \times 10^{-3} \text{ cm}^2 \text{ V}^{-1} \text{ s}^{-1}$  for both the materials [143].  $\text{C}_{60}$  and  $\text{C}_{60}/\text{C}_{70}$  fullerenes were also used as the active layer with mobility  $5 \times 10^{-4} \text{ cm}^2 \text{ V}^{-1} \text{ s}^{-1}$ . The mobility of  $\text{C}_{60}$  was raised to  $0.08 \text{ cm}^2 \text{ V}^{-1} \text{ s}^{-1}$  by modifying the deposition technique [144]. Further research has offered to a mobility of  $0.56 \text{ cm}^2 \text{ V}^{-1} \text{ s}^{-1}$  in  $\text{C}_{60}$ -based FET, which is quite reasonable value in  $n$ -channel transistor system [145]. It has recently been shown that OFETs based on  $N, N'$ -dioctyl-3,4,9,10-perylenetetracarboxylic diimide (PTCDI-C18H) as the organic semiconductor provides bottom contact devices with mobility as high as  $0.6 \text{ cm}^2 \text{ V}^{-1} \text{ s}^{-1}$  [111]. Apart from the organic molecules, polymers have been introduced in this race. There are only fewer reports available on  $n$ -type based FET device structures. Electron transport in an  $n$ -type conjugated polymer was investigated in FETs made from a ladder type polymer, so-called poly(benzobisimidazobenzophenanthroline) (BBL) spun from Lewis acid ( $\text{AlCl}_3, \text{GaCl}_3, \text{FeCl}_3$ ) [146]. The mobility was observed on the order of  $10^{-4} \text{ cm}^2 \text{ V}^{-1} \text{ s}^{-1}$ . Later on, the mobility of BBL was shown to increase up to  $0.1 \text{ cm}^2 \text{ V}^{-1} \text{ s}^{-1}$  by spin coating from methanesulfonic acid instead of Lewis acid [147]. The same group also found the  $n$ -type OFET using a series of binary blends of BBL and poly( $p$ -phenylene-2,6-benzobisthiazole) to obtain the mobility of  $5 \times 10^{-5} \text{ cm}^2 \text{ V}^{-1} \text{ s}^{-1}$  [148]. Field-effect mobilities of  $3\text{--}4 \times 10^{-3} \text{ cm}^2 \text{ V}^{-1} \text{ s}^{-1}$  were achieved in the encapsulated, bottom-gate FET configuration consisting of methanofullerene [6,6]-phenyl-C61-butyric acid methyl ester (PCBM) as active semiconductor on top of an organic dielectric layer and calcium as the drain-source contacts. Lower apparent mobilities were observed for gold and aluminum contacts [149].

#### 2.4.3 Progress in Ambipolar OFETs

In addition to the development of  $p$ -channel and  $n$ -channel FETs, there are a few reports on ambipolar transistor, where both  $p$ - and  $n$ -type of transport can be achieved in a single device. The advantages of such device are: (i) possibility

of complementary circuit with low power consumption analogous to Complementary-Metal-Oxide-Semiconductor (CMOS) technology; (ii) possibility of having radiative recombination in a transistor by balancing the injection of both electrons and holes at the same place. Despite high purity with few acceptors ( $< 10^{13} \text{ cm}^{-3}$ ), the unipolar transport characteristics is typically observed in organic semiconductors. This can be attributed to different injection efficiencies for electrons and holes and to some extent can be related to the effective mass of the charge species. An approach using heterostructure FET was reported to obtain ambipolar transport in a single device with bottom-contact architecture [137,150]. The device structure consisted of 6T and  $\text{C}_{60}$  as the two active layers for *p*- and *n*-channel operations respectively. The active layers were sublimed on top of silicon oxide layer, drain and source contact pads. The two materials were selectively chosen owing to the fact that HOMO level of 6T is energetically lower for holes than the HOMO of  $\text{C}_{60}$  while the LUMO of  $\text{C}_{60}$  is energetically lowered for electrons. The drawback of this structure was the use of similar metal electrodes, one of which possess Schottky barrier with  $\text{C}_{60}$ . Recently two different drain and source were adopted according to the semiconductors pentacene and *N,N'*-ditridecylperylene-3,4,9,10-tetracarboxylic diimide (PTCDI- $\text{C}_{13}\text{H}_{27}$ ) to obtain balanced mobility [151]. An alternative approach was adopted by making a film of heterogeneous polymer blends consisting of interpenetrating networks and also by using narrow-bandgap organic semiconductors [152]. A blend of hole-transporting poly(methoxy dimethyloctyloxy)-phenylene vinylene (OC1C10-PPV) with electron-transporting PCBM was used for ambipolar conduction. The electron mobility in such blends ( $7 \times 10^{-4} \text{ cm}^2 \text{ V}^{-1} \text{ s}^{-1}$ ) was two orders of magnitude lower than the electron mobility of a pure film of PCBM, while the hole mobility was similar to that of single-component OC1C10-PPV ( $3 \times 10^{-5} \text{ cm}^2 \text{ V}^{-1} \text{ s}^{-1}$ ). Ambipolar transport was also found in OFET structure fabricated with a layer of PCBM [153]. Pentacene film together with calcium as source and drain were also used to extract ambipolar conduction incorporating hole mobility and electron mobility of  $4.5 \times 10^{-4} \text{ cm}^2 \text{ V}^{-1} \text{ s}^{-1}$  and  $2.7 \times 10^{-5} \text{ cm}^2 \text{ V}^{-1} \text{ s}^{-1}$

respectively [154]. A recent breakthrough on ambipolar transport in most of the common *p*-type semiconductors has received considerable attention towards this remarkable research field. According to this report, the origin of unipolar transport in such materials is the presence of hydroxyl group (OH) and they may act as trap centres [80] and Oxygen has high electron affinity, which replaces the hydrogen ion of OH with induced electrons, providing hole-only transport. However, the inclusion of hydroxyl-free insulator, for example divinyltetramethylsiloxane-bis(benzocyclobutene) (BCB), has offered ambipolar transport in almost all the well-known *p*-type conjugated polymers. A brief overview of different device configuration is tabulated in Table 2.1.

Table 2.1 Performance of Transistors with different device configurations

Device Type	Materials Used				Device Dimension		Device Parameters		Remarks	Ref
	DS	G	Ins	Sem	L	W/L	$\mu$	On/Off		
Staggered + Bottom gate	Au	Al	SiO <sub>2</sub>	P3HT	75	20	0.1	>10 <sup>6</sup>	HMDS treatment	[15]
Coplanar + Bottom gate	Au	Al	SiO <sub>2</sub>	Pentacene	20	2.5	1.5	10 <sup>8</sup>	OTS treatment	[142]
	Au	n <sup>+</sup> -Si	SiO <sub>2</sub>	P3HT	5	200	0.18	400	Dip coating	[114]
	Au	Au	PDMS	Rubrene	75	13	20	10 <sup>6</sup>	Elastomeric stamp	[155]
Staggered + Top Gate	Au	Au	TC101	P3HT	100	15	10 <sup>-4</sup>	10 <sup>3</sup>	-	[156]
Short Channel	Pt	-	SiO <sub>2</sub>	Pentacene	0.03	3.3	10 <sup>-2</sup>	10 <sup>2</sup>	Electron-beam Patterning	[157]
	PE-DOT/Au	PE-DOT/PSS	PMMA	F8T2	0.03	2667	0.006	-	Dwelled electrodes Top Gate + Top Contact	[158]
Bilayer Dielectric	Au	p <sup>+</sup> -Si	PMMA/Ta <sub>2</sub> O <sub>5</sub>	Pentacene	100	190	0.29	2.7 × 10 <sup>5</sup>	-	[159]

\* DS – Drain & Source; G – Gate; Ins – Insulator; Sem – Semiconductor;  $L$ – Channel length;  $W$  – Channel width;  $\mu$  – Field-effect mobility in  $\text{cm}^2\text{V}^{-1}\text{s}^{-1}$

## **Chapter 3**

### **Materials, Fabrication and Measurements**

#### **3.1 INTRODUCTION**

The choice of the materials and the fabrication methods are the vital aspects involved in fabricating the PFETs. Poly(3-hexylthiophene) (P3HT) and Poly(3-octylthiophene) (P3OT) were chosen as the active layer possessing high photoresponsivity and large field-effect mobility ever known among the *p*-type conjugated polymers. Several well-known insulators such as silicon dioxide (SiO<sub>2</sub>), polyvinyl alcohol (PVA) were employed as the gate dielectrics. The silicon wafers, poly(ethylenetheraphthalate) (PET), aluminum coated glass plates, and indium tin oxide (ITO)-coated glass plates were used as the substrates. A detailed description of the materials selection and the fabrication procedures are discussed in the following sections.

#### **3.2 MATERIALS**

This section deals with the brief introduction to the materials like P3HT, PVA and hexamethyldisilazane (HMDS), which were used in device fabrication. The knowledge about synthesis and the chemical and physical properties of these materials is essential to understand and then optimize the device performance.

##### **3.2.1 Poly(3-hexylthiophene) (P3HT)**

P3HT belongs to the group of alkyl-substituted thiophene compounds and usually is referred to as poly(3-alkylthiophene) (P3AT). Polythiophene is a leading candidate for optoelectronic application with sufficient thermal stability ( $T_g > 150$  °C). In the quest of solubility and processability, the first synthesis of P3AT was reported a couple of decades ago [160]. Following this invention, there was a considerable progress in synthesis of P3ATs. Typically there exist three well-known methods for synthesis of P3ATs, namely (i) electrochemical



polymerization, (ii) oxidative polymerization of 3-alkylthiophene by oxidants like ferric chloride ( $\text{FeCl}_3$ ) and (iii) polymerization by dedihalogenation of 2,5-dihalo-3-alkylthiophene [161]. Depending on the relative position of alkyl group attached in the two consecutive chains, the polymer chains form head-to-head (HH) or head-to-tail (HT) or tail-to-tail (TT) combinations, as shown in

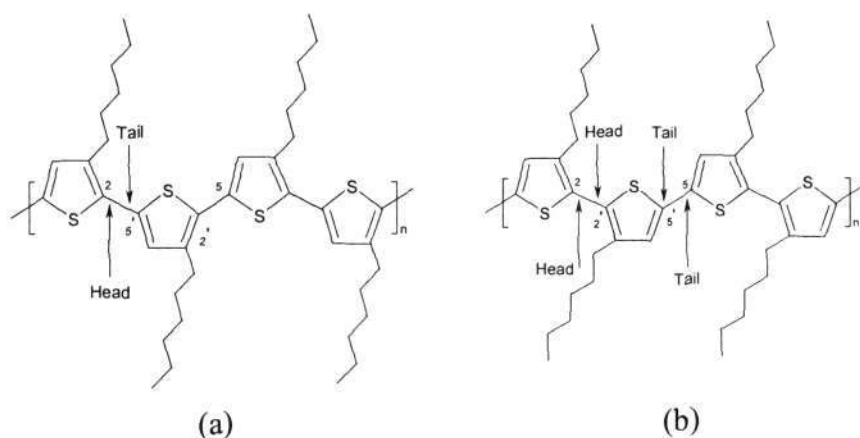


**Fig. 3.1** Schematic structure of P3HT with (a) head-to-tail coupling and (b) head-to-head and tail-to-tail couplings.

Fig. 3.1. For HH, the coupling between two consecutive monomer rings occurs through 2- and 2- positions and similarly HT and TT are through 2, 5' and 5, 5' positions respectively. The appearance of the triad leads to four possible isomerisms namely HT-HT, TT-HT, HT-HH and TT-HH. The combination of HT-HT can access a low energy planar conformation, leading to high conjugated polymers. On the other hand, appearance of unfavorable HH coupling causes a sterically driven twist of thiophene rings that result in a loss of conjugation, higher band gap with consequent destruction of high conductivity and the other desirable properties. According to the degree of orientation, P3HT is divided in two categories. One is called the *regiorandom*, where the HH and HT are randomly distributed and the other is known as *regioregular*, which contains either HH or HT. Most of the polymers are commercially available. In particular, P3HT was obtained from Sigma-Aldrich, USA. The organo zinc reagents formed by reacting Ricke Zinc with 2,5 dihalothiophenes is typically used to synthesize P3HT of this category [162].

These P3HTs offer more than 98.5% regioregularity as obtained in nuclear magnetic resonance (NMR) spectroscopy.

Self-organized supramolecular structures of P3HTs upon coating on the insulating surface was normally observed to provide a prominent signature for reasonable 2-dimensional charge transport in FET structure (Fig. 3.2). The preferable orientations of polymer chain along (100) plane due to the lamella layer structure and (010) plane due to  $\pi$ - $\pi$  interchain stacking were reported on the basis of X-ray diffraction (XRD) study of P3HT structure [163]. Recent exploration on the orientation effect of P3HT using synchrotron grazing-incidence XRD was also evident for reflections from (100), (200), (300) and (010) planes at the scattering angles ( $2\theta$ )  $5^\circ$ ,  $11^\circ$ ,  $16^\circ$  and  $22.5^\circ$  respectively

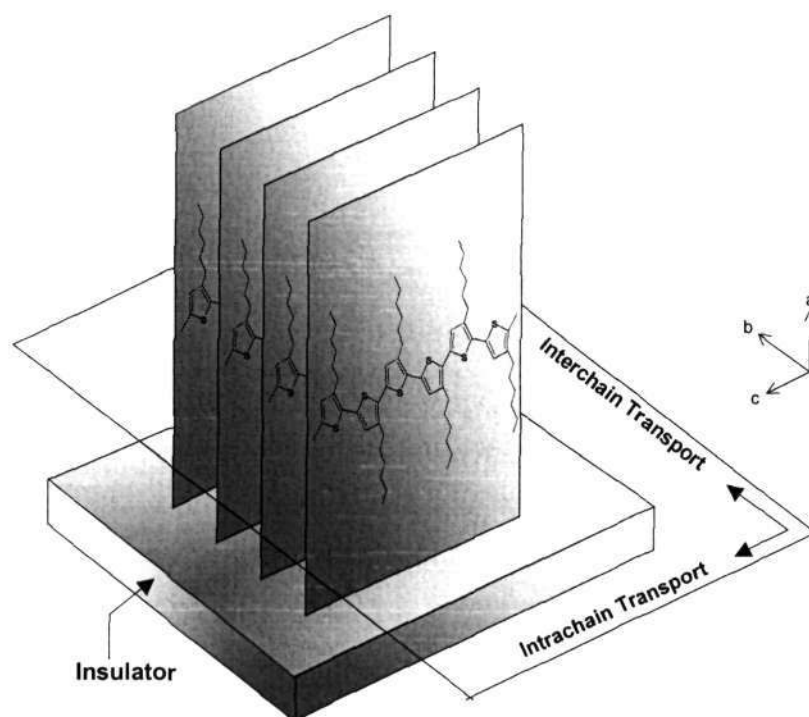


**Fig. 3.2** Schematic representation of self-assembled structural ordering in regioregular P3HT providing 2-dimensional charge transport.

[164]. The three-dimensional structural order can be represented by the axes  $a$ ,  $b$  and  $c$  along the lamella layer structure,  $\pi$ - $\pi$  interchain stacking and polythiophene chain with repetition distance of  $16.81 \text{ \AA}$  and crystallite size

(coherence length) of 1.75 nm ( $\sim 10$  unit cells) along  $a$ -axis [165]. However, the structural orientation of P3HT is very sensitive to degree of regioregularity and the way of deposition techniques. In samples with high regioregularity ( $> 91\%$ ) and low molecular weight, the preferential orientation of the ordered domains is along with  $a$ -axis normal to the substrate and the  $b$ -axis in the plane of the substrate [118]. On the other hand, in samples with low regioregularity (81%) and high molecular weight, the crystallites are preferentially oriented with  $a$ -axis and  $b$ -axis being in the plane and normal to the plane of the substrate, respectively [165]. The direct correlation between the mobility and the  $\pi$ - $\pi$  interchain interaction in P3HT was clearly reflected the degree of regioregularity [118]. The mobility of P3HT-based FET was observed to increase with degree of regioregularity. This suggests that the alignment of  $b$ -axis along the substrate enhances the mobility. The influence of interchain interaction on mobility was perceived by comparing two types of FET devices consisting of spin-cast and drop-cast films of 81% regioregular P3HT. In case of drop-cast film,  $b$ -axis was observed to be in parallel to the plane of the substrate. The mobility obtained was quite significantly higher than that obtained from spun-cast ones. The slower deposition rate was proposed as the possible reason of obtaining higher mobility for the dip casting. The correlation between the field-effect mobility and the structural order can be established on the basis of above observations.

The strong interchain coupling was also manifested in charge modulation spectroscopy (CMS) of MIS diode structure consisting of regioregular P3HT as semiconductor [118]. The sub-gap transitions in CMS spectra revealed the existence of polaronic transport. In addition, the existence of forbidden C3 transition ( $\approx 1.75$  eV), which is approximately the sum of C1 ( $\approx 0.35$  eV) and C2 ( $\approx 1.35$  eV) transitions, was attributed to the interchain interaction. This aspect was also mentioned in chapter 2 [Section 2.2.8]. In their study the charge-transfer like transitions due to the configuration interactions was also observed in infrared region ( $< 0.3$  eV).

### 3.2.2 Polyvinyl alcohol (PVA)

Polyvinyl alcohol (PVA) is a water-soluble synthetic polymer and commercially available as white granular solid and powdered forms. PVA is typically used as a thickener, stabilizer and binder in industrial applications along with other commercial applications such as cosmetics, paper cloth, films, cements and mortars etc. This material can be employed in making sensors, drug delivery biocompatible magnetic film etc. due to its unique and excellent film forming properties [166,167]. PVA is synthesized by hydrolysis of a polyvinyl ester such as polyvinyl acetate using transesterification method (Fig.

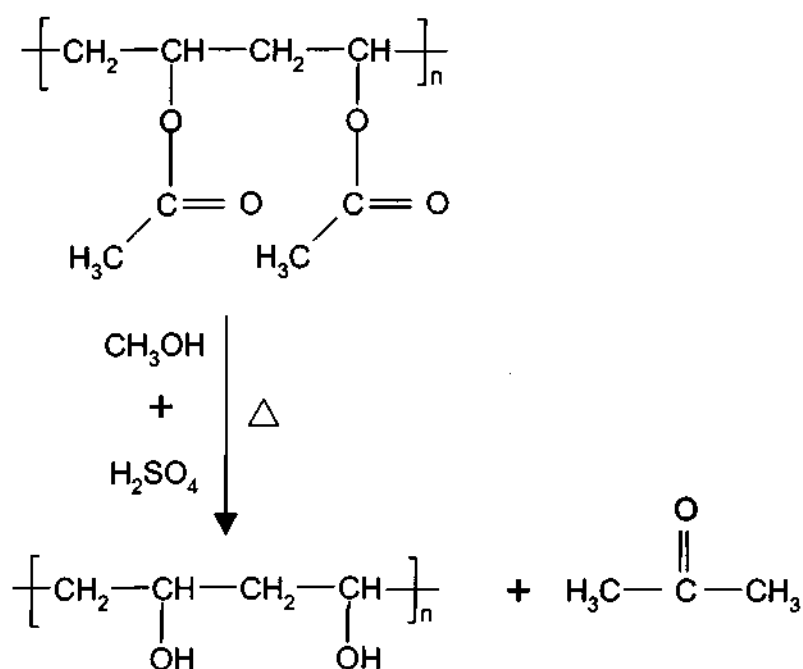


Fig. 3.3 Synthesis of polyvinyl alcohol (PVA) using transesterification method.

3.3). The percentage of the polyvinyl acetate, which is hydrolyzed to alcohol groups, is known as *percentage hydrolysis*. The desirable properties of fully hydrolyzed PVA, i.e., with hydrolysis of around 98% or more, are decreased water sensitivity and increased tensile strength. On the other hand, partially hydrolyzed PVA (about 88% hydrolyzed) shows increased water sensitivity and can be used as a good dispersing agent. With increasing molecular weight

ranging from  $10^4$  to  $10^5$ , viscosity and tensile strength increase while water sensitivity decreases.

PVA is a good dielectric material and it can be processed easily to achieve flexible, transparent thin film with less surface roughness. These properties were exploited in organic electronics to use it as an insulating material for FET fabrication [81]. The dielectric constant of PVA at room temperature is quite high ( $\epsilon_r \approx 8-10$ ) as compared to silicon dioxide or other conventional polymer insulators and it varies with temperature as well as frequency [168,169]. In particular, PVA was used as an insulator due to two major advantages; (i) PVA is completely transparent in the visible range, which is a crucial property to study the light activated feature of the transistor and (ii) the refractive index ( $\eta$ ) of PVA is 1.51 [170], the value is closely resembled to that of glass ( $\eta = 1.5$ ). Owing to the combination of several additional features, the unique dielectric material PVA is widely employed. It is essential to mention that the partially hydrolyzed PVA, being sensitive to moisture, can be a source of charge trapping centres. This feature was exploited recently to obtain electrically operated memory effect in OFET [171].

### **3.2.3 Hexamethyldisilazane (HMDS)**

In solution-processed deposition technique, the interface between the polymer semiconductor and insulator is a crucial factor for deciding the field-effect mobility. Hexamethyldisilazane (HMDS) is a *silane* (silicon-based) chemical, which typically acts as a bridge between the inorganic substrate and the organic materials increasing the van der Waals interaction between the two surfaces. HMDS (molecular weight = 161.4) is synthesized from trimethylchlorosilane and ammonia using *amination* process, as shown in Fig. 3.4(a). The main purpose of using HMDS layer is to convert the insulator surface from hydrophilic to hydrophobic. The common problem of oxide-coated silicon substrate (Si/SiO<sub>2</sub>) is the appearance of hydroxyl group in the form of silanol (Si-OH) that makes the surface hydrophilic. The treatment SiO<sub>2</sub> with HMDS replaces the hydroxyl groups at the SiO<sub>2</sub> surface with methyl groups,

forming  $[(\text{CH}_3)_3\text{Si-Si}]$  compound on the surface and ammonia as byproduct, as displayed in Fig. 3.4(b). Ammonia is conducted by heating under reflux. The apolar nature of the modified surface containing methyl groups apparently

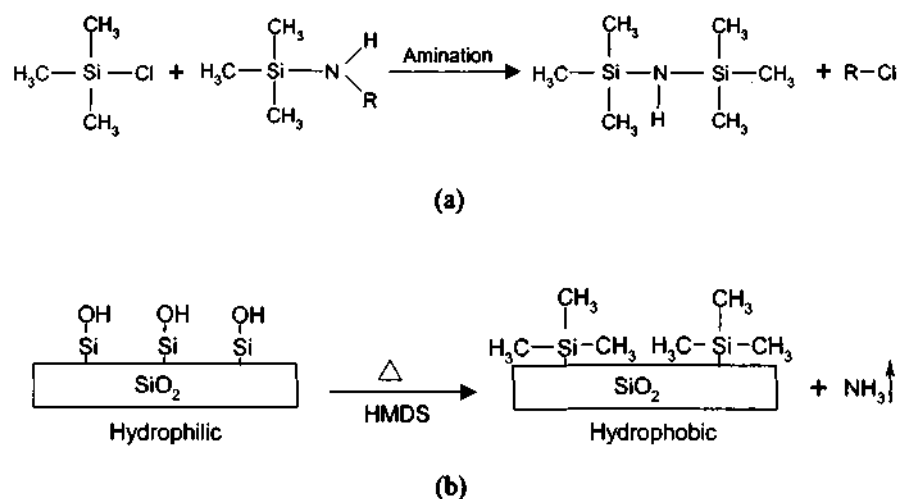


Fig. 3.4 (a) Synthesis of hexamethyldisilazane (HMDS) using amination method. (b) Surface modification of  $\text{SiO}_2$  using HMDS treatment.

attracts the hexyl side chains of P3HT, which in turn leads to the assembly of lamella structure with  $b$ -axis oriented parallel to the substrate. HMDS treatment on insulating surface can be performed either by projecting HMDS vapor for 2 minutes at  $120^\circ\text{C}$  [121,172] or by spin-coating HMDS, followed by annealing at  $120^\circ\text{C}$  for 1 hour [173].

### 3.3 FABRICATION METHOD

Polymer field-effect transistors in top-contact configuration were fabricated using the standard protocol, as follows: (i) cleaning of the substrates (plain glass, ITO-coated glass plate, commercially available  $\text{Si}/\text{SiO}_2$ , PET), (ii) deposition of gate electrode (Al) electrode (only for glass and PET), (iii) preparation of homogenous PVA solution, (iv) spin-casting of PVA films on top of gate electrode's surface (exception in  $\text{Si}/\text{SiO}_2$  substrate), (v) surface treatment using HMDS, (vi) purification of P3HT using *re-precipitation* method, (vii) spin-casting of highly purified P3HT films on top of the gate dielectric, (viii)

post-coating thermal treatment and finally (ix) controlled and uniform deposition of drain-source (Au) electrodes. Glass plates were pre-cleaned with isopropyl alcohol, acetone, ethanolamine, hexane, distilled water and finally in acetone to remove any traces of water and the films were kept in a heat bath to dry out all the solvents. ITO coated glass plates were also cleaned using standard RCA cleaning, where the substrates were dipped into a mixture of ammonium hydroxide, hydrogen peroxide and distilled water (1: 1: 5) and heated around 80 °C for 15 minutes. Finally the substrates were cleaned in distilled water and acetone and then dried. Similar treatment was also applied to Si/SiO<sub>2</sub> substrate.

Aluminum was coated on top of glass (also for PET) substrate using

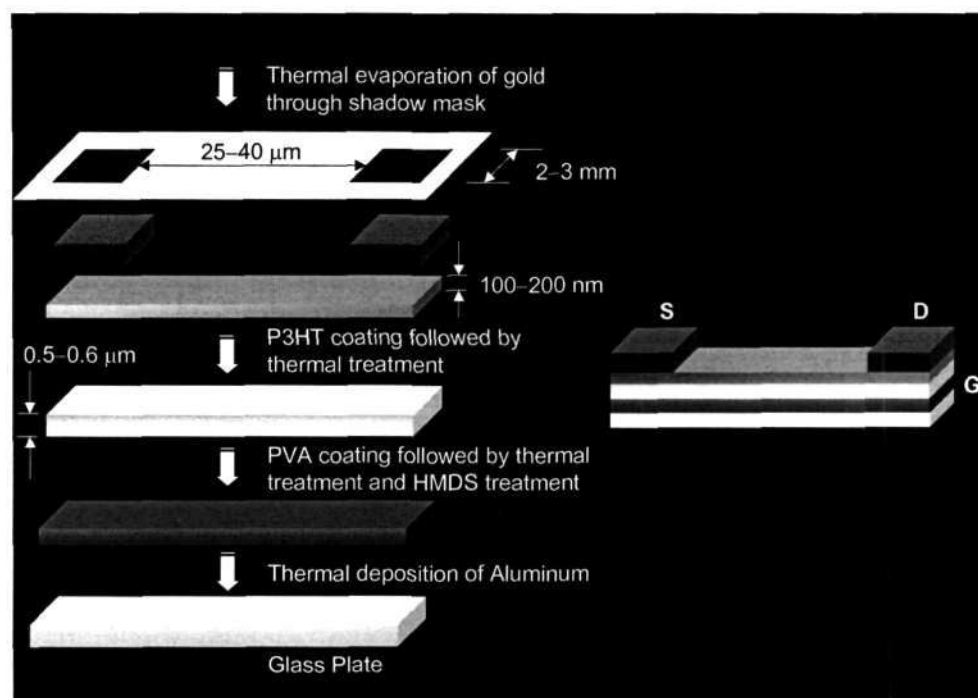


**Fig. 3.5** Fabrication method of polymer field-effect transistor (PFET).

thermal evaporation technique. PVA was dissolved in distilled water with gentle heat and then filtered. The spun-cast film of PVA was obtained using with spinning speed of about 1500 revolutions per minute (rpm) to maintain the thickness of 0.5–0.6 μm (exception in Si/SiO<sub>2</sub> substrate). The thin film was thermally treated at 60 °C for 6–7 hours or sometimes even more. Prior to

P3HT coating, the insulator was undergone by surface treatment with HMDS vapor followed by annealing at 70 °C for 2–3 hours to achieve hydrophobic surface. P3HT was purified using re-precipitation method. In this method P3HT was first dissolved in toluene and then acetone was added to the solution. As acetone is non-solvent for P3HT, a dark red precipitation of P3HT appeared, whereas the other organic contamination was dissolved in acetone. The acetone was removed from the mixture and the precipitated P3HT was dried. This process was repeated for more than three times to ensure the solvents were dried completely. The purified P3HT was dissolved in chloroform and the solutions were filtered by 0.2  $\mu\text{m}$  pore size filter papers. A thin layer of P3HT was spin coated (1500 rpm for 1 minute) from chloroform solution (5–10 mg/ml) in nitrogen atmosphere ( $< 1$  ppm  $\text{O}_2$ ,  $< 1$  ppm  $\text{H}_2\text{O}$ ) to obtain the thickness of 100–200 nm. After a thermal treatment process at 70 °C for more than 12 hours in vacuum, gold was thermally evaporated (under a vacuum level  $\sim 10^{-6}$  mbar) through a shadow mask to form drain and source electrodes with separation of 25–40  $\mu\text{m}$  ( $L$ ) and width ( $W$ ) of 2–3 mm ( $W/L \sim 100$ ). The whole process of device fabrication is displayed in Fig. 3.5. Finally electrical contacts were made to the three electrodes and the device was transferred to a vacuum chamber ( $10^{-3}$  mbar) for electrical and optoelectronic measurements.

### 3.4 MEASUREMENTS

All the devices were always kept in inert and/or vacuum conditions prior to experimentation. Firstly, the output and transfer characteristics of P3HT-based FET were carried out and subsequently various optoelectronic measurements on the same device were performed. We repeated the measurements several times to ensure the reproducibility of the results within the experimental limits.

#### 3.4.1 Absorption Coefficient Measurement

In case of polymer electronics, absorption spectrum that measures the absorption coefficient  $\alpha$  as a function of energy or wavelength ( $\lambda$ ), carries the primary information about the energy levels of the polymer and provides



various informations about the sub-gap states arising due to the impurities or defects. Absorption coefficient  $\alpha(\lambda)$  is essentially one of the important order parameters for detecting optoelectronic properties. Here  $\alpha(\lambda)$  of P3HT film was obtained using Hitachi U-3400 spectrophotometer and Perkin Elmer spectrophotometer. The absorption coefficient is usually determined from Beer-Lambert's law i.e.  $P = P_0 \exp(-\alpha d)$ , where  $d$  is the thickness of the film,  $P_0$  and  $P$  are the incident beam intensity and transmitted beam intensity respectively. The relationship between  $\alpha(\lambda)$  and the thickness of the film can thus be written in the form of

$$\alpha(\lambda)d = 2.303 \log(P_0/P) \quad (3.1)$$

With the knowledge of known values of thickness (we obtained thickness value from surface profilometry measurement),  $P_0$  and  $P$ , one can estimate  $\alpha(\lambda)$ . A typical value of  $\alpha \approx 2 \times 10^5 \text{ cm}^{-1}$  was observed at  $\lambda \approx 525 \text{ nm}$ . The vibronic features were observed around 2.36 and 2.24 eV (with a shoulder around 2.1 eV) along with the onset of the bandgap around 1.9 eV.

#### 3.4.2 Transistor Output Characteristics and Transfer Characteristics

Two identical sourcemeters SM1 and SM2 (Keithley 2400) along with a high impedance Electrometer (Keithley 6512) were used for performing the

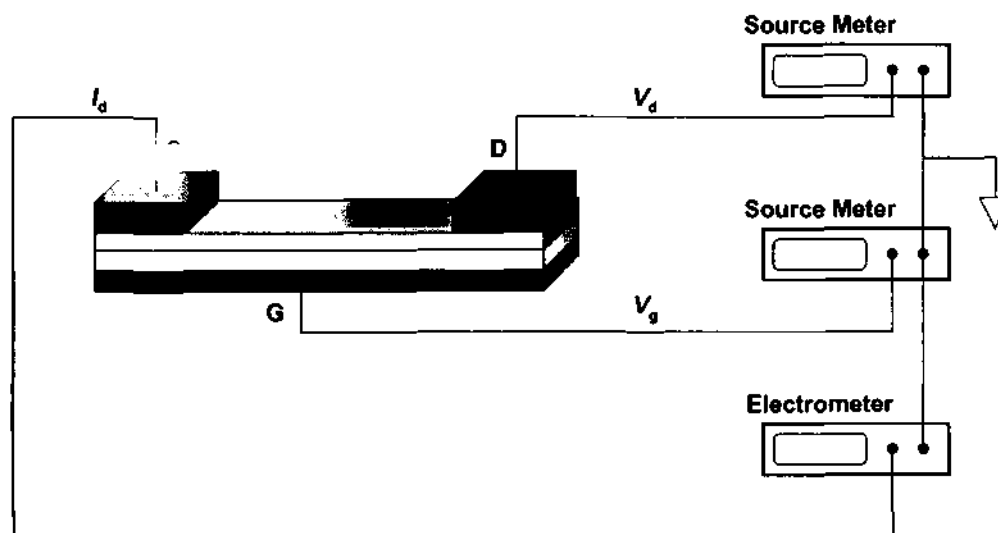


Fig. 3.6 Schematic diagram for transistor characteristic measurement.

transfer and output characteristics of PFETs. All the instruments were interfaced parallelly with the computer by means of General purpose interfaced bus (GPIB). The data acquisition was done using computer-controlled Q-BASIC and LabVIEW (version 6.1) programming. The schematic diagram of the set-up is shown in Fig. 3.6. The scan was done with sufficient interval between two successive data points depending on the response of PFET. In case of output characteristics, drain voltage ( $V_d$ ) was varied through SM1 for different sets of voltage (gate voltage  $V_g$ ) in the SM2. For measuring transfer characteristics  $V_g$  was changed through SM2 by keeping SM1 fixed. Prior to measure the transistor characteristics, we ensured that in all the cases the magnitude of leakage current as low as 100 pA was maintained to obtain the typical features. The leakage current can be traced by two techniques: (i) comparing  $I_d$  in SM1 and EM, which should ideally be identical; (ii) measuring  $I_d$  for different  $V_g$  with source-drain shorted ( $V_d = 0$  V), which ideally should be constant with negligibly small value (2–3 orders less than the saturated  $I_d$ ). Current-voltage (I-V) characteristics of a PVA film in a sandwiched configuration with two metallic Al-electrodes were also observed in this set-up.

#### 3.4.3 Capacitance-Voltage Measurements

Thin films of PVA sandwiched between two Al-electrodes were measured using this technique to study the dielectric property of PVA. In this method, a constant dc bias ( $V_{dc}$ ) coupled with a small ac signal ( $V_{ac}$ ) of frequency  $f$  was applied to the device and changes in impedance were detected. The more direct value of capacitance was obtained for different frequencies. The capacitance of PVA film was measured as a function of  $V_{dc}$  for different frequencies using a Keithley C-V meter. The measurements were carried out assuming that the contacts between the electrodes and the films were ohmic. In case of FET, the capacitance of the insulator should ideally be independent of voltage, frequency and temperature for stable performance.

#### 3.4.4 Transient Photocurrent Measurements

Transient photocurrent measurement is a useful technique in the time domain to study the dynamics of photoinduced charge carriers. In particular, the measurements were carried out in both dc and ac modes. In dc mode, the experimental set-up is similar to that used for transistor characteristics. Various light sources were used ranging from blue to red colors (blue diode laser of  $\lambda =$

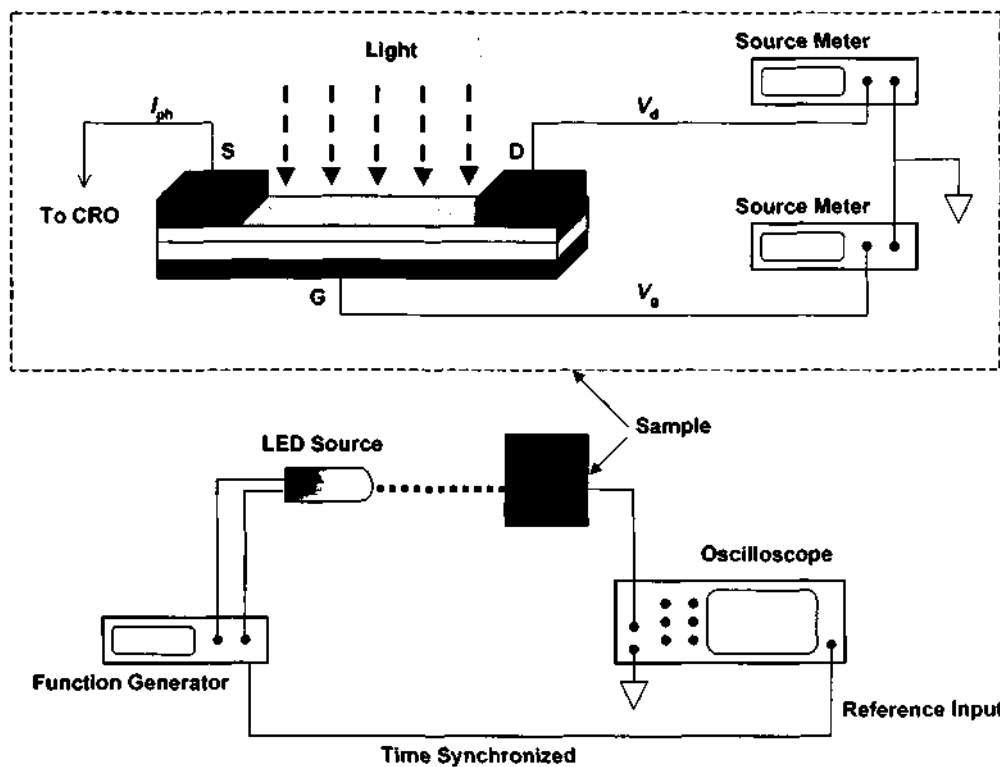


Fig. 3.7 Schematic diagram for transient measurement using oscilloscope.

473 nm, nanosecond-pulsed green laser  $\lambda = 532$  nm, red He-Ne laser of  $\lambda = 632.8$  nm, each of power 5 mW). All the measurements were carried out by recording the current in EM as a function of time to study the prolonged decay (for several hours). On the other hand, in an ac mode, the electrometer and the light source were replaced with 1 GHz sampling rate, 500 MHz storage oscilloscope (HP) and a light emitting diode driven by a function generator (Tektronix AFG320) respectively. The oscilloscope and the function generator were synchronized with each other (Fig. 3.7). In this method, the initial response of the photoinduced current and relaxation were studied. Single shot pulse measurements with different pulse width were also carried out in FET

structure for different  $V_g$ . This technique is a useful tool to estimate the charge carrier generated within a short time and can be used to find out the quantum yield of the device under test.

### 3.4.5 Intensity Modulated Photocurrent Spectrum (IMPS)

Intensity modulated photocurrent spectrum (IMPS) is a powerful tool to determine the photoresponse, field distribution, location of photoinduced charge generation etc. This measurement is carried out in frequency domain. In this case a lock-in amplifier (SRS 830) was used instead of electrometer to detect

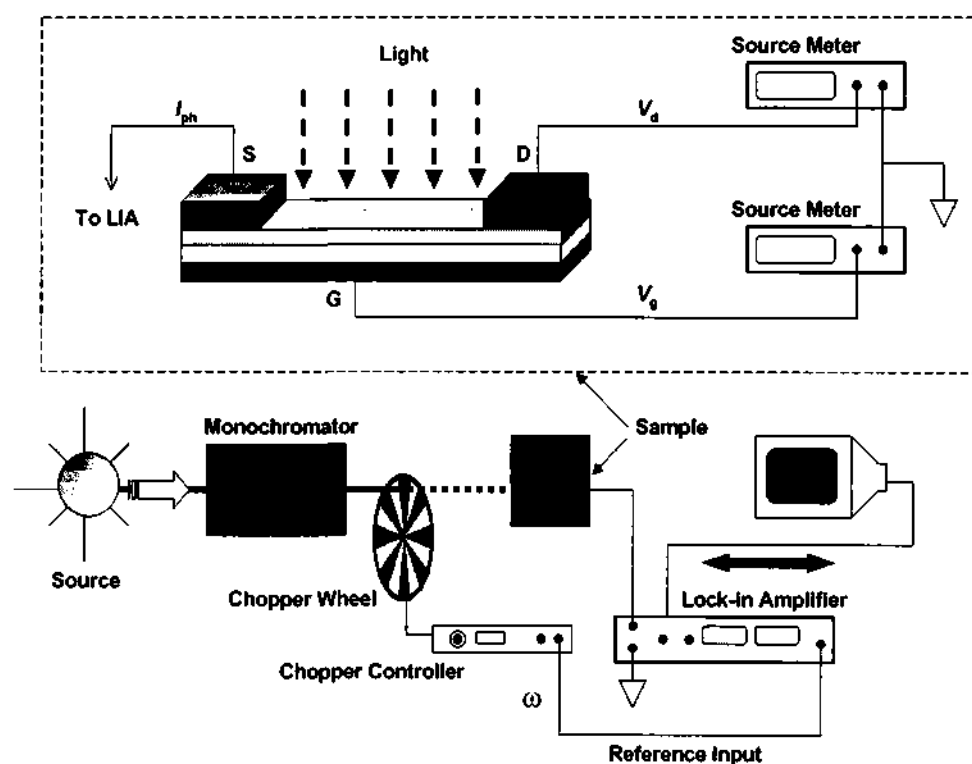


Fig. 3.8 Schematic diagram of the set-up for intensity modulated photocurrent spectroscopy (IMPS) measurement.

weaker signals, coupled with high signal to noise ratio. IMPS involves chopping of illuminated light and measuring the photocurrent using lock-in amplifier that is synchronized with the chopping frequency. The integration time constant of the lock-in amplifier and so the speed of data acquisition were varied according

to the chopping frequency. Tungsten lamp, coupled with a monochromator (Acton Spectrapro150), was used to provide a wide range of spectral window for this typical photocurrent measurement. The set-up is schematically displayed in Fig. 3.8. The photocurrent spectral response can be expressed as

$$I_{\text{ph}}(\lambda) = KP(\lambda)\alpha(\lambda)\eta(\lambda) \quad (3.2)$$

where  $K$  is a constant and  $\eta(\lambda)$  is efficiency of photocurrent generation. The experimental curve obtained was normalized, whenever required.

#### **3.4.6 Optical Microscopy and Electron Microscopy**

The optical microscopy on PFET structure was carried out to study the morphology of the film and to measure the channel length. An optical microscope (HUND), coupled with a detector showing position of the beam, was used. The microscopy measurement was also conducted under an inverted microscope (Nicon). The thickness of the film was also measured using this microscope along with custom-built light detection set-up. Scanning electron microscopy (SEM) was carried in some of the samples to observe the morphology and alignment of the electrodes with better resolution.

#### **3.4.7 X-ray Diffraction (XRD) and Grazing Incidence X-ray Diffraction (GIXRD) Measurements**

The ordering and self-assembly of pristine P3HT film atop HMDS-treated glass plate was verified using conventional X-ray diffraction (XRD) and grazing incidence X-ray diffraction (GIXRD) techniques. No significant ordering was observed in XRD technique, as expected. But in GIXRD measurement (in plane), a peak at  $2\theta \approx 5^\circ$  ( $\theta$  is the angle of incidence), representing the (100) plane, was observed. The GIXRD measurement was conducted in CCMR, Cornell University, USA.

## **Chapter 4**

# **Slow Relaxation of Photoinduced Drain Current in PFET**

### **4.1 INTRODUCTION**

The normal tendency of non-equilibrium system is to approach towards the equilibrium state. The rate of the dynamical movement from non-equilibrium state to equilibrium state determines the slowness of the system. There are several examples of such decay process from the excited state to the ground state involving system-specific relaxation time and dynamics. For example, the radioactive element, which decays spontaneously following single exponential behavior with respect to time, takes several years to be stable. But the decay processes involved in phosphorescence, glassy materials, or even in leaky capacitor are different in nature and also in different time scale. The nature of the decay process is strongly correlated to the system and can be used to extract material characteristics.

In this context, photosensitive conjugated polymers such as poly(phenylenevinylene), poly(alkylthiophenes) etc. also show slow decay of photoinduced current in the time range of several hours. The relaxation process after photoexcitation can provide valuable insight about the redistribution of the charge carriers and the field and many other dynamical aspects related to drift-diffusion process. The decay characteristics are typically interpreted in terms of stretched exponential decay law (SEDL). But this decay law cannot be applicable since they yield fitting parameters, which do not have physical basis. This chapter is mainly focused on the relaxation of photoinduced drain current involved in polymer field-effect transistors. The failure of SEDL to provide the sufficient explanation of the system-specific features is discussed here in detail. In addition, more appropriate model describing the observed trends is

demonstrated to acquire microscopic view of charge dynamics and the redistribution of the charge carriers in deciding the decay process.

#### 4.2 DARK CHARACTERISTICS OF POLYMER FIELD-EFFECT TRANSISTORS

The polymer transistors were primarily tested in vacuum ( $10^{-3}$  mbar) under dark condition. The device parameters such as field-effect mobility, on/off ratio etc. are essential factors not only to speculate the nature of the interface between the insulator and semiconductor but also to understand the photophysical feature. In particular, several types of P3HT based PFET were fabricated depending on the different combination of the insulating materials and the substrates.

##### 4.2.1 Output and Transfer Characteristics of Polymer Field-Effect Transistors

Four different categories of transistors, according to various combinations of the insulator and substrate materials, were fabricated and tested in similar

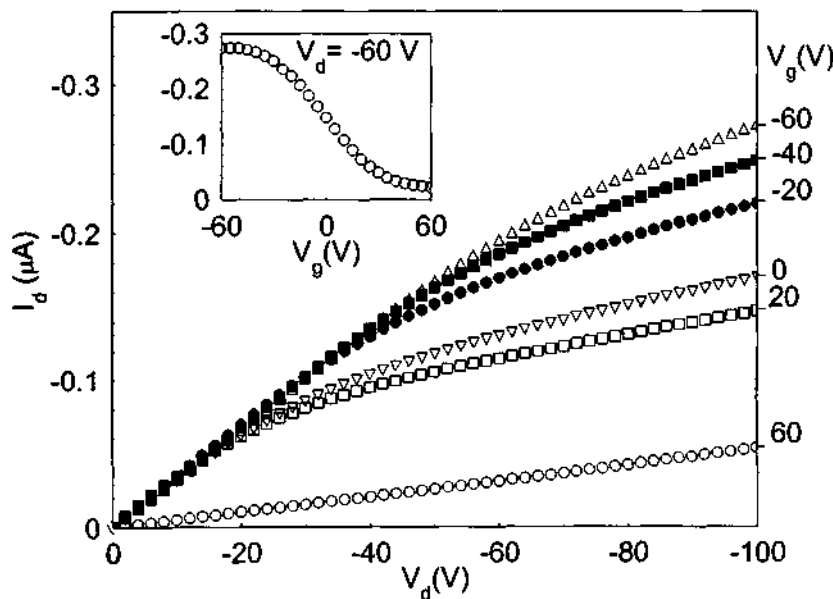


Fig. 4.1 Transistor output characteristics of device type I with  $L = 25 \mu\text{m}$ ,  $W = 2000 \mu\text{m}$ . Inset shows the transfer characteristic of the device at  $V_d = -60 \text{ V}$ .

conditions. P3HT and gold were used as the common semiconducting material

and the drain-source electrodes respectively for all the FETs. The devices are

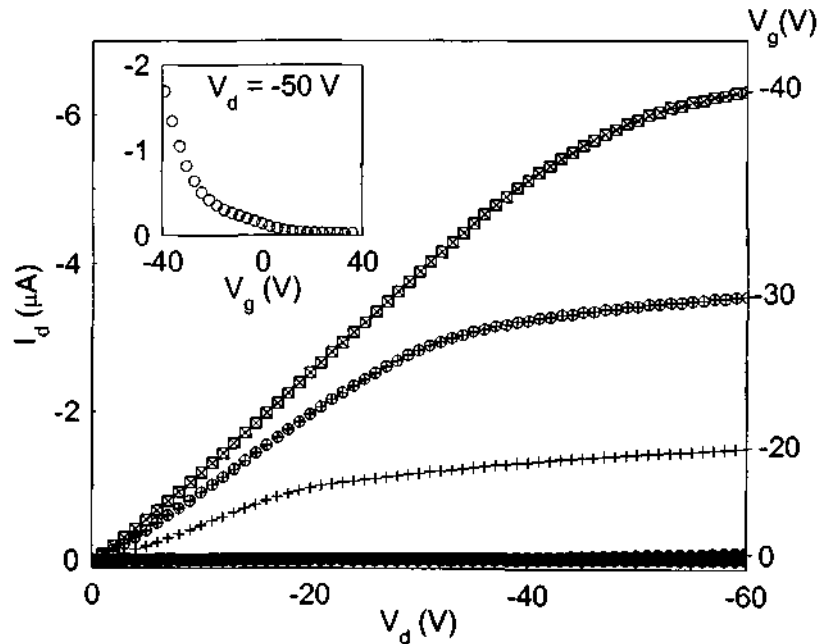


Fig. 4.2 Transistor output characteristics of device type II with  $L = 30 \mu\text{m}$ ,  $W = 3000 \mu\text{m}$ . Inset shows the transfer characteristic of the device at  $V_d = -50$  V.

identified as type I, II, III and IV. In type I, PVA was used as insulator and Al as metal gate electrode atop the glass plate. Type II devices with same dielectric medium were fabricated on transparent and flexible PET substrate. The device structures, consisting of  $\text{SiO}_2$  as insulator, were categorized in type III. The devices were fabricated on top of commercially available Si/SiO<sub>2</sub> wafer and heavily *p*-doped Si was used as gate electrode. In type IV, the devices were fabricated on top of the transparent ITO-coated glass substrate. PVA was used as the dielectric medium atop ITO as gate electrode.

The output characteristics and transfer characteristics of the devices of different kinds were primarily tested in vacuum as the primary test to extract the device parameters. The output and transfer characteristics of the best devices belonging to different types are displayed in Fig. 4.1–4.4 and the insets, respectively. Typical *p*-channel unipolar (hole-only) feature was observed in all the FET structures, operating under accumulation mode. The figure of merit of the FETs of different types is tabulated in Table 4.1. The analysis shows that



FET based on P3HT/SiO<sub>2</sub> is superior to the other devices in terms of mobility

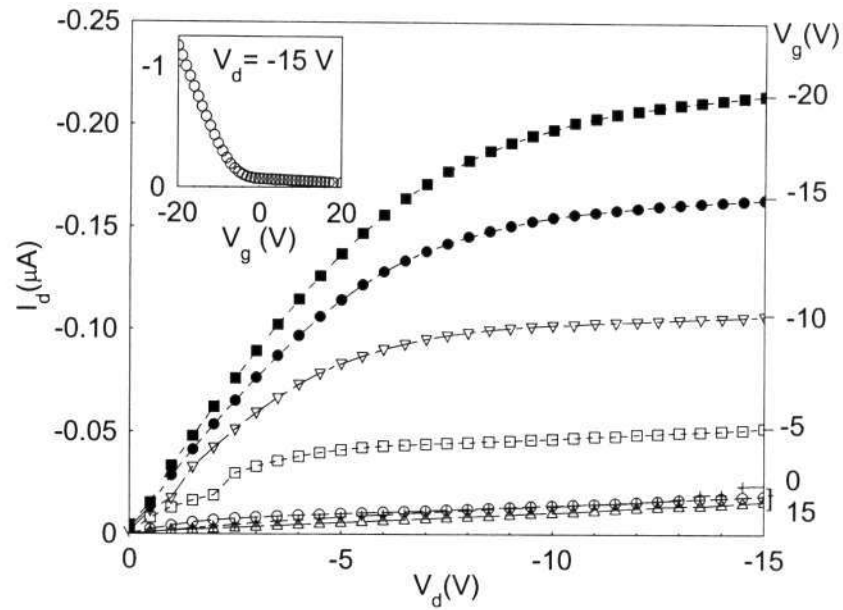


**Fig. 4.3** Transistor output characteristics of device type III with  $L = 30 \mu\text{m}$ ,  $W = 1640 \mu\text{m}$ . Inset shows the transfer characteristic of the device at  $V_d = -15 \text{ V}$ .

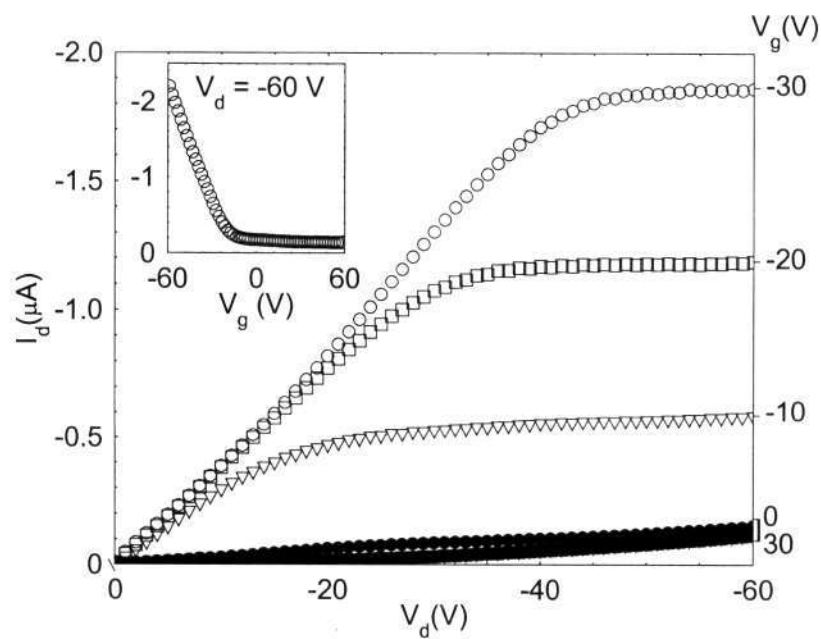


**Fig. 4.4** Transistor output characteristics of device type IV with  $L = 30 \mu\text{m}$ ,  $W = 3000 \mu\text{m}$ . Inset shows the transfer characteristic of the device at  $V_d = -60 \text{ V}$ .

and on/off ratio. The lower mobility of the device, containing P3HT/PVA

interface, can be attributed to the imperfections in the soft dielectric media and the presence of traps at the insulator-semiconductor interface. The trap-assisted feature was manifested as the hysteresis appearing in the transfer characteristics. The lower on/off ratio of  $I_d$  primarily arises from the high off current contributed by the bulk. However, FETs based on PVA are particularly suitable to demonstrate the photoinduced effects, which depend on the initial low-dark  $I_d$ . A wide choice of substrate and gate electrode is possible when the dielectric layer is polymers like PVA. Added advantages are the dielectric film along with its mechanically flexible and optically transparent features.

**Table 4.1 Performance of transistors with different combination of materials**

Device	Substrate	Gate	Insulator	$\mu$ ( $\text{cm}^2\text{V}^{-1}\text{s}^{-1}$ )	Remark
Type I	Glass	Al	PVA	$10^{-3}-10^{-4}$	HMDS treatment
Type II	PET	Al	PVA	$2 \times 10^{-3}$	Flexible FET
Type III	Si/SiO <sub>2</sub>	P <sup>+</sup> Si	SiO <sub>2</sub>	$3 \times 10^{-2}$	Highest mobility
Type IV	ITO coated Glass	ITO	PVA	$6 \times 10^{-3}$	Transparent gate

### 4.3 PHOTOINDUCED MODULATION OF TRANSISTOR CHARACTERISTICS

Upon photoexcitation, the transistor characteristics is severely altered in terms of the charge and field distribution, which renders substantial increase in drain-source current. The photoinduced excess charge carriers relax very slowly upon termination of light source. In addition, this device geometry serves as a model system to study the photophysics of the polymer semiconductors with controlled charge distribution in the background.

#### 4.3.1 Photoresponse of Polymer Field-Effect Transistors at Low Temperature

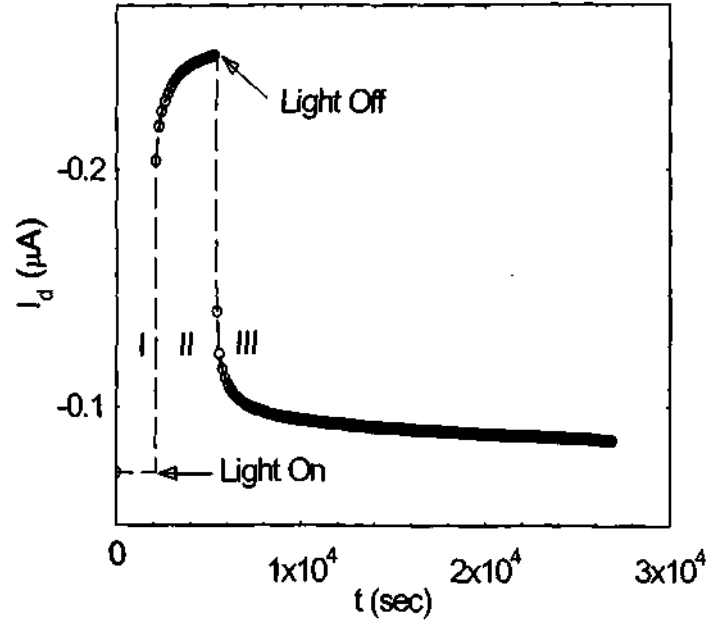


Fig. 4.5 Photoresponse of PFET structure at temperature 150 K,  $V_g = -20$  V and  $V_d = -80$  V. Region I, II and III represent the dark, light and relaxation components respectively.

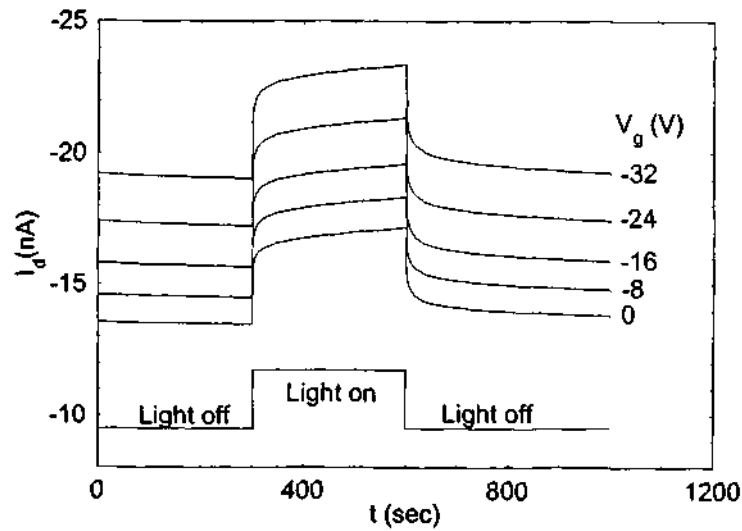


Fig. 4.6 Photoresponse of PFET structure as a function of  $V_g$  upon photoexcitation ( $\lambda = 532$  nm,  $1 \text{ mW/cm}^2$ ) from the bottom (through Al gate) at temperature 100 K,  $V_d = -40$  V.

Significant increase in  $I_d$  upon photoexcitation followed by slow relaxation after the terminating the light source was observed in PFET. Extremely

sluggish relaxation of photoinduced charge carriers (PCC) was more evident at low temperature. The photoresponse of FET is illustrated in Fig. 4.5, showing three different regions. Region I represents the initial dark  $I_d$ . Upon photoexcitation, a huge change is displayed in region II. In this regime, current is time-dependent as well as intensity-dependent. Immediately upon switching off the light, a rapid decay in the early stages followed by a slow decay

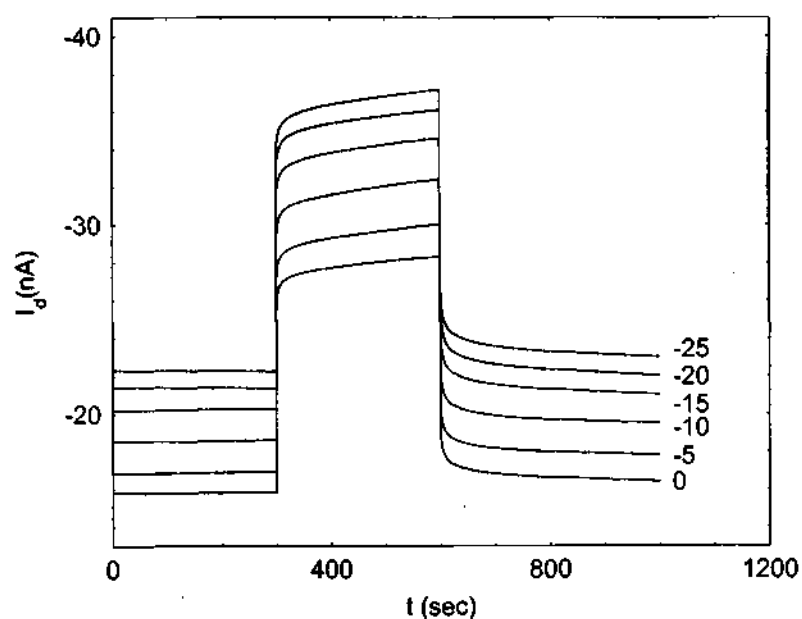


Fig. 4.7 Photoresponse of PFET structure as a function of gate voltage upon photoexcitation ( $\lambda = 532$  nm,  $1$  mW/cm<sup>2</sup>) from the top (through P3HT) at temperature  $100$  K,  $V_d = -40$  V.

component was observed at  $100$  K (region III in Fig. 4.5). The slow component was observed to continue for several hours showing typical persistence effect. The photoresponse of the PFET as a function of  $V_g$  for light incident from top (through P3HT) and bottom (through PVA) are shown in Fig. 4.6 and 4.7, respectively. Except the magnitude, no significant change was noticed between the two responses.

#### 4.3.2 Slow Relaxation of Photoinduced Conductance in PFET

The relaxation of PCC, after terminating light source, in the conventional semiconducting polymer films with surface configuration is typically very slow

[50,174]. The nonequilibrium conductance following photoexcitation in these systems was interpreted in terms of a dispersive diffusion mechanism restricting recombination. The decay mechanisms are typically fitted to a stretched exponential (Kohlrausch's law). The time-dependent current decay conductivity can be written as

$$I = I(0) \exp\left[-\left(\frac{t}{\tau}\right)^\gamma\right] \quad (4.1)$$

where  $\tau$  is the relaxation lifetime and the exponent  $\gamma$  ( $0 < \gamma < 1$ ) is indicative of the degree of disorder and associated with a distribution of activation energies. It is to be noted that  $\gamma = 1$  corresponds to conventional Debye relaxation, which is characterized by a single relevant relaxation time  $\tau$ .

The stretched exponential decay law (SEDL) is apparently a general characteristic of glassy materials and has been observed in a wide variety of complex disordered systems. Several mechanisms leading to stretched exponential behavior have been proposed including time-dependent barriers to recombination [175], hierarchically constrained dynamics [176], percolation [177], time-dependent diffusion processes [178] and recently hopping transport [179]. The physical processes involved in generating the SEDL can be classified in two main categories. The first one postulates a statistical distribution of relaxation lifetimes across many uncorrelated degrees of freedom, leading to parallel relaxation process. Then, with the assumption of additive contribution to the relaxation quantity (here it is current  $I$ ) can be expressed as

$$I(t) = \int_0^\infty \omega(\tau) \exp(-t/\tau) d\tau \quad (4.2)$$

Any reasonable  $I(t)$  can thus be explained by a suitable choice of *weight distribution*  $\omega(\tau)$ . However, this approach is microscopically arbitrary incorporating no specific distribution of lifetimes to account for stretched exponential behavior. The method was completely ruled out for practical purposes [176].

The other model premises a serial relaxation to equilibrium via a hierarchy of dynamical constraints. The model is based on three requirements: (1) the theory must be based on *dynamics* rather than mere statistics; (2) the theory must involve *constraints*; (3) the theory should involve a *hierarchy* of degrees of freedom, from fast to slow. This model thus predicts that the relaxation processes are correlated to each other describing a time dependent relaxation rate and the time evolution of  $I(t)$  is governed by the rate equation

$$\frac{dI(t)}{dt} = -k(t)I(t) \quad (4.3)$$

The stretched exponential decay must be then related to the functional form of decay rate  $k(t)$ . A link between the SEDL and the dispersive transport was

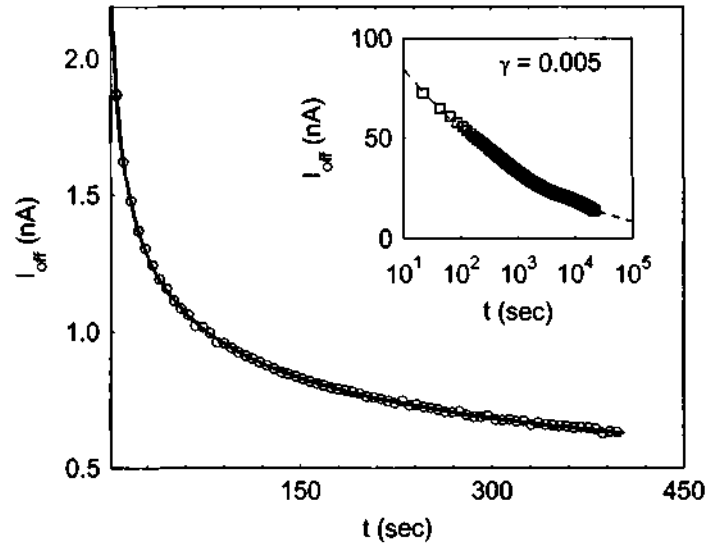


**Fig. 4.8** Slow relaxation (every 70<sup>th</sup> data points) of photocurrent for  $V_g = -32$  V,  $V_d = -40$  V at 100 K with SEDL fit (solid line). Inset shows the semilog plot of decay for  $V_g = -20$  V,  $V_d = -80$  V at 150 K. The curve is fitted to SEDL with unreasonable value of  $\gamma = 0.005$ .

characterized by a power law time decay of the mobility or diffusion in hydrogenated amorphous silicon [178]. In case of conjugated polymer such as poly(*p*-phenylenevinylene) (PPV), a power law time dependence of the decay rate was observed i.e.  $k(t) \sim t^{-\beta}$  [50,174]. Using the power law dependence and integrating Eq. (4.3), we arrive at the SEDL with  $\gamma = (1 - \beta)$ .

In case of PFET, though the characteristic decay response was primarily fitted to SEDL as shown in Fig. 4.8, there were a couple of discrepancies to adopt this model for interpreting the relaxation process involved. In such device structure, which possesses a controlled charge distribution under the influence of  $V_g$ , one should expect a device specific model for charge dynamics rather than a general law.

#### 4.3.3 Inappropriateness of Stretched Exponential Decay Law in PFET

The nature of the decay in PFET can be forcibly fitted to SEDL with high accuracy but physical inappropriateness. The insufficiencies of the model arising in particular are as follows: (i) The forcible fit of SEDL to the

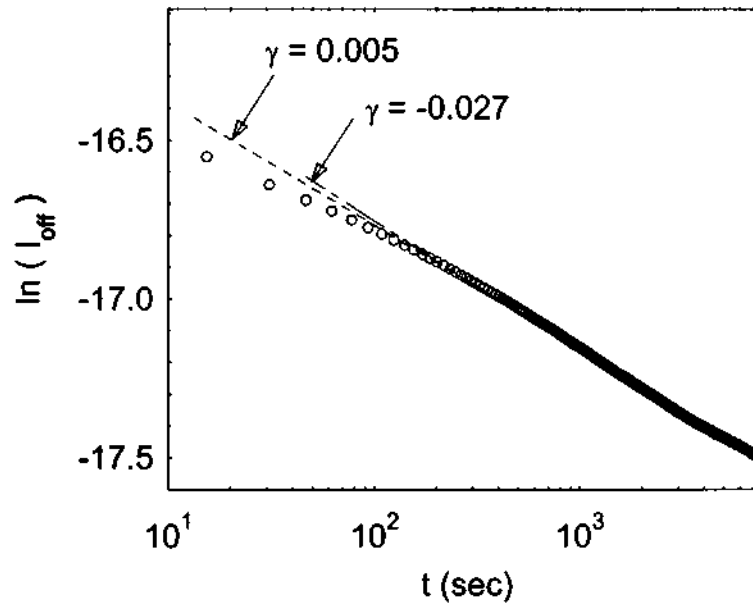
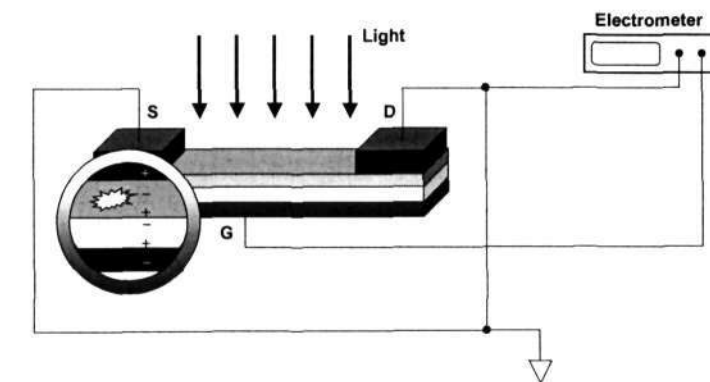


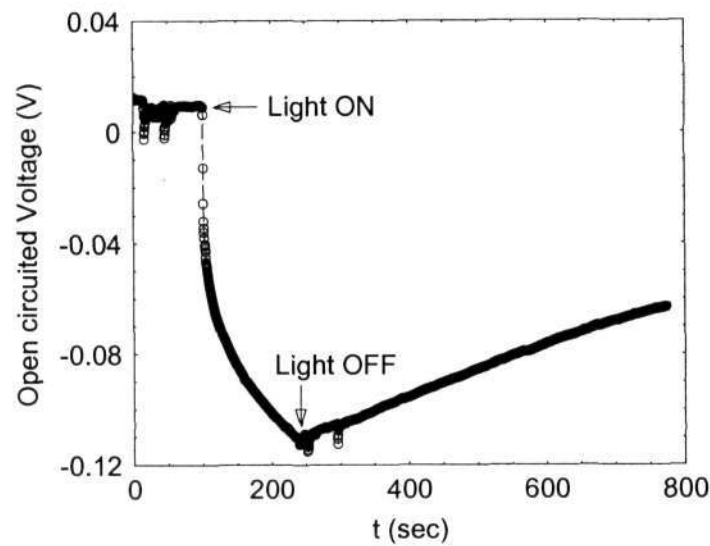
Fig. 4.9 Semilog plot of  $\ln(I_{off})$  versus time (every 70<sup>th</sup> data points) for  $V_g = -20$  V,  $V_d = -80$  V at 150 K. The data is fitted to SEDL (dashed lines) with nonunique  $\gamma$  value.

experimental curve yields an unreasonable  $\gamma$  ( $\gamma = 0.005$ ) value. This value is unrealistic and corresponds to a wide spread of trap energies and cross-sections without any further detail of the real process. (ii) There is no uniqueness in the model. As in Fig. 4.9, the same curve can be fitted to SEDL with different combinations of fitting parameters, which weaken the model in interpreting the photophysical processes. (iii) The fitting parameters for different  $V_g$  are not

correlated. This is unexpected since the mechanism should not vary with gate bias. Eventually, it becomes more complicated to explain the influence of  $V_g$  in build-up and relaxation of photocurrent. (iv) In SEDL, different physical mechanisms were proposed for rapid and slow components of the relaxation in the same system, which is quite unreliable and artificial concept. (v) This method doesn't provide adequate microscopic view of charge dynamics, which is important in such specific device.



(a)



(b)

**Fig. 4.10** (a) Experimental set up for measuring open-circuit voltage between the gate and shorted drain-source. (b) Transient of open-circuit voltage upon exposing light ( $\lambda = 632.8$  nm).



#### 4.3.4 Experimental Verification of Charge Dynamics in PFET

The motion of the PCC was probed by detecting the open circuit voltage developed between the gate and shorted drain-source ( $V_d = 0$ ) during photoexcitation and relaxation process. The experimental set up is displayed in Fig. 4.10(a). A clear open-circuit voltage ( $V_{gso}$ ) signal of  $\sim 120$  mV (for  $\lambda \approx 632.8$  nm, incident power  $\approx 1$  mW/cm<sup>2</sup> on the channel region), as shown in Fig. 4.10(b), was observed. The possible motion of the positive charge carriers towards the interface leaving the less mobile negative charge carriers in the bulk can be suggested to corroborate the observed result. The charge carrier generation in the bulk is common to both depletion and accumulation modes and has no direct dependence on  $V_g$ , as it is hardly accessed by the associated field. The transient profile of this voltage as shown in Fig. 4.10(b) can be attributed to the redistribution of the photoinduced charge carriers and the RC time constant of the configuration.

#### 4.3.5 Model of Spatial Charge Separation

The inconsistency in stretched exponential decay demands to adopt a better model to describe the microscopic picture of the decay dynamics of PCC in PFET. A model based on time evolution of spatial separation of the excess charge carriers is more appropriate and feasible in the present case, which relies on an identical physical mechanism for recombination for the rapid and slow segments of decay. The model was first proposed by H. J. Queisser to explain the nonexponential relaxation of PCC in a system consisting of conducting  $n$ -type gallium arsenide ( $n$ -GaAs) grown on insulating chromium-doped GaAs (Cr: GaAs) [180,181]. The PCC was assumed to be separated due to the potential barrier arising at surfaces, interfaces, junction or fluctuations of composition or doping. Similar situation can be realized in PFET under accumulation mode. The channel near the interface and the bulk region of the semiconductor can be considered as the conducting and insulating media, respectively.

Upon illumination, the *positive* and *negative* charge carriers (to be stated often as *holes* and *electrons*, respectively from now onwards) are separated due to the field distribution inside the device. The holes move towards the insulator/semiconductor interface due to drift and diffusion processes as they find their minimum potential in the comparatively higher ordered region. On the other hand, the electrons, which are less mobile in the disordered system, are localized and trapped in the bulk maintaining a distribution after being photoexcited. The separation of charge carriers and the direction of their motion were reflected in open-circuit voltage experiment, as mentioned in the previous section. The photoexcited holes govern the transport property, whereas the distribution of trapped electrons dictates the relaxation dynamics. Upon termination of light, holes recombine with the trapped electrons following the serial relaxation process. The more distant carriers are likely to be recombined with progression of time and this results in the sluggish rate of decay. The mathematical representation of the current decay can be derived by correlating the spatial distribution of charge carriers with time evolution.

The rate equation representing the recombination process of PCC is as follows

$$\frac{dn(x,t)}{dt} = -[n(x,t)/\tau_0] \exp(-2x/a) \quad (4.4)$$

where  $n(x,t)$  is trapped negative charge density persisting after time interval  $t$  from termination of the disequilibrating illumination,  $a$  is the Bohr radius of the positive charge carriers and  $\tau_0$  is carrier lifetime of uniform bulk material (e.g.  $\tau_0 \sim \mu\text{sec}$  for PPV [182]). The  $x$ -axis extends toward the bulk and  $x = 0$  corresponds to a discrete channel-bulk boundary. By solving Eq. (4.4) for  $n(x,t)$  in terms of  $t$  and assuming  $t \gg \tau_0$ , which is valid for many practical purposes, the *excess conductivity* due to PCC can be expressed as

$$\sigma_{\text{off}}(t) x_p = \mu_h e \int_0^{\infty} n(x,t) dx \approx \mu_h e \int_0^{\infty} n(x,0) dx \quad (4.5)$$

where  $n(x,0)$  corresponds to the density of trapped negative charges at  $t = 0$ ,  $e$  is the charge of the majority carriers having mobility  $\mu$  ( $= \mu_h$ ) within the conducting channel of thickness  $x_p$ . In the present system, a rectangular distribution of trapped electrons is considered to be extended up to a certain length  $x = l$  at time  $t = 0$ , i.e.  $n(x,0) = Z$ , the volume density of traps, in the

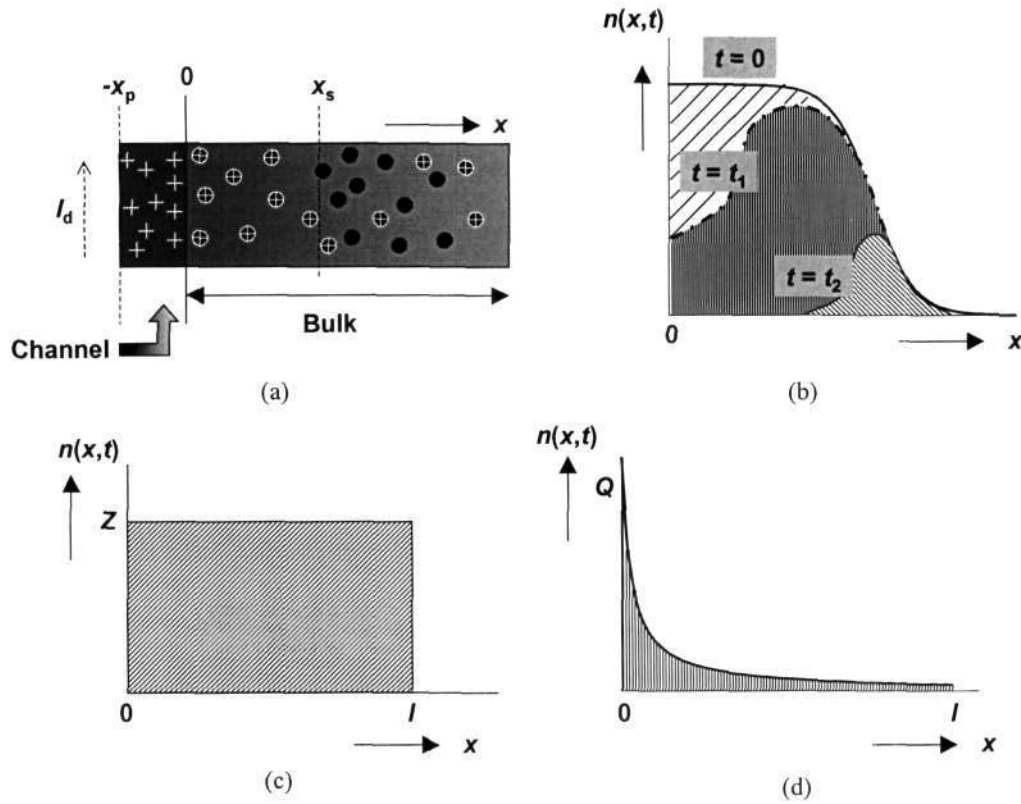


**Fig. 4.11** (a) Photoinduced charge separation scheme in PFET. Conducting channel shows the distribution of excess holes contributing the additional current to  $I_d$  (as shown the direction). In the bulk, a zone containing recombined electron-hole are separated from the trapped electrons (black spots) by a front (dotted line) at  $x_s$ . The origin ( $x = 0$ ) is at the channel-bulk interface and  $x = -x_p$  corresponds to the insulator-semiconductor interface. As time progresses, the front approaches to the right recombining more electrons to recover initial equilibrium. (b) Trapped-electron volume density profile  $n(x,t)$  in the bulk for times  $t = 0$ ,  $t = t_1$ ,  $t = t_2 > t_1$  after switching off illumination at  $t = 0$ . The area under the curve represents the remnant charge, whereas that above the curve represents the charge having recombined up to the particular time ( $0$ ,  $t_1$  or  $t_2$ ). (c) Rectangular distribution (logarithmic decay law) and (d) coulombic distribution (double log decay law) of the trapped electrons.

interval  $[0, l]$  and zero elsewhere. At time  $t$ , all carriers having a lifetime  $t + \tau_0$  can be assumed to have recombined. The effect of recombination can be

realized clearly by considering that a sharp front, which separates the unrecombined localized electrons from the already recombined counterpart, moves along the  $x$ -axis, as shown in Fig. 4.11 schematically. The position of the front relates the time through a spatial distribution  $\tau = \tau_0 (2x/a)$ , which can be obtained from the denominator of Eq. (4.4). The lifetime  $t + \tau_0$  corresponds to the position of the front  $x(t) = (1/2) a \ln [1 + (t/\tau_0)]$ , which can be treated as the lower limit of Eq. (4.5) to find the conductivity. Integration of Eq. (4.5) by substituting the rectangular distribution finally yields

$$\sigma_{\text{off}}(t) = \sigma_{\text{ini}} - \frac{1}{2x_p} e\mu_h aZ \ln(t/\tau_0), \quad \text{for } t \gg \tau_0 \quad (4.6)$$

where  $\sigma_{\text{ini}}$  represents the initial conductivity. The concept of spatial distribution of the carriers, used in this model, is justifiable specifically for FET geometry

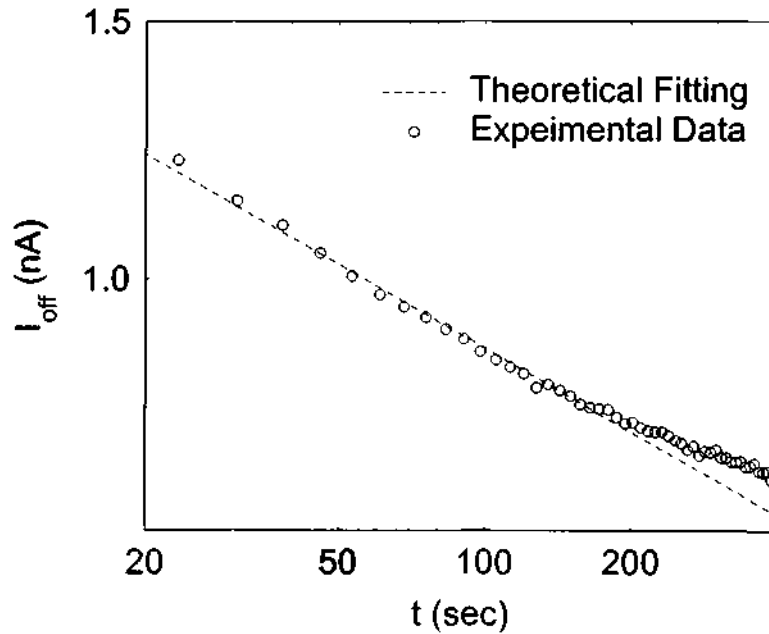
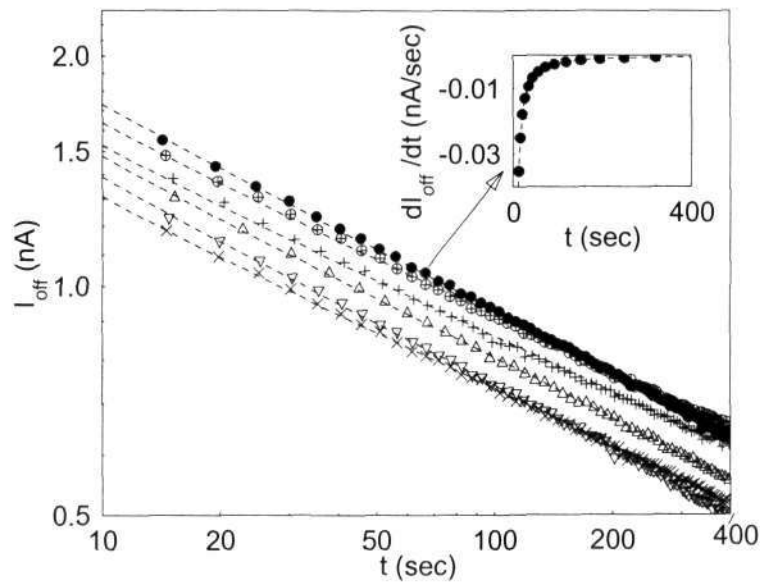


Fig. 4.12 Log-log plot of photocurrent decay (data points) at  $V_d = -40$  V,  $V_g = -16$  V upon switching off light. The experimental curve is fitted to logarithmic decay law (dashed line).

under photoexcitation. The  $V_g$  dependence of photocurrent decay can be taken to be a measure of the parameter governing the spatial distribution. The associated physical arguments arise from a possible presence of an in-built field, which modifies the transistor characteristics, and the charge carrier generation.

Upon switching off the light source, the field redistribution and the recombination causes the current decay. The rate of recombination decreases progressively, accompanied by the relaxation of the built-in field. In the longer time scale the decay process is governed by the recombination of charge carriers separated by larger distances.

The fitting to this model using Eq. (4.6) is satisfactory for the initial duration ( $t < 200$  s). At longer duration a subtle deviation to the model appears, as shown in Fig. 4.12 (dashed line). The discrepancy arises due to our initial



**Fig. 4.13** Log-log plot of photocurrent relaxation  $I_{\text{off}}(t)$ , along with fit to Eq. 4.8 at different  $V_g$ . Inset shows the fitting of the model with the derivative of the experimental curve.

assumption based on the rectangular distribution of trapped negative charges. In the present device, the rectangular distribution does not portray a realistic distribution of the spatial of the negative charge carriers in the bulk. A more appropriate and physically explainable distribution can be of the form  $n(x,0) = Q/x$  within the region  $0 < x \leq l$  and zero elsewhere, where  $Q$  is the  $V_g$  dependent parameter expressing the density of the negative charges. This distribution is intuitively explained by taking the mutual interaction between the proximal electrons into consideration and indeed supports the hierarchy of the

system. On substitution of this distribution along with the same limit as described earlier and assuming  $t \gg \tau_0$ , Eq. (4.5) leads to

$$I_{\text{off}}(t) = I_{\text{ini}} - I_{\text{dec}} \ln[\ln(t/\tau_0)] \quad (4.7)$$

where  $I_{\text{dec}}$  is linearly proportional to  $\mu_h$ ,  $a$  and  $Q$ , governing the decay rate. This is obviously a slow decaying function as compared to the single logarithmic law. The experimental points are fitted with Eq. (4.7) over the entire duration with a higher resolution (standard error < 0.3%, correlation coefficient  $r^2 > 0.99$ ), as shown in Fig. 4.13 (dashed lines). A high degree of fitting was observed indeed in the instantaneous time derivative of the experimental data, as shown in Fig. 4.13 inset. It is to be noted that  $I_{\text{off}}(t)$  is a measure of excess current, which means that it is the difference between the photoinduced  $I_d$  and dark  $I_d$ .

#### 4.3.6 Importance and Gate Bias Dependence of Fitting Parameters

The two fitting parameters involved in Eq. (4.7) can merely describe the

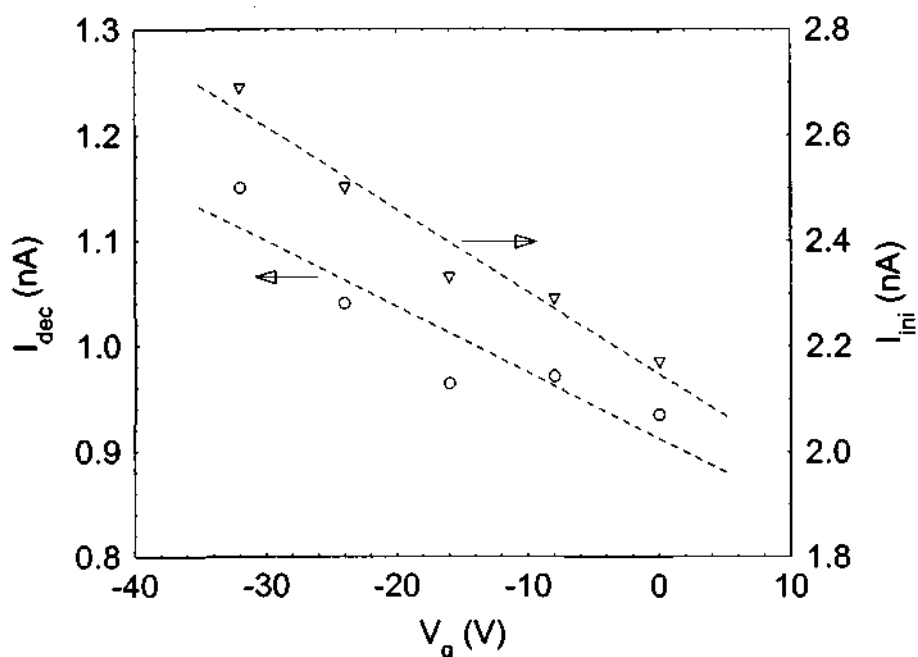


Fig. 4.14 Plot of decay-fitting parameters  $I_{\text{dec}}$  and  $I_{\text{ini}}$  as a function of  $V_g$ .

relaxation of PCC over a larger time period.  $I_{\text{ini}}$  can be defined as the excess current persisting at  $t = 2.7$  sec after termination of light. The other parameter

$I_{dec}$  can be defined as the decrease of current from  $t = 2.7$  sec to  $t = 15$  sec after switching off the source of illumination. The correlation between the two parameters essentially suggests that the decay process depends on the initial value. This describes the different rate of recombination of the excess charge carriers depending on the degree of disequilibrium. It is also to be noted that the relaxation process over wide time scale is governed by the two parameters, which mainly depend on the early component of the relaxation. It also preserves the characteristics of the mechanism for rapid and slow components of the decay.

A discernible linear  $V_g$ -dependence was observed for both  $I_{ini}$  and  $I_{dec}$ , as shown in Fig. 4.14. This can be attributed to the direct or indirect impact of  $V_g$  on the distribution of trapped electrons, hole mobility etc. The feeble effect of  $V_g$  on the photoinduced charge generation and relaxation emphasizes that charge separation and recombination largely take place in the bulk and are screened from the gate bias by a large distribution of charge density within the channel region.

#### 4.3.7 Build-up of Photoinduced Charge Carriers in PFET

The build up of photoinduced excess current  $I_{on}(t)$  for different  $V_g$  is shown in Fig. 4.15. The value of  $I_{on}(t)$  exhibits logarithmic dependence of time as shown (dashed lines) in Fig. 4.15. According to the model given by Queisser *et al.* [183] the logarithmic dependence of  $I_{on}(t)$  on cumulative photon dose implies a spatial separation of PCC at the interface between conductor and insulator. The interface potential between the  $p$ -layer and the bulk, in particular, renders the separation of PCC with the negative charge diffusion to the bulk and gets localized in the trap sites. The explanation of the accruing conductance was attributed to the available trap sites. An increase of  $I_{on}(t)$  with respect to negative  $V_g$  was observed. This can be primarily attributed to the higher drift/diffusion rates of the photo-generated positive charge from the bulk to the channel region where the potential of the positive charge is significantly lowered. The negative charge carriers would also tend to diffuse into the bulk

and the spatial-access can increase with increasing  $V_g$  in the accumulation mode.

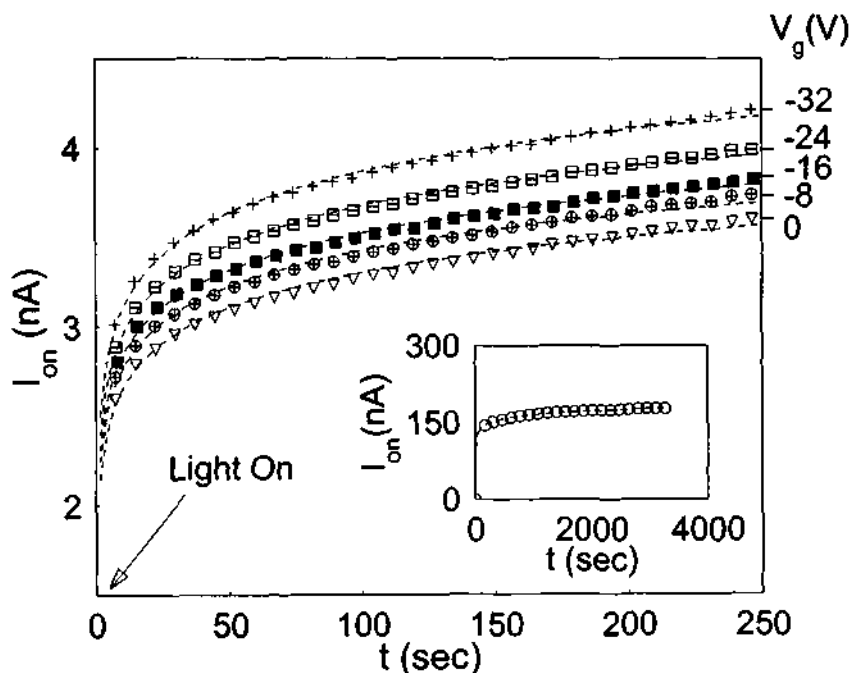
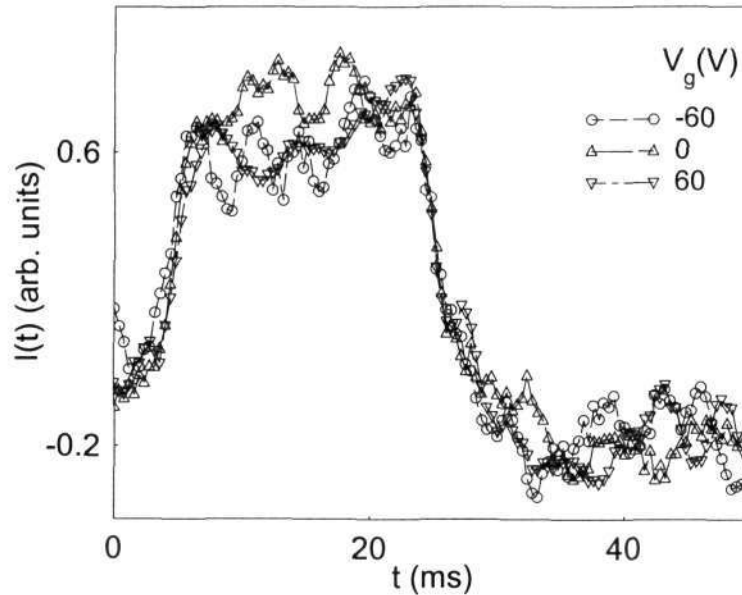


Fig. 4.15 The build up of photoinduced current  $I_{on}(t)$  for different  $V_g$ , along with logarithmic time dependence (dashed lines) under  $V_d = -40$  V at 100 K. Inset is the  $I_{on}(t)$  for a device from a different batch under  $V_d = -80$  V and  $V_g = -20$  V at 150 K over a longer time regime (every 500 data points is displayed).

#### 4.3.8 Photoresponse of PFET under Short Pulse Mode

The initial stages of the decay in the sub millisecond range can be evaluated from the ac response of  $I(t)$  to short periodic light pulses as shown in Fig. 4.16. Two distinct features were observed from these experiments: (i) The ac peak-peak response of  $I(t)$  was at least three orders less than the total change of dc current obtained from long duration light-exposure. (ii) The ac response, which was a signature of fast response ( $< 20$  msec), did not show any discernible dependence on  $V_g$ . The  $V_g$  dependence of the current decay was observed at longer time scales when the electrons and holes are well separated from each other. The difference in  $V_g$  dependence can then be attributed to a more effective screening at higher density of PCC, which prevails at the early stages.





**Fig. 4.16** Short pulse (21 ms) response  $I(t)$  in ac mode for different  $V_g$ , as marked in the figure.

#### 4.3.9 Validity and Limitation of the Model of Spatial Charge Separation

It was observed that the model of spatial charge separation is much more physical and can provide better insight into the photoinduced effect of polymer based transistors. The strength of this model lies in the involvement of only two fitting parameters to interpret the relaxation over a large time span. The relaxation of charge carriers over more than four hours was fitted to Eq. 4.7 (Fig. 4.17) with excellent resolution that validates the applicability of this model in the specific system. Moreover the model also satisfies all the three postulates for serial relaxation. The first requirement of dynamical process rather than mere statistics is proven throughout the model. The second requirement demonstrating the constraint over large time scales is also valid in the present model as the trapped electrons closer to the channel-bulk interface screens the further lying traps and must be removed first before more distant charge is affected. Finally, the hierarchy, in particular, is simply described by the rapid recombination of the proximal charge carriers followed by the slow relaxation of the distant charges.

However, the model has a couple of minor limitations. Firstly, the model holds for low temperatures since the trapped electrons are assumed to be

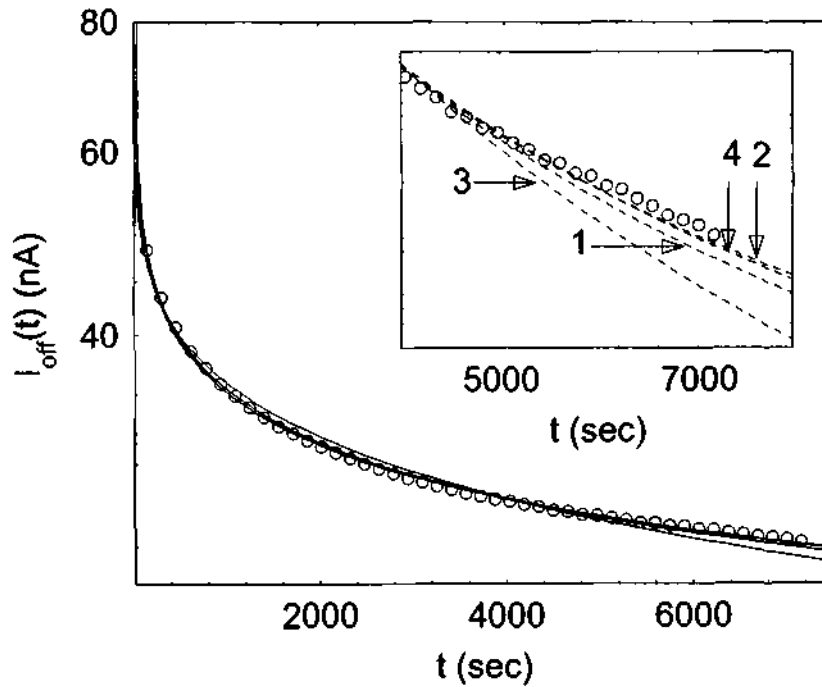


**Fig. 4.17** Photocurrent relaxation for  $V_d = -80$  V,  $V_g = -20$  V (data points). The curve is fitted to different models. Inset shows the enlarged view of the fitting to SEDL (1 & 2), logarithmic decay (3) and double-log decay (4) at the larger scale of time. Note that  $I_{off}(t)$  represents the magnitude of excess current.

stationary. But at finite temperature the electrons are able to move due to thermalization. This eventually accelerates the motion of the front. To maintain such condition, all the experiments were carried out at low temperature with low light intensity. Secondly, trap-assisted transport for holes is neglected in this model, which may modify the decay process. Thirdly, the model cannot explain the early stages ( $t < 2.7$  sec) of the relaxation. This is because of the primary assumption of coulombic distribution, which becomes undefined as  $t \rightarrow 0$ . This shortcoming does not suppress the usefulness of the model since the purpose of the model is to explain the prolonged relaxation rather than the early stages. Finally, the relaxation process may not be true in depletion mode because the primary assumption of interface between the channel and bulk

cannot be obtained in depletion mode. The comparison of different decay models is summarized in Table 4.2.

Table 4.2 Comparison of different decay models

Curve No.	Description	Quality of Fit	Fitting Parameters	Comments
1	SEDL	$r^2 = 0.998$	$\gamma = 0.058$ $\tau = 9 \mu\text{sec}$	Best fit; Unreasonable fitting constants
2	SEDL fitted to $\ln(I_{\text{off}})$	$r^2 = 0.998$	$\gamma = 0.005$ $\tau$ – undefined	Lack of uniqueness
3	Logarithmic Decay	$r^2 = 0.988$	$I_{\text{ini}} = 7.65 \text{ nA}$ $I_{\text{dec}} = 5.88 \text{ nA}$	More physical but deviated in the larger time scale
4	Double-log Decay	$r^2 = 0.995$	$I_{\text{ini}} = 113 \text{ nA}$ $I_{\text{dec}} = 40.3 \text{ nA}$	More physical; Excellent fit

#### 4.4 SUMMARY

The photoinduced relaxation process in polymer transistor was studied with comprehensive experimental and theoretical supports. The slow nonexponential relaxation of photoinduced current was the predominant feature in all the devices. The experimental results were discussed in the context of many possible models. The model, based on the spatial separation of charge carriers following serial relaxation due to hierarchy of the system was adapted successfully for the present system. The model was further modified to include a gradually decreasing function for the spatial distribution of the photogenerated negative charge carriers being trapped in the bulk. Microscopic view of dynamical model provides a better understanding in terms of the charge distribution and their dynamics in this device structure. The treatment can also be used to extract the trap distribution profiles inside the device.

## Chapter 5

### Optoelectronic Memory Effect in PFET

#### 5.1 INTRODUCTION

The extreme slow process and the control over slowness can be interpreted in terms of retention processes i.e., the ability to hold at a desired state for a finite time span. The equal ability to flip the system between two stable states forms the basis for a bistable memory device. Research on memory effects and related devices have shown tremendous potential for modern technology. Most of the conventional memory devices like two-terminal random-access memory (RAM), electrically programmable read only memory (EPROM), dynamic random-access memory (DRAM), flash memory etc. are operated electrically. The principle of operation of all the devices mentioned above is based on capacitive effect to store the charges in the system and the different status of memory state is detected depending on the resistance of the system. Memory devices based on organic materials have shown to be equally efficient with much smaller scale of size. For example, the conformational changes of the organic molecules depending on whether oxidized or reduced by the electrical response have been successfully exploited to achieve memory device [184,185]. Another novel approach by using a layer of metal nanocluster, sandwiched between two organic layers to obtain bistable memory effect has been reported recently [186]. An extensive research on organic based memory device is currently pursued in different laboratories to obtain high performance, high density (i.e. smaller in size) device structure using inexpensive processing techniques.

In the present case, as seen from the earlier chapter (section 4.3.2), the prominent slow decay of photoinduced current over several hours in PFET forms a basis for exploring memory features in OTFTs. The added feature of this decay was the observation of strong control of  $V_g$  over the excess charge carriers was observed prominently in the device when it was subjected to

depletion mode of operation. The considerable photomultiplication during light exposure followed by a slow relaxation upon termination of light was exploited to store the charges in this system. This aspect is another important component in the memory process. The present chapter deals with the control of relaxation process by  $V_g$  with certain initial conditions. The write, store, read and erase operations in a single device structure using the combination of the  $V_g$  and incident light source are presented in the following sections along with a discussion on various possible sources related to these novel features.

## 5.2 MEMORY EFFECT IN TRANSISTOR UNDER DEPLETION MODE

Unlike accumulation mode, the dynamics of photoinduced charge carriers was observed to be strongly dependent on the gate bias at low temperature. The ultra-slow relaxation of the excess charges led to a form of charge-storage within the device. The demonstration of the memory operation was essentially based on the manipulation of this stored charge.

### 5.2.1 Photoinduced Charge Dynamics in Depleted Transistor

In depletion mode, the majority charge carriers (holes) are pushed away

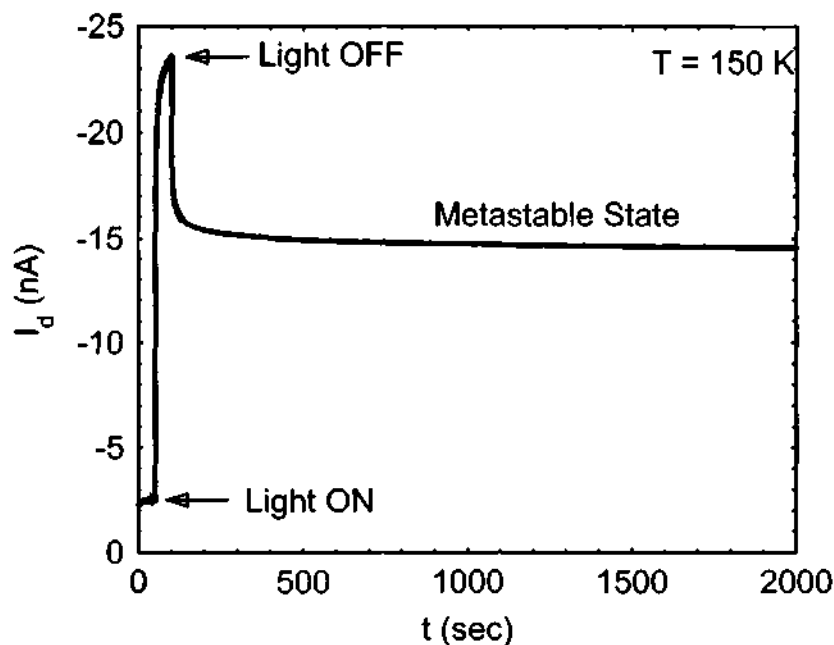
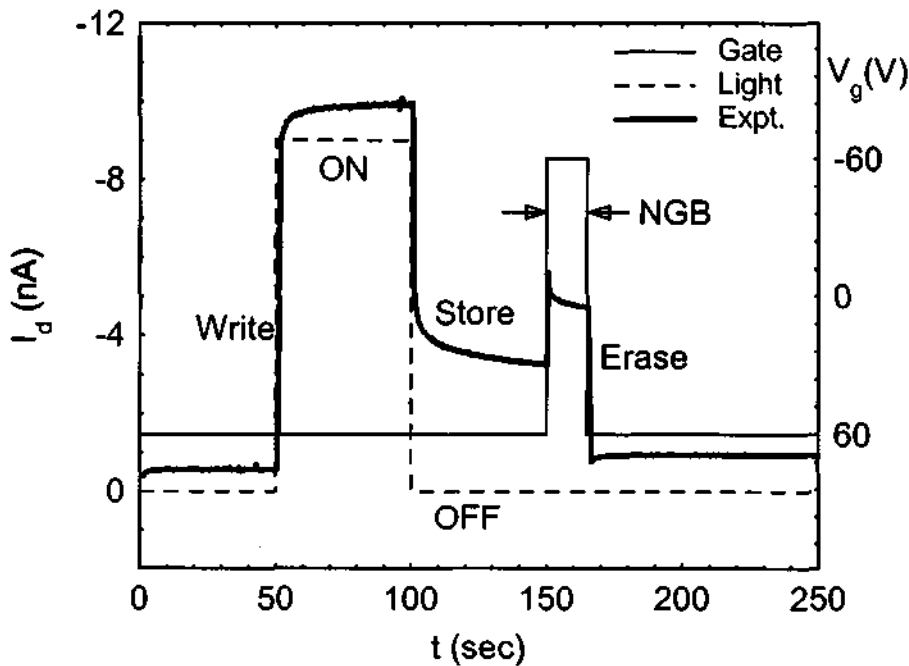


Fig. 5.1 Transient photocurrent response of PFET under depletion mode ( $V_g = 60$  V,  $V_d = -60$  V) at 150 K.

from insulator-semiconductor interface. The low density of holes in the channel results in an off state (low  $I_d$ ), in presence of an electric field set-up by the immobile negative interfacial-charge carriers. This high field region promotes charge generation and charge separation upon photoexcitation. A high photomultiplication in the background of low dark current is different from the situation in accumulation mode. The typical photoresponse under depletion mode is shown in Fig. 5.1. A considerably high response was observed followed by a persistent behavior upon switching-off the source of illumination. The ultra-slow relaxation of photoinduced charge carriers turns the device into a metastable state. This can be recognized as storing of charge carriers even after removal of the source of photogeneration. The relaxation process, however, is distinctly different from decay features in the accumulation mode.

**5.2.2 Memory Operation in Polymer Field-Effect Transistor**

The access to the transport region by  $V_g$  and light can be exploited to achieve memory effect in polymer transistor. The characteristic response,



**Fig. 5.2** Optoelectronic memory effect in PFET (thicker solid line) at 20 K upon using light (dotted line) and gate bias (solid line) as the two input parameters.

describing a complete cycle of operations at  $T = 20$  K, was observed in a single transistor structure, as displayed in Fig. 5.2. The initial data ( $0 < t < 50$  sec) shows dark  $I_d$  of the FET, operated at  $V_d = -60$  V and  $V_g = 60$  V. This state can be assigned as '0'. The *write* operation was executed by exposing light ( $\lambda = 632.8$  nm;  $33$  mW/cm<sup>2</sup> without any correction for dispersion in glass window) through drain-source electrodes and P3HT for 50 sec ( $50 < t < 100$  sec). A current of about 10 nA was arrived upon photoexcitation, which did not undergo appreciable change with respect to time. Upon termination of light, the current was observed to decay down to  $\sim 3$  nA showing an apparent persistence (50% decay after more than 3 hours). This metastable state can be designated as '1' and can be stored for finite time. The information was removed by turning  $V_g$  to negative value (accumulation mode) for 15 sec (represented by NGB in figure) followed by the reversal of  $V_g$  to positive value again. This process can be regarded as an *erase* operation by which the device recovers to its initial dark state ('0' state).

### 5.2.3 Qualitative Description of Memory Effect

The observed results may arise from two plausible sources. The first possible reason is photoinduced charge generation and charge transfer across the semiconductor-insulator interface and trapped within the insulator. This may effectively screen the gate bias. This type of memory effect has been observed in many memory devices [187]. The other possible reason is charge generation and storage within the semiconductor. In this context, it is also an essential aspect to address the location of charge carriers that can be buried in the semiconductor. We speculate on the origins of these phenomena at a qualitative level and propose a model, which is consistent with the entire set of present observations and earlier results. The initial response, marked by the dashed line in Fig. 5.3, represents the dark current in depletion mode. The charge distribution inside the device is depicted in Fig. 5.3 schematically, showing a high field in the depleted region due to the presence of immobile negative charges.

During the photoexcitation process, the charges are assumed to be generated throughout the sample depending on the light intensity and local electric field (laterally or vertically). The photoinduced charge transport is

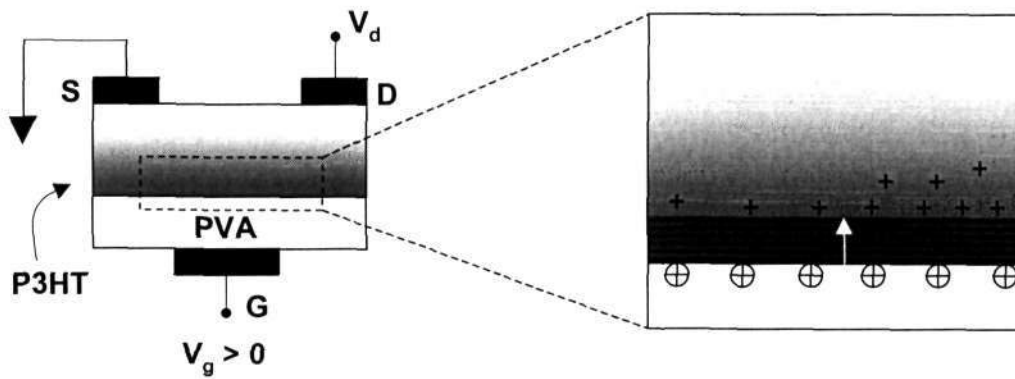
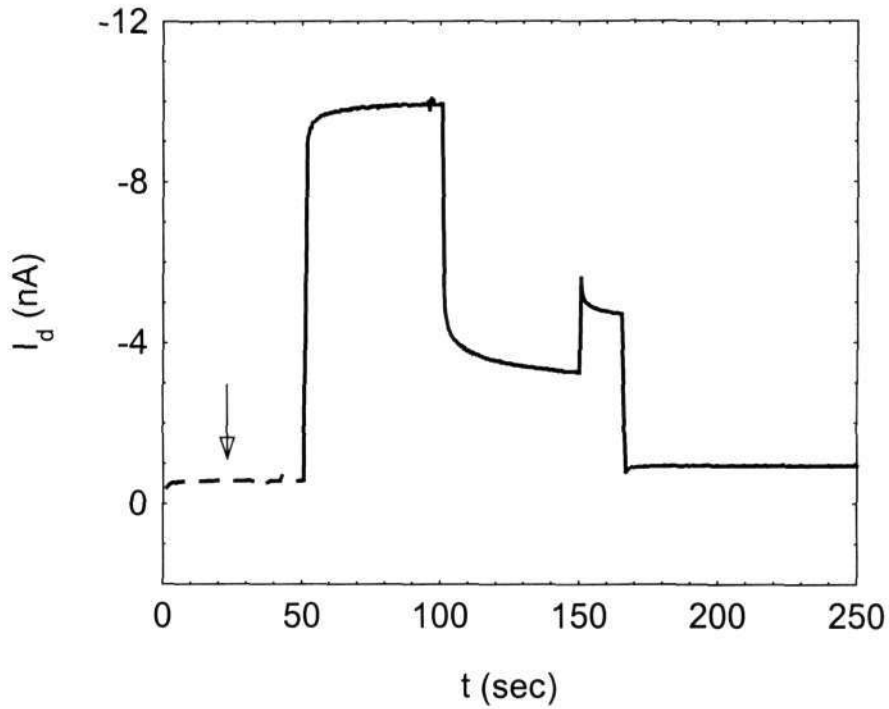
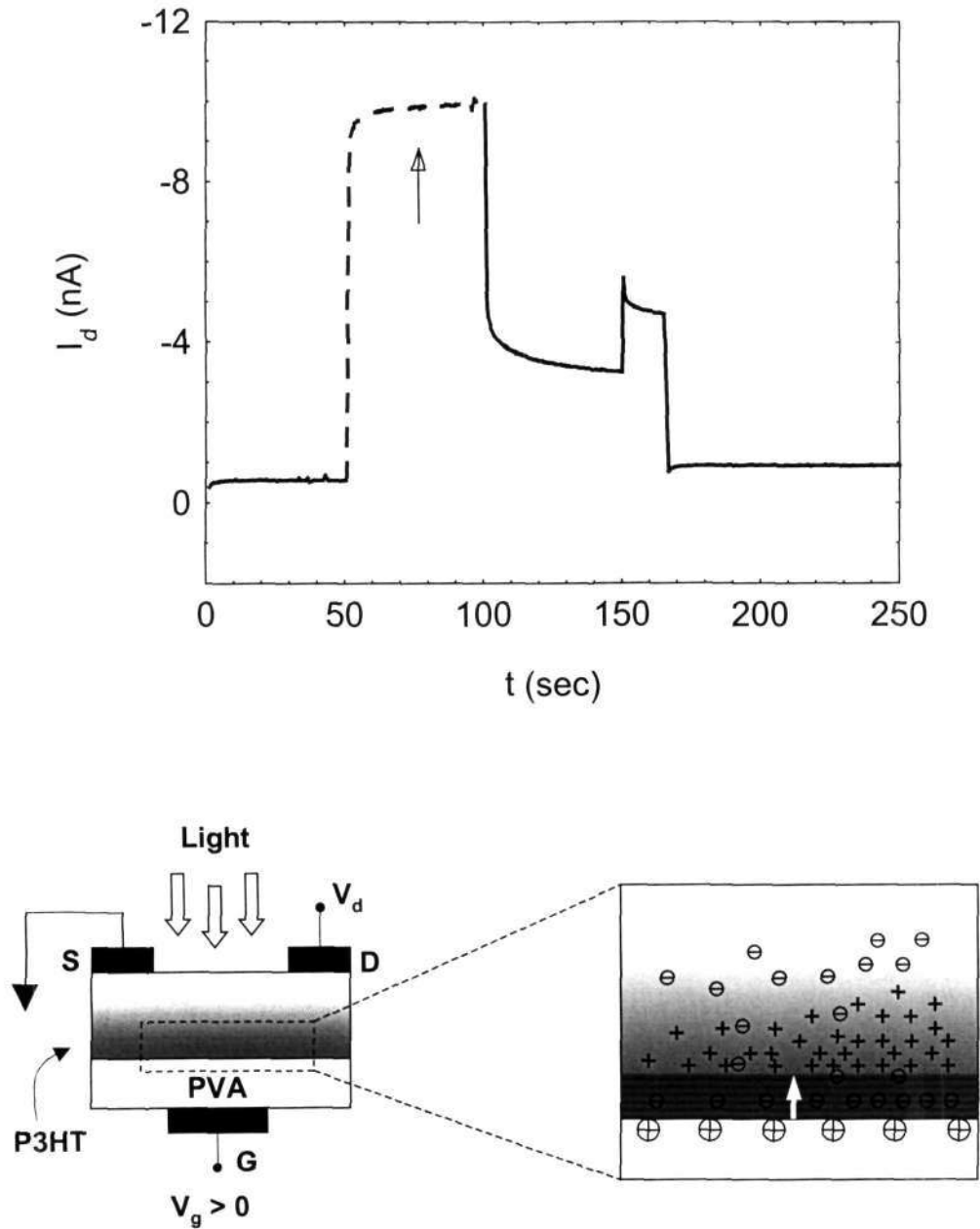


Fig. 5.3 Schematic diagram of charge distribution in PFET under depletion mode ( $V_g = 60$  V) manifesting the dashed portion of  $I_d$  as highlighted by the arrow (above).

predominantly contributed by holes, while the electrons are localized immediately after being generated. In depletion mode, the built-in field at the



interface opposes the proximity of the holes towards the interface. The holes



**Fig. 5.4** Schematic diagram of charge distribution in PFET under *write* operation (using light) manifesting the dashed portion of  $I_d$  as highlighted by the arrow (above).

within the depletion region drift away from the interface in presence of the high field. The electrons, on the other hand, are trapped within the depletion region. This type of motion of holes and electrons near the interface is strongly  $V_g$ -

dependent since the extent of the field associated with depletion region is limited to few layers from the interface. The holes, which are generated in the

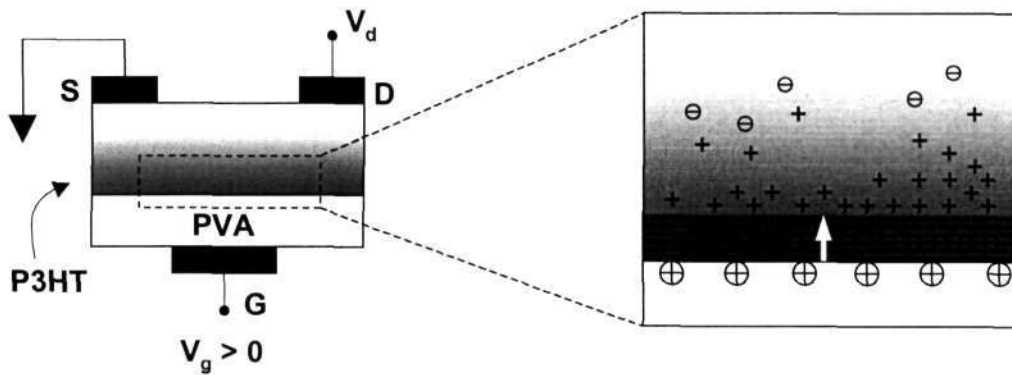
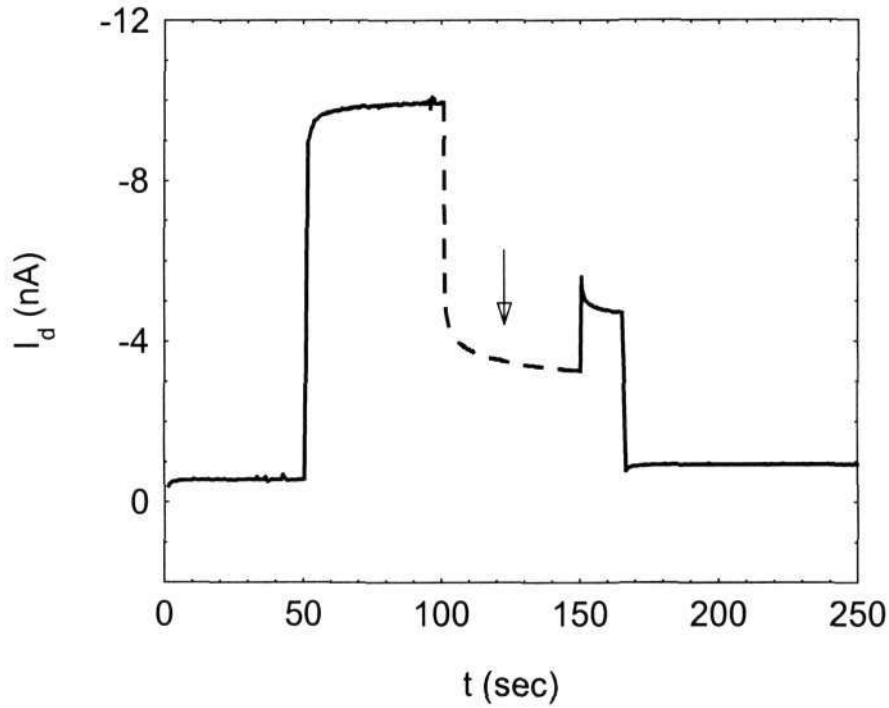


**Fig. 5.5** Schematic diagram of charge distribution in PFET under *store* operation (switching off light) manifesting the dashed portion of  $I_d$  as highlighted by the arrow (above).

bulk, are likely to converge to a minimum-potential route similar to the process observed in accumulation region (Chapter 4). This process is almost

independent of  $V_g$  since the corresponding field does not encompass the entire bulk. The schematic of charge distribution is shown in Fig. 5.4 (dashed line).

Upon termination of illumination,  $I_d$  decays rapidly due to the recombination of the proximal carriers describing the early stage of the

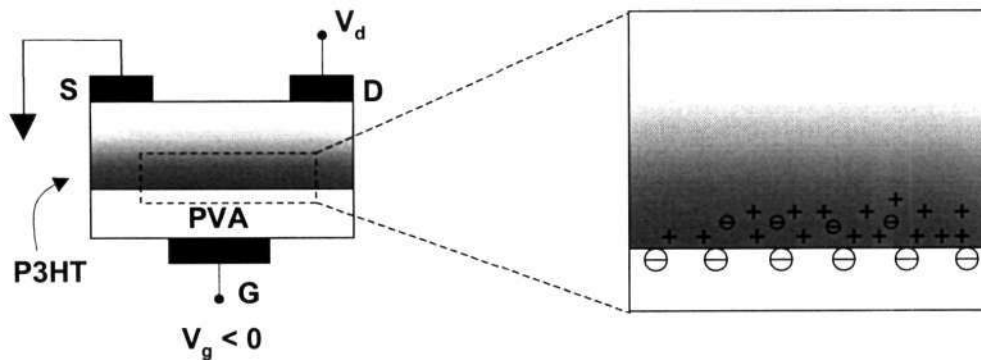
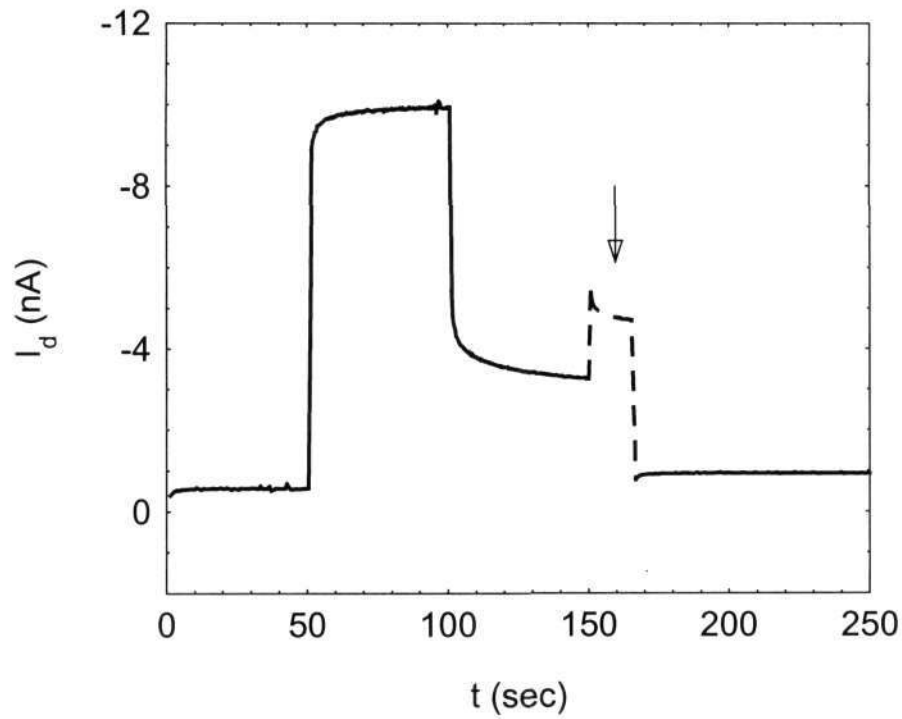


**Fig. 5.6** Schematic diagram of charge distribution in PFET under *erase* operation (using negative gate bias NGB,  $V_g = -60$  V) manifesting the dashed portion of  $I_d$  as highlighted by the arrow (above).

relaxation. Subsequently, the decay process is limited by the poor recombination cross-section of the trapped electrons within the depletion region

in presence of field. The trapped negative charged sites effectively screen the gate voltage and consequently lead to a higher  $I_d$  in the metastable state,

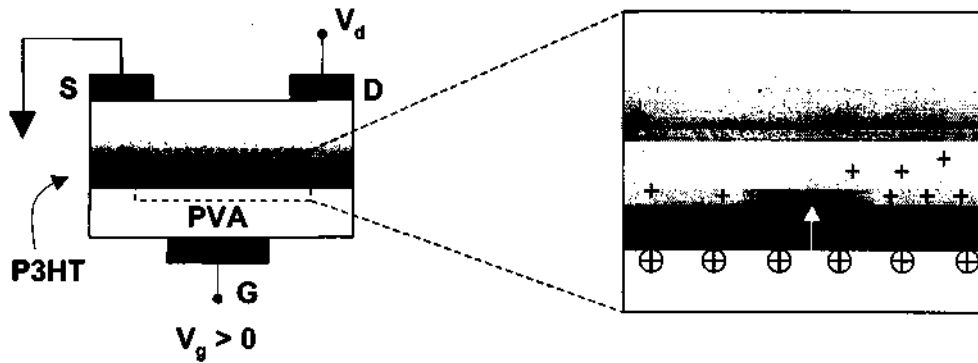
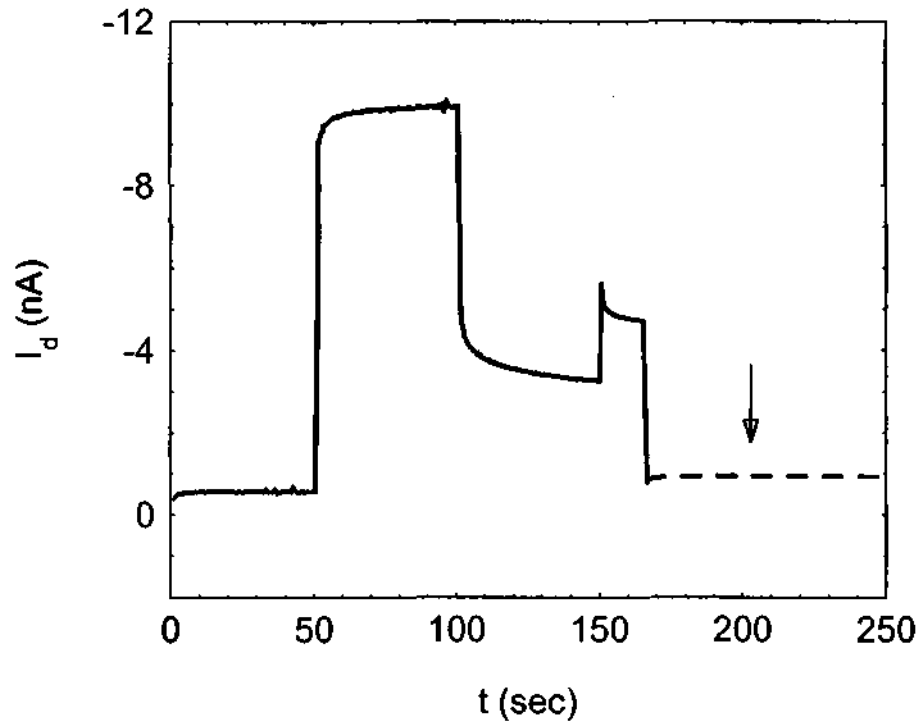


Fig. 5.7 Schematic diagram of charge distribution in PFET after recovery to initial dark condition manifesting the dashed portion of  $I_d$  as highlighted by the arrow (above).

compared to the dark value. The decay of  $I_d$  from this state is considerably slow and can be described by a double-logarithmic function of time, as shown in Fig.

5.5 (dashed line). The slow reduction of  $I_d$  is attributed to the bulk recombination, which is an indication of the slow non-exponential relaxation process inherent to the P3HT based devices. In this regime, the rate of recombination gradually decreases due to the increasing spatial distance between the carriers to be recombined. Upon applying a negative  $V_g$ , the hole accumulation at the interface results in the increase of  $I_d$  forming the channel region. However, this process is also accompanied by an increased rate of recombination around the electron trapping centres near the interface, resulting in appreciable decay of excess charge carriers. Both these processes are reflected in Fig. 5.6, where the initial increase in  $I_d$  is observed, after applying negative gate bias (NGB), followed by a relatively rapid decay.

Finally, the reversal of  $V_g$  into the depletion region takes the FET back to its original-initial value, as displayed in Fig. 5.7. The behavior of the resultant drain-source current  $I_d$  after termination of illumination can be described in terms of three components:

$$I = I_0(V_g) + I_{\text{gen}} - I_{\text{rec}}(N^*, t) + I_{\text{bi}}(E_{\text{bi}}) \quad (5.1)$$

where  $I_0$  is the dark value of drain-source current,  $I_{\text{gen}}$  represents the generation term,  $I_{\text{rec}}$  and  $I_{\text{bi}}$  are related to the recombination and a built-in field  $E_{\text{bi}}$  respectively and  $N^*$  is the excess charge. Upon switching off the light, the initial decay is governed by the intensity dependent early-recombination term. The system gradually reaches the metastable state by attaining the unstable equilibrium between the third and fourth terms, as the latter is related to built-in field associated with redistribution of charge carriers. Thus the current is maintained at a higher value. Upon application of NGB, the current rapidly attains the enhanced saturation value initially but afterwards decays rapidly. The decay is largely dominated by  $I_{\text{rec}}$ , which eventually sweeps almost all the excess charges and leaves the system under stable equilibrium.

#### 5.2.4 Dependence of Memory Effect on Light Intensity

The memory effect was studied for different intensities of light source. The current during the photoexcitation was observed to be dependent on light

intensity but upon switching-off the light, the same metastable state was arrived (Fig. 5.8). To characterize the effect we introduce a parameter, called the *retention factor* defined as the ratio of  $I_d$  in the metastable state to that in the illuminated state. A decrease of retention factor with increasing light intensity

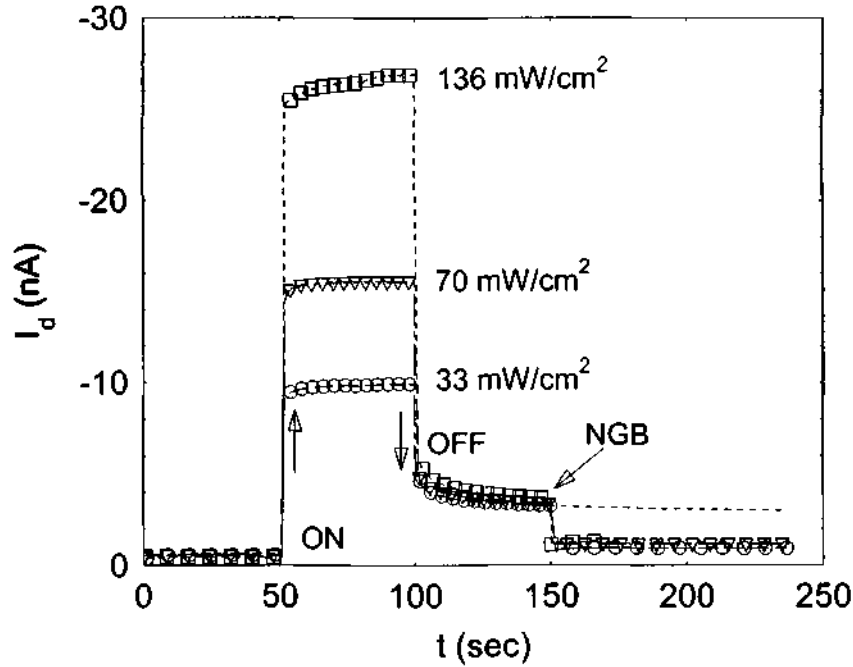


Fig. 5.8 Memory effect as function of light intensity. The dotted line indicates the metastable state insensitive to the light intensity.

was observed. At some critical intensity it could approach to unity. The trend was observed by reducing the intensity of light to  $158 \mu\text{W}/\text{cm}^2$ , as shown in Fig. 5.9. A clear unsaturated metastable state was observed in this case. The results can be interpreted consistently on the basis of the proposition mentioned in the previous section. The photogeneration of charge carriers increases with the intensity of light, promoting intensity-dependent  $I_d$  during illumination. Upon switching-off the source of illumination, recombination takes place among the proximal carriers of opposite signs. But the persistence appears due to the reduction of recombination cross-section of the electrons that are trapped within the high field depleted region. The recombination cross-section is restricted by the built-in field associated with  $V_g$ . This makes the metastable state

independent of light intensity though the number of excess charge carriers due

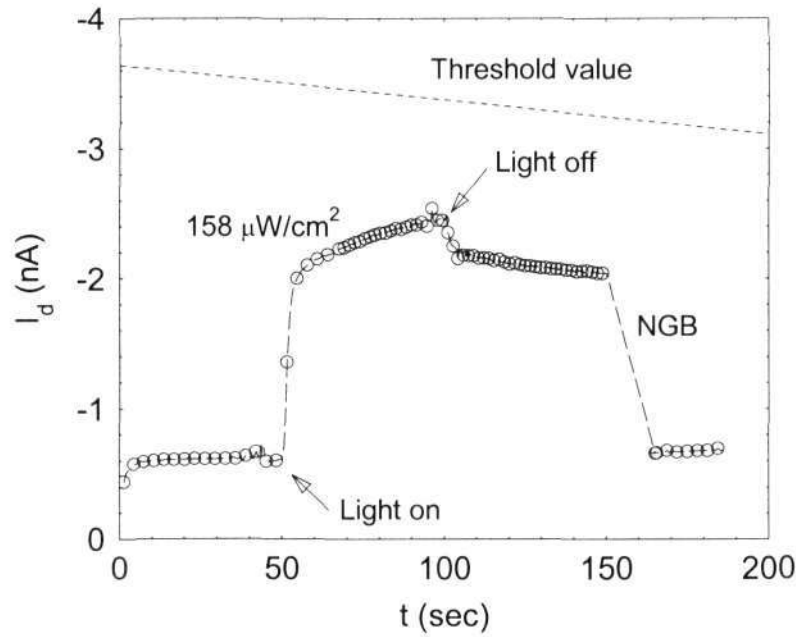


Fig. 5.9 Unsaturated metastable state due to low level of light intensity. The dotted line indicates the threshold value to attain intensity independent memory effect.

to the photoexcitation depends on the intensity.

### 5.2.5 Dependence of Memory Effect on Duration of Light Pulse

The memory effect was also verified with different pulse widths of the

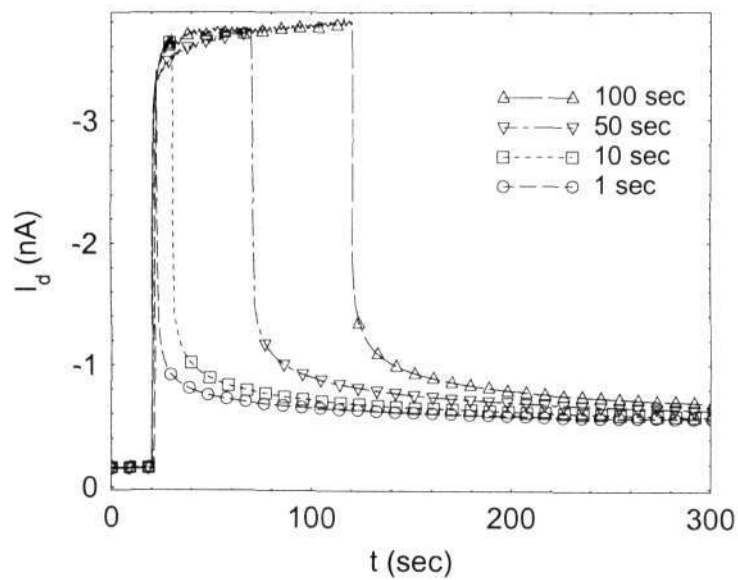


Fig. 5.10 Memory effect for different duration of exposure as marked by different symbols

exciting source ranging from 1 sec to 100 sec (Fig. 5.10). There was no influence of duration of light pulse on the memory effect as the same metastable state was achieved in all the cases. This reveals that the trapped charges and recombination rate solely depend on the gate voltage irrespective of the duration of light exposure (> 100 msec).

### 5.2.6 Effect of Temperature on Memory Effect

The entire memory effect was observed at low temperature ( $T = 20$  K). The same operations were carried out at  $T = 150$  K and 295 K to study the effect of

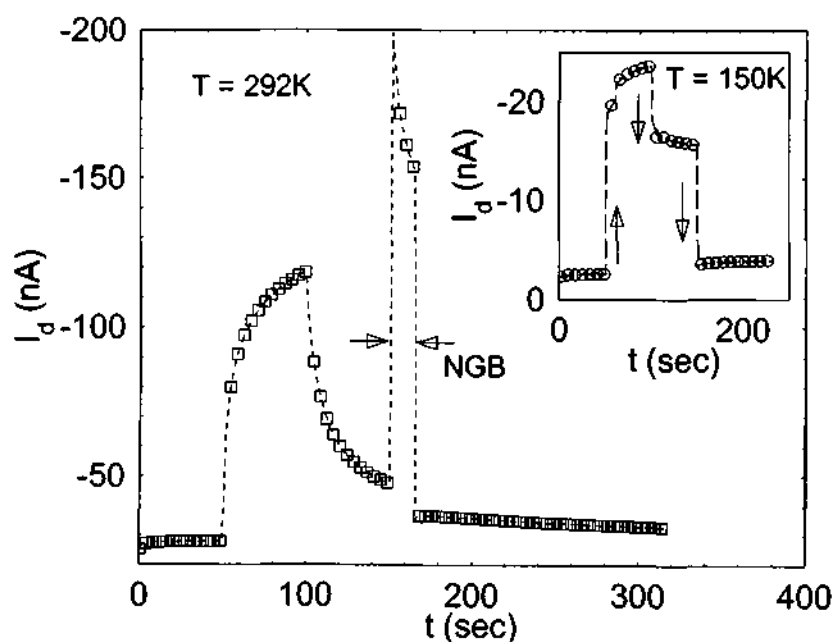


Fig. 5.11 Effect of temperature in memory feature. At room temperature memory effect disappears showing no retention of charge.

temperature (Fig. 5.11). The retention of charge carriers was observed to be strongly dependent on temperature. However, at  $T = 150$  K, the memory effect was visible with comparatively high value of  $I_d$ . This high value was attributed to the thermal energy to dissociate more number of charge carriers. But the effect almost disappeared at room temperature (292 K), showing no distinguished metastable state. The monotonic decrease of current upon switching-off the light offers no memory effect in the device. The absence of



memory effect can be attributed to the thermalization of the trapped electrons, which eventually enhances the recombination rate. At room temperature, substantial increase of  $I_d$  was observed when the device is subjected to a negative gate voltage followed by a rapid relaxation. This presumably indicates the appearance of built-in field within the depleted region.

### 5.2.7 Equivalence of Metastable State and Accumulation Mode

The level of  $I_d$  in the metastable state was apparently equivalent to the that of FET, operating in the accumulation mode under dark condition. This equivalence was verified by testing the  $I_d$ - $V_d$  under metastable state and comparing it with that obtained in normal accumulation mode. Figure 5.12

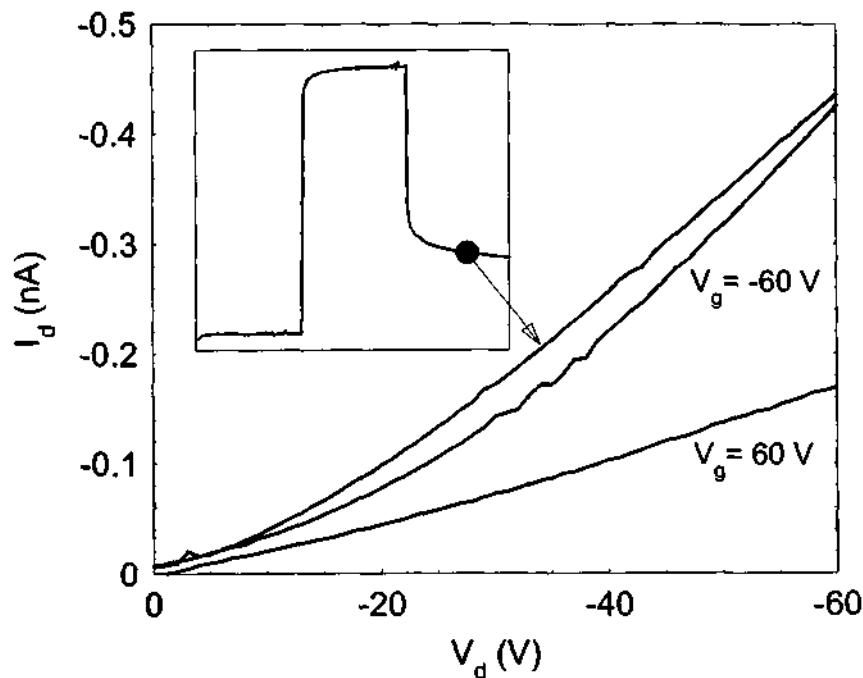


Fig. 5.12 Output characteristics of PFET for  $V_g = 60$ ,  $-60$  V, along with the curve corresponding to the metastable state, as represented by the point in the transient.

shows the output characteristics at  $V_g = 60$  and  $-60$  V (dotted lines) and that in metastable state (solid line). It was observed that the transistor output characteristic under metastable state almost resembled that in accumulation mode. This suggests that the redistribution of PCC in metastable state appears to provide the situation, which can effectively be attained by operating the FET in

the accumulation mode. The measurement was cycled without affecting the acquired memory effect. This also confirms that the memory effect was independent of  $V_d$  and the charges were stored near the interface rather than underneath the drain and source electrodes. From application point of view,  $V_d$  can be applied to read the information regardless of the writing, erasing and storing processes, which were mainly governed by  $V_g$ . The decoupling of photogeneration and transport of charge carriers adds a novel and hybrid memory feature in polymer transistor.

**5.2.8 Absence of Memory Effect in Accumulation Mode**

The memory effect was not observed when the operations were repeated with PFET, being initially in the accumulation mode. The complete cycle of memory effect and the transients were performed starting from the accumulation mode ( $V_g = -60$  V) of the FET. The photoresponse in

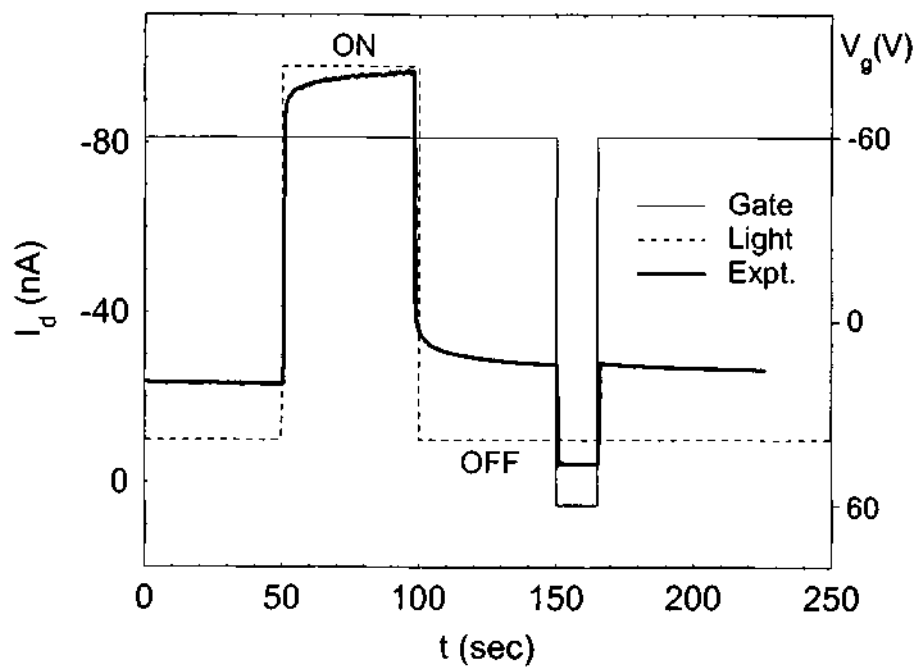


Fig. 5.13 Absence of memory effect in accumulation mode of PFET ( $V_d = -60$  V). The thicker solid line, thinner solid line and the light exposure represent the experimental curve, gate voltage, and the light exposure, respectively at 20 K.

accumulation mode resembles the typical behavior describing sequential relaxation process without any memory feature, as shown in Fig. 5.13. No

change of current was observed upon applying gate pulse of positive value ( $V_g = 60$  V). This strongly supports that the memory effect is related to the trapped electrons within the depleted region with reduced recombination rate. The possibility of the interfacial trap states, charge transfer and storage in the insulator to promote the memory effect can be ruled out completely, as those would also be expected to influence the memory effect in similar manner in case of accumulation mode. In particular, the photogeneration and relaxation in accumulation mode are essentially a bulk-dominated process being almost independent of  $V_g$ , as mentioned in the preceding chapter. Upon reversing  $V_g$ , however, dynamics of the excess charge carriers cannot be changed.

### 5.3 COMPARISON BETWEEN THE PHOTOINDUCED CHARGE DISTRIBUTION IN DIFFERENT MODES OF TRANSISTOR

The photoinduced charge generation and their dynamics follow different

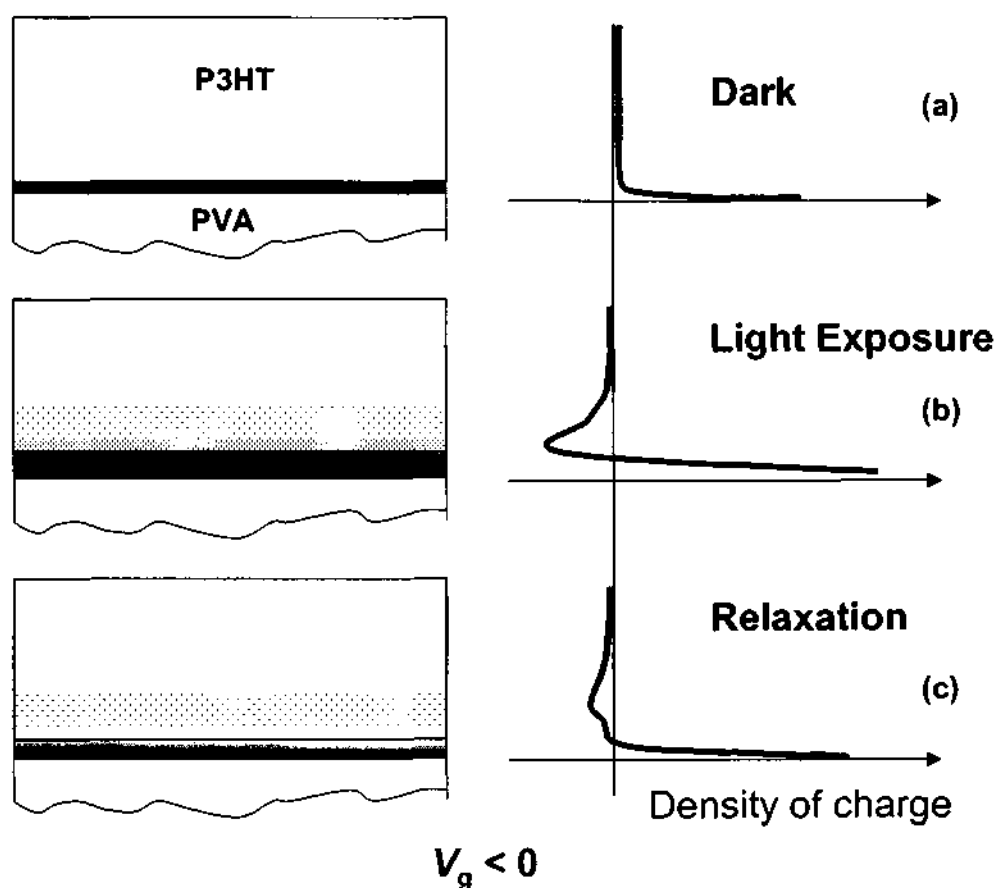


**Fig. 5.14** Schematic of charge density profile inside the polymer semiconductor with dark (a), light operation (b) and relaxation (c) under accumulation mode.

routes depending upon the mode of operation (i.e. accumulation or depletion). The more mobile holes, in principle, contribute to the transport process directly, whereas the less mobile trapped-electrons govern the decay process via recombination. One can speculate and come out with a schematic representation of charge density profile inside the device for different modes. In the context of this model, the charge density profile, describing the charge generation upon exposing light and the relaxation of charge upon switching off the light, has been schematically resolved in Fig. 5.14(a-c). Figure 5.14(a) shows the schematic of conventional charge distribution within the semiconductor when the FET is subjected to operate in the accumulation mode under dark condition. The density of hole is highly confined in the interface, forming the channel with high conducting state. It is to be noted that the hole-density profile is not uniform along the channel direction, as density is higher in source-gate region than that in drain-gate region. Upon exposing light, the excess carriers are generated in the bulk. The electrons are trapped in the bulk prevailing a distribution during the exposure, whereas the holes prefer to drift towards the channel contributing a large change in  $I_d$ . The density of holes inside the channel region increases largely, as shown by the gray region and density profile in Fig. 5.14(b). The trapped electrons, on the other hand, are distributed in the bulk with a gradual decrease away from the channel, as displayed by dotted region in Fig. 5.14(b). Upon switching off the light source, the field redistribution and the recombination cause the current decay. The rate of recombination decreases progressively, accompanied by the relaxation of the built-in field. The initial component of the decay is attributed to the recombination of the proximal charge carriers, whereas the delayed component is contributed by the recombination of the charge carriers separated with larger distances, as shown in Fig. 5.14(c). The negative quasi-static character of the charge distribution in the bulk (post photo-excitation stage) lends support to the Fig. 5.14(a-c) schematic.

The schematics of charge density profile in depletion mode are shown in Fig. 5.15(a–c), describing the different states of light-operation. Initially under dark condition, the holes are depleted from the interface forming a high electric field region (depletion region) composed of immobile negative ions, as shown

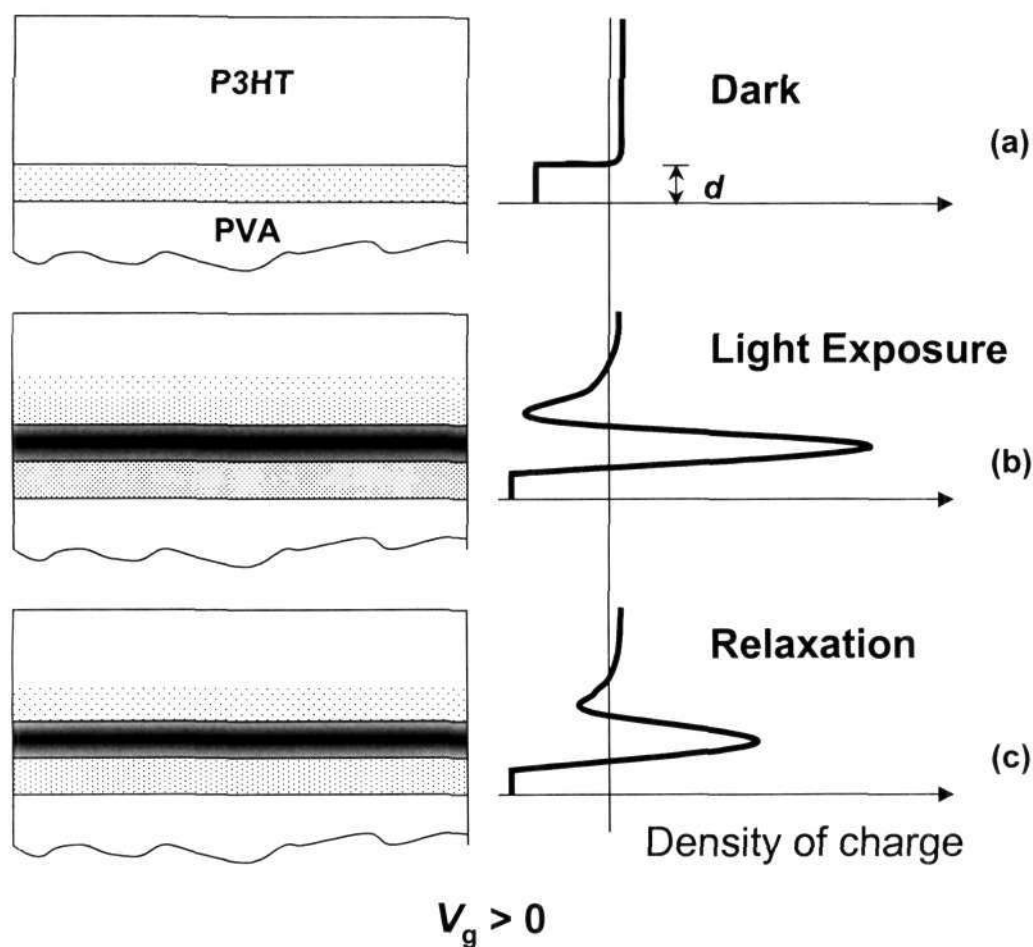


**Fig. 5.15** Schematic of charge density profile inside the polymer semiconductor with dark (a), light operation (b) and relaxation (c) under depletion mode.

in Fig. 5.15(a). During the photoexcitation process, the charges are generated via different pathways depending on the local field. Upon operating in depletion mode, the holes within the depletion region drift away from the interface under the influence of sizable electric field, whereas the photogenerated electrons are buried within the depletion region (i.e.  $x > d$ , the extent of the depletion width measured from the interface). This is represented by the density profile of holes beyond the depletion region. The charge generation in the bulk is likely to be

independent of gate voltage because of the screening effect. Thus the holes, which are generated in the bulk are likely to move towards the interface finding a minimum-potential route. On the other hand, the corresponding electrons are localized in deep trap sites. This process is similar to the accumulation mode. The hole distribution effectively leads to a pattern where maximum is at a finite distance away from the interface. This situation is almost similar to the accumulation mode. Upon switching off light, the recombination process in the bulk occurs in a manner similar to the accumulation mode. In contrast, the recombination of the electrons in the depletion region is restricted by high field, describing metastable state.

#### 5.4 SUMMARY

The photoinduced transient of PFET, operating under depletion mode, was investigated and novel memory effect was observed at low temperature ( $70\text{ K} < T < 200\text{ K}$ ). The operation of the memory process involved information/input, which can be introduced optically and a process of reading or erasing by electrical control of  $V_g$  in this hybrid memory device. The slow relaxation due to the reduced recombination rate in the high field depleted region was exploited to store the charge for several hours. The features were observed to be independent of light intensity and the duration of the light exposure. The memory effects were minimal at room temperature due to the expeditious recombination rate arising from the thermalization process of trapped electrons. A qualitative interpretation was proposed to speculate the experimental observations. A schematic description of the charge distribution profile was put forward to compare the possible mechanisms involved in the accumulation and depletion modes. The novel features observed in the depleted photo-FET can offer a model device-architecture to obtain an efficient multilevel memory device with decoupled operation of writing and erasing. One would also expect an improved performance, in terms of retention, stability, and operating-voltages upon introducing intentional electron trapping centers in dilute

proportions in the semiconducting polymer matrix along with optimized geometrical parameters.

## **Chapter 6**

### **Photocurrent Spectroscopy in PFET**

#### **6.1 INTRODUCTION**

Intensity modulated photocurrent spectroscopy (IMPS) using lock-in technique is a standard and efficient approach to speculate the photo-physical processes involved in variety of photosensitive devices. The spectral analysis of the photoresponse can provide an in-depth knowledge about the location of photogeneration, built-in field, recombination process, quantum efficiency and many other aspects related to photoinduced processes. The technique has been successfully adopted in organic-based sandwich devices [188] and solar cells [22].

Different pathways of photoinduced charge generation, recombination and charge transport depending on the modes of operation, demand a comprehensive study to locate the origin of the photoinduced processes involved in PFET. The spectral response of photoinduced drain current as a function of the gate voltage, light intensity, temperature, modulating frequency and direction of light exposure was performed with standard spectroscopic analysis of photoinduced drain-source current to extract the spatial information of carrier states. The FET geometry, in the depletion mode, provides the opportunity to probe carrier-generation efficiency at different electric field without issues related to minority carrier injection from the electrodes. The ability to manipulate the light-current/dark-current ratio is one of the most obvious advantages in this device structure in terms of analysis of the results. Electric field induced spectral changes can be directly correlated to excitation energetic in absence of carrier density induced terms such as recombination, diffusion etc.

#### **6.2 SPECTRAL RESPONSE OF PHOTOCURRENT AT LOW TEMPERATURE**



The IMPS was measured using a standard lock-in technique at low temperature ( $T = 100$  K) to study the effect of light more closely. The light was

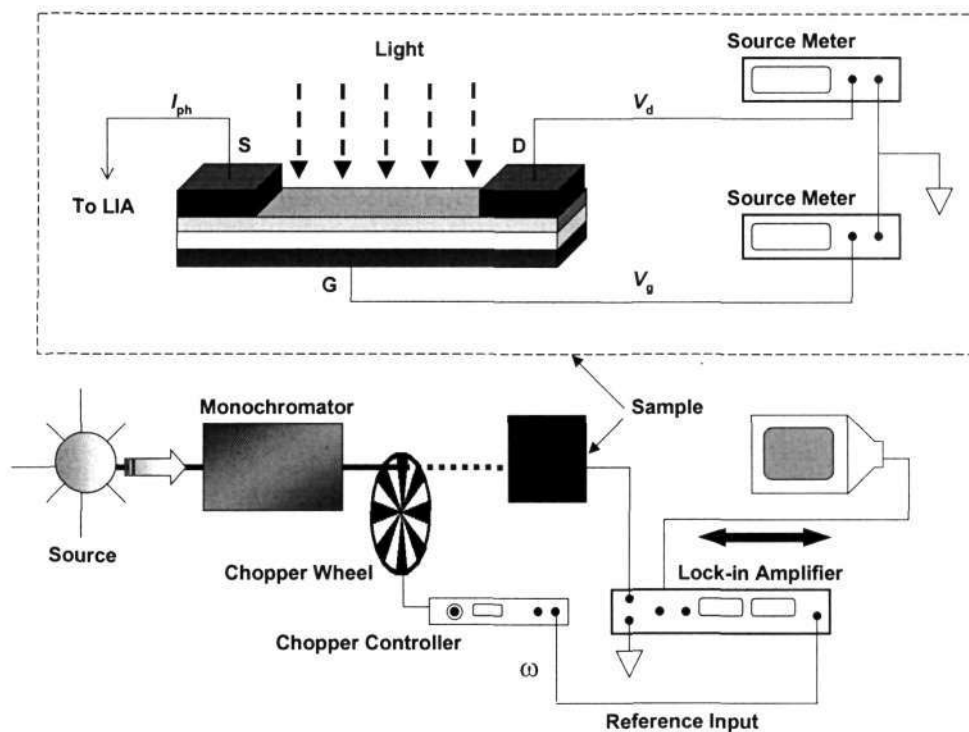


**Fig. 6.1** Experimental set up for intensity modulated photocurrent spectrum of PFET upon top-illumination.

exposed from the top (through P3HT followed by PVA) of the device, as shown in Fig. 6.1 schematically. The photocurrent signal was studied as a function of  $V_g$ , intensity of light and modulating frequencies.

### 6.2.1 Photocurrent Spectrum for Different Gate Bias

The spectral response of drain current  $I_{ph}(\lambda)$  for different modes of operation with modulating frequency  $\omega = 18$  Hz is displayed in Fig. 6.2. The spectral response was observed to follow the absorbance except the appearance of maximum at the band edge wavelength (absorption onset). In this spectral regime with low absorption coefficient  $\alpha(\lambda)$ , the photoactivity was expected to be largely at the interface region. In addition, the light, which was also partially reflected back to the device by the semitransparent gate (Al) electrode, may

enhance the signal corresponding to low absorbing wavelength. The sharp increase at the band-edge was also indicative of the fact that the transport was limited to a very narrow region. A small change of  $I_{ph}(\lambda)$  in the range of 65–45 pA was observed upon changing the gate voltage from  $-100$  V to  $100$  V,

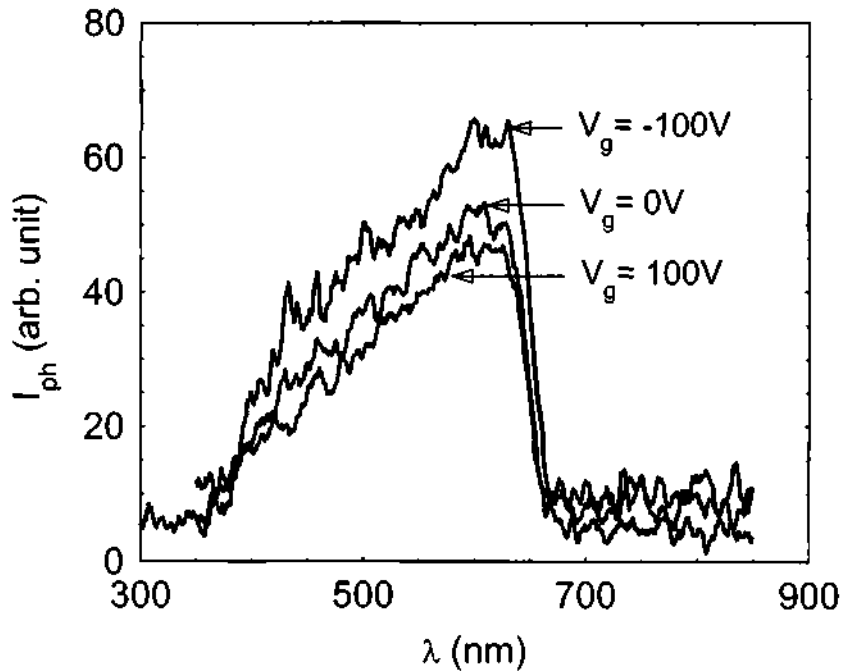
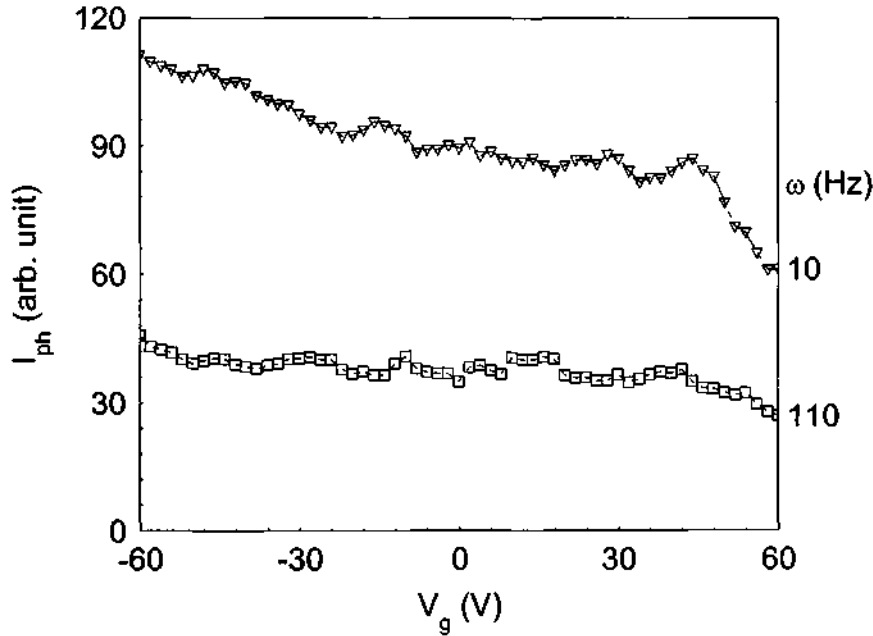


Fig. 6.2 IMPS of PFET for different gate bias at 100 K under  $V_d = -50$  V and modulating frequency  $\omega = 18$  Hz.

maintaining almost identical shape of the spectrum. This emphasizes a discernible impact of gate voltage in photocurrent in consistent with the results discussed in chapter 4. This trend was observed even at higher modulating frequency ( $\omega = 110$  Hz)

The monotonic dependence of  $I_{ph}(\lambda)$  on  $V_g$  was prominently manifested in PFET, as depicted in Fig. 6.3 (for  $\omega = 10$  Hz and 110 Hz). The decrease of  $I_{ph}(\lambda)$  with modulating frequency was also consistent with the slow response of polymer transistor, as mentioned in chapter 4. However, a marginal change of the ratio of  $I_{ph}(\lambda)$  corresponding to the accumulation ( $V_g = -60$  V) and depletion ( $V_g = 60$  V) modes was noticed upon changing the frequency from 10 to 110 Hz. This suggests that the photogeneration of charge carriers in different modes is almost equally influenced by the modulating frequency. In other words, the

normalized  $I_{ph}(\omega)$  is independent of  $V_g$ . The dependence of gate voltage can be attributed to the variation of the parameters like mobility, recombination rate



**Fig. 6.3** Photocurrent signal as a function of  $V_g$  upon exposing light  $\lambda = 630$  nm with modulation  $\omega = 10$  and 110 Hz and  $V_d = -30$  V at 100 K.

and diffusion of the photogenerated charge carriers that are typically influenced by  $V_g$ .

### 6.2.2 Light Intensity Dependence of Modulated Photocurrent

Intensity dependence of photocurrent can provide the information about the nature of recombination process. For example, linear dependence is expected for monomolecular recombination, whereas for bimolecular recombination  $I_{ph}$  is assumed to be proportional to the square root of the light intensity. The plot of photocurrent as a function of intensity for  $\omega = 15$  Hz and 130 Hz in a log-log scale is shown in Fig. 6.4. The device was illuminated at the wavelength  $\lambda = 630$  nm ( $\sim 1.97$  eV) corresponding to the peak of  $I_{ph}(\lambda)$ . The exponent  $\beta$  in  $I_{ph} \sim (\text{Intensity})^\beta$  was observed to be close to unity. This suggests that the fast response is independent of charge density representing the presence of monomolecular recombination in PFET structure. A minor decrease of the exponent from 0.9 to 0.8 was observed upon varying the modulating frequency

from 15 Hz to 130 Hz. Even though the frequency range was limited ( $< 400$

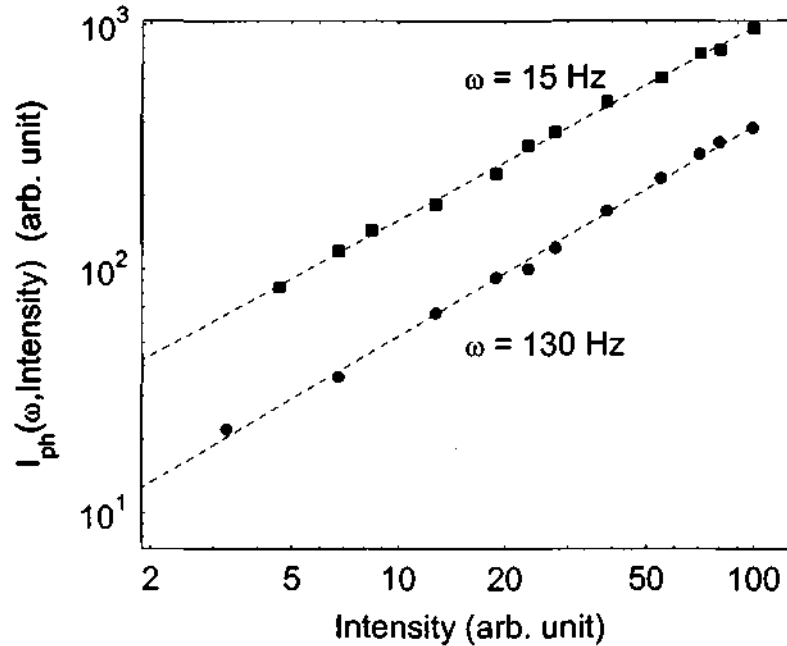


Fig. 6.4 Photocurrent signal versus light intensity ( $\lambda = 630$  nm) for different modulating frequencies under  $V_d = -30$  V,  $V_g = -60$  V at 100 K.

Hz), the dominance of the slow dynamic factors was involved in particular.

### 6.3 SPECTRAL RESPONSE OF PHOTOINDUCED DRAIN CURRENT AT ROOM TEMPERATURE

The spectral feature of photocurrent was observed to change substantially at room temperature. The valuable information regarding the photophysical processes was traced in the spectral feature of  $I_{ph}(\lambda)$ . Typically the temperature-dependent terms like in mobility, photocurrent yield and thermalization of charge carriers can be considered to alter the spectral response at room temperature. The photophysics of PFET was investigated at room temperature to point out the origin of the photogeneration process.

#### 6.3.1 Photoinduced Effect versus Bolometric Effect

An important issue, directing the increase of current as an impact of thermal effect instead of direct photogeneration of charge carriers, is often

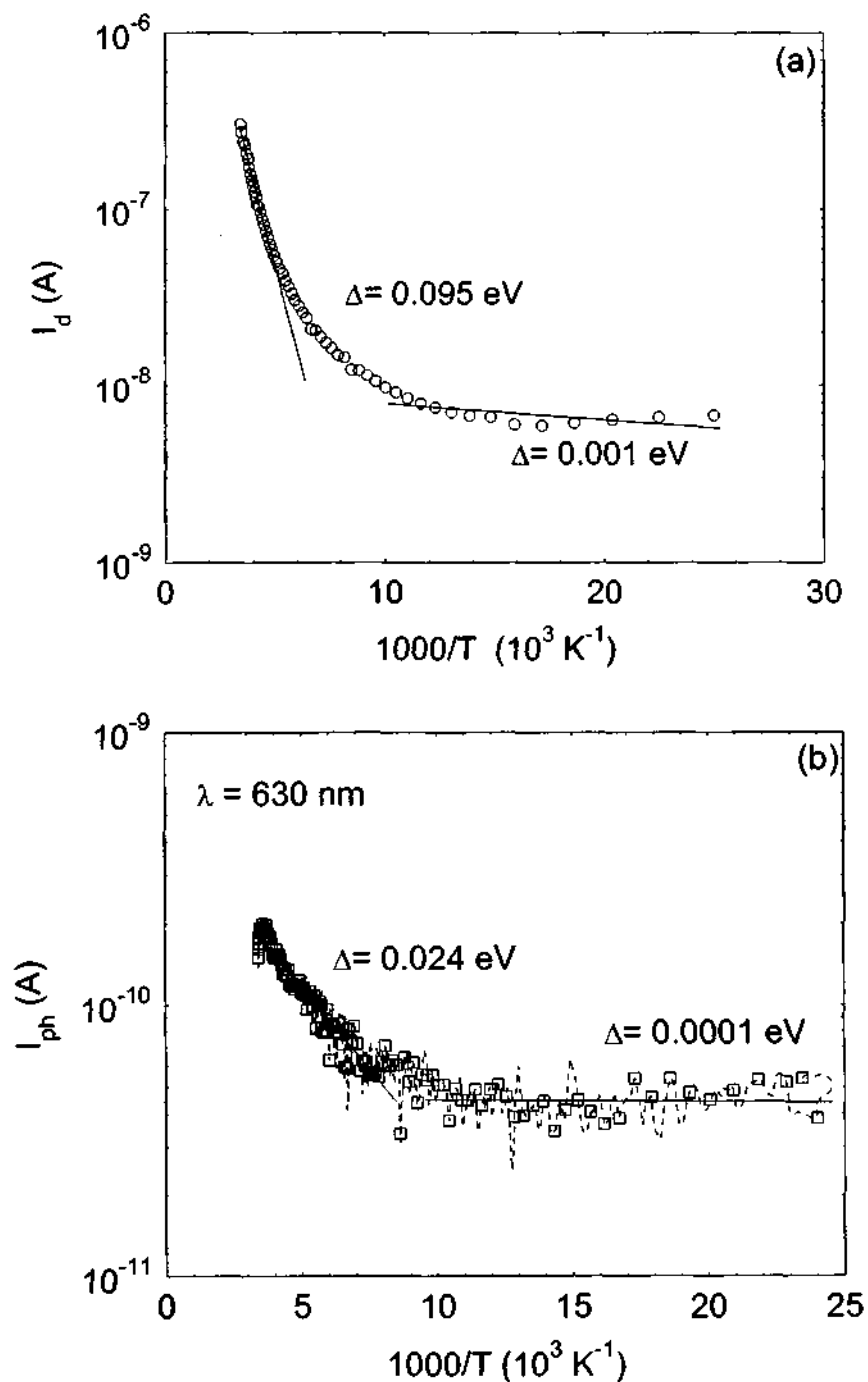


**Fig. 6.5** Arrhenius plot of dark  $I_d$  (a) and photocurrent  $I_{ph}$  (b) upon photoexcitation with  $\lambda = 630 \text{ nm}$  under accumulation mode ( $V_g = -60 \text{ V}$ ,  $V_d = -30 \text{ V}$ ). Every  $10^{\text{th}}$  data points are plotted for clarity.

raised in case of photosensitive semiconductor (bolometric effect) [189] and needs to be addressed here. The appearance of the strong response near the band edge wavelength substantiates the photogeneration of charge carriers rather than the bolometric effect. For bolometric heating, the signal is expected to be approximately proportional to the dark conductivity, which eventually leads to the same activation energy of both the photoconductivity and dark conductivity. The temperature dependence of dark conductivity and that of photoconductivity are illustrated in Fig. 6.5(a) and (b), respectively. In both the cases, the activation energy was observed to vary from low value to a high value (several orders of magnitude) and vice-versa around the temperature  $T = 100$  K. However, the activation energy of photocurrent (0.024 eV) was much lower than that of dark current (0.095 eV). This indeed indicates that the photoinduced effect observed in the present case is genuine and not due to bolometric effect.

### 6.3.2 Photocurrent Spectrum of Top-illuminated Polymer Field-Effect Transistor

The spectral response of photo-FET, which was subjected to photoexcitation from the top with  $\omega = 10$  Hz, is shown in Fig. 6.6. The two

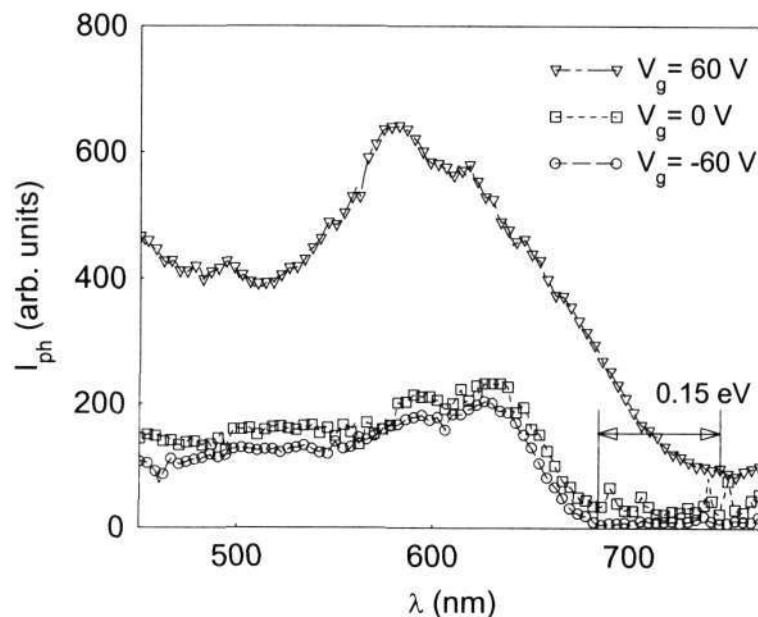


**Fig. 6.6** IMPS at room temperature for various gate voltages under  $V_d = -60$  V. A red shift of 0.15 eV appears in depletion mode.

striking features observed are: (i) higher magnitude of  $I_{ph}(\lambda)$  in depletion mode, (ii) a red shift of the onset of the spectrum corresponding to the depletion mode as compared to the accumulation mode. In depletion mode, the finite value of  $I_{ph}(\lambda)$  below the band edge can be explained in the context of an excitonic framework. The presence of a sizable electric field, associated with the depletion region, can be suggested to be responsible for the dissociation of the photogenerated electron-hole pair. The predomination of field factor for efficient photogeneration of charge carriers was supported by the higher magnitude of  $I_{ph}(\lambda)$  in depletion mode as compared to the accumulation mode. The same argument can explain  $I_{ph}(\lambda)$  under flatband condition ( $V_g = 0$  V) (not shown), which was observed to be almost identical to that of accumulation mode. The decrease of on/off ratio with increasing temperature also invokes that the thermalization of the charge carriers in the depletion mode is more sensitive to temperature than that in the accumulation mode.

The different photoresponse depending on the temperature was also manifested in the light-to-dark  $I_d$ , as shown in Fig. 6.7. The span of dark to light values of  $I_d$ , represented by the bars, under two different gate voltages (different modes) are displayed in Figure 6.7(a). The top and the bottom of each bar indicate the current value under light ( $\lambda = 632.8$  nm) and dark conditions, respectively. The transfer characteristic of the transistor under dark condition is represented by the dashed line. In particular, the photoinduced  $I_d$  was observed to be almost insensitive to the modes of operation. On the other hand, the dark  $I_d$  was observed to be less in depletion mode as compared to that in accumulation mode (normal transistor behavior). The higher light responsivity in depletion as compared to that in accumulation mode can be understood in the context of the observations mentioned above. The reverse nature of photoresponse at low temperature is displayed in Fig. 6.7(b), where the photoinduced  $I_d$  essentially changes with higher degree in the accumulation mode rather than in the depletion mode. It is also essential to comment that upon exposing very high level of light intensity (depending on the device parameters), the similar saturation value of  $I_d$  can be attained even at low

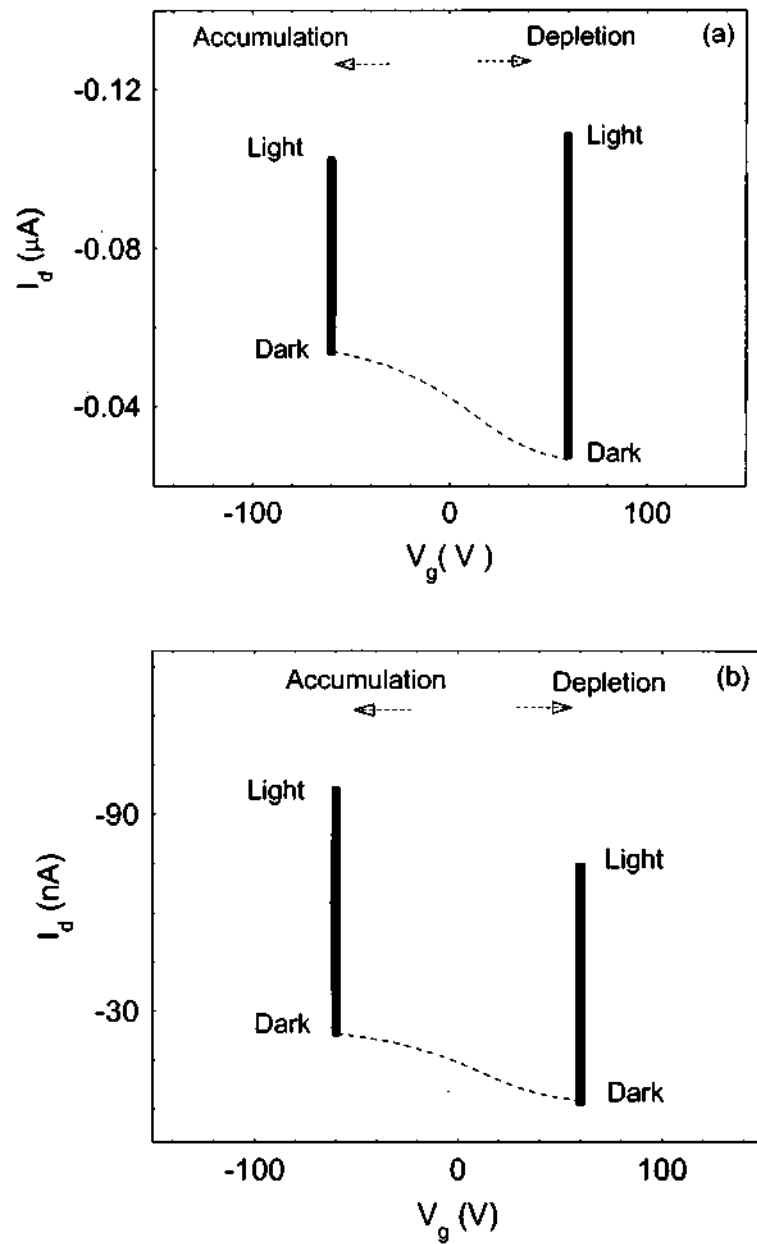


**Fig. 6.7** Bar chart of  $I_d$  for two different gate voltages ( $V_g = 60$  and  $-60$  V) at room temperature (a) and 150 K (b). The bar indicates the range of the  $I_d$  upon irradiation ( $\sim 1$  mW at 630 nm).

temperature. This observation can be attributed to the limitation of doping concentration in the polymer chain.

### 6.3.3 Effect of Modulating Frequency and Gate Voltage on Photocurrent Spectrum



The nature of the photocurrent spectrum was independent of modulating frequency in the range of 10–200 Hz, as depicted in Fig. 6.8 (for  $\omega = 110$  Hz). The magnitude was, however, reduced as compared to the low frequency

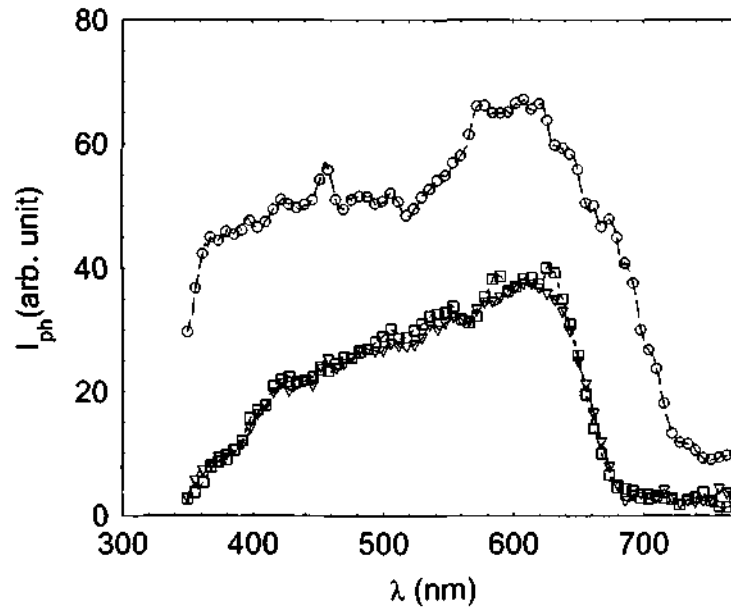
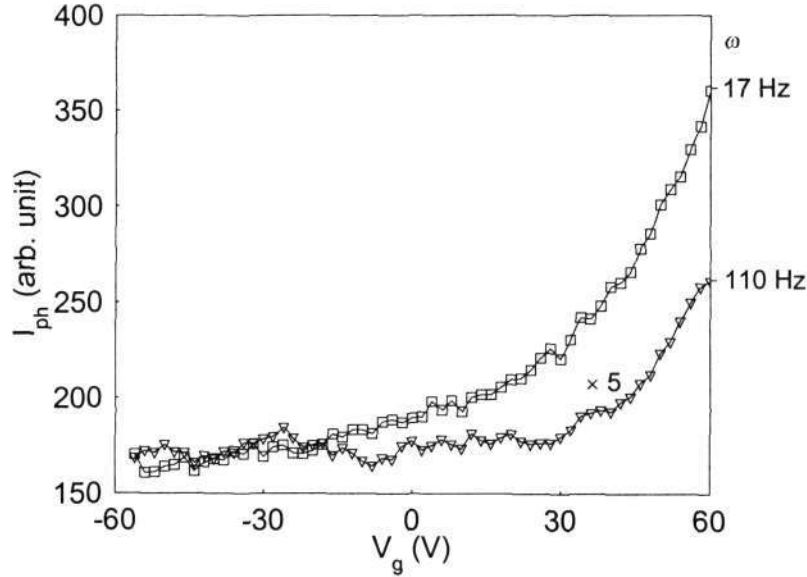


Fig. 6.8 IMPS at room temperature for  $V_g = -60$  ( $\square$ ),  $0$  ( $\nabla$ ),  $60$  V ( $\circ$ ) under  $V_d = -60$  V and  $\omega = 110$  Hz. The spectral shift is independent of the modulating frequency.

counterpart. But the spectral shift ( $\approx 0.15$  eV) between the onsets of  $I_{ph}(\lambda)$  associated with the two modes was indeed unaltered. This emphasizes that the electric field factor associated with the depletion region is responsible for the spectral shift rather than the concentration profile or the dynamical aspects of the excess photogenerated charge carriers. This result also indicates that the photogeneration is effective near the semiconductor-insulator interface and largely to be within/in the vicinity of the depletion region. The magnitude of the shift was strongly reduced with temperature below 100 K. This quenching can be attributed to the lack of thermalization of the excitons to be dissociated to provide excess electron-hole pair. The sizable field arising in the depletion mode is not sufficient enough to dissociate excitons at low temperature, as interpreted using a simplistic Onsager model.

The gate voltage dependence of photocurrent at  $\lambda = 630$  nm was explicitly observed for  $\omega = 17$  Hz and 110 Hz (Fig. 6.9), similar to the result at low

temperature ( $T = 100$  K). But at room temperature, there was a clear asymmetry in the spectral response with respect to the gate voltage unlike the response at



**Fig. 6.9** Photocurrent signal as a function of  $V_g$  for different  $\omega$  (17 and 110 Hz).

low temperature. The field-induced and thermally assisted photogeneration process of charge carriers in the Onsager framework can be used to explain these  $V_g$ -dependent  $I_{ph}(\lambda)$  features.

#### 6.3.4 Photocurrent Spectrum of Bottom-illuminated Polymer Field-Effect Transistor

The spectral feature of PFET, upon photoexcitation from the bottom (i.e. through the semitransparent Al gate), is illustrated in Fig. 6.10. The spectral shift ( $\sim 0.15$  eV) and the amplification of the signal in depletion mode indeed were present in the system, which ensure the field specific properties inherent to the device geometry. The spectral differences between depletion and accumulation modes are highlighted by plotting  $\Delta I_{ph}/I_{ph}(-)$  as function of wavelength ( $\lambda$ ), where  $\Delta I_{ph} = I_{ph}(V_g = 60 \text{ V}) - I_{ph}(V_g = -60 \text{ V})$  and  $I_{ph}(-)$  represents the photocurrent corresponding to  $V_g = -60$  V (dotted line in Fig. 6.10). The red-shift in the photocurrent spectrum in depletion mode was observed more clearly upon comparing  $I_{ph}(V_g = 60 \text{ V})$  and  $I_{ph}(V_g = -60 \text{ V}) \times 5$

in the same scale, as shown in inset of Fig. 6.10. The spectral response of photocurrent under flatband condition ( $V_g = 0$  V) (not shown) was observed to be almost identical to that in accumulation mode, as observed in case of top

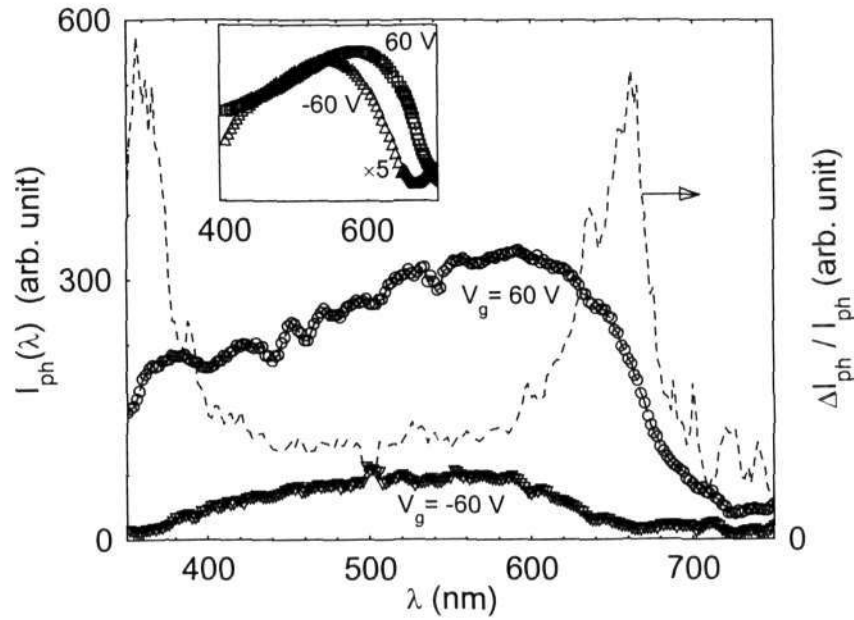


**Fig. 6.10** Room temperature IMPS at different  $V_g$  ( $-60$  and  $60$  V) upon modulating light with  $\omega = 16$  Hz. The difference between the spectrum for different modes is highlighted by plotting  $\Delta I_{ph}[I_{ph}(V_g = 60 \text{ V}) - I_{ph}(V_g = -60 \text{ V})]/I_{ph}(-60 \text{ V})$  as function of wavelength ( $\lambda$ ) (dotted line). Inset is  $I_{ph}(\lambda)$  and drawn on the same scale to compare  $I_{ph}(V_g = 60 \text{ V})$  and  $I_{ph}(V_g = -60 \text{ V}) \times 5$ .

illumination (section 6.3.2). The photoinduced free carrier generation can be generalized to be governed by the following factors: (i) incident light characteristics, (ii) lateral field due to  $V_d$ , (iii)  $V_g$  for  $V_g > 0$  and (iv) secondary effects caused by a vertical charge separation resulting in a built-in field. Consequently the charge transport is controlled by the following factors: (i) mobility, (ii) lateral field due to  $V_d$ , (iii) secondary effects caused by a vertical charge separation resulting in built-in field, and (iv) the number density.

#### 6.4 PHOTOCURRENT SPECTROSCOPY IN TRANSPARENT-GATED PHOTO-FET

The FET structure was modified by replacing aluminum with transparent indium tin oxide (ITO) as the gate electrode to enable comprehensive studies of the photoinduced effect, which was observed to be largely dominated in the

semiconductor-insulator interface. As ITO is transparent in the visible range, reflection of light can be ignored in this configuration. This leads to a model system for understanding the photophysics by exposing light in either direction of the device. The measurement and analysis of the results were used to extract the spatial information of the  $V_g$ -dependent photocarrier generation region.

#### 6.4.1 Photocurrent Spectrum of Transparent PFET for Top-illumination

Spectral features of the transparent PFET upon photoexcitation from the top are displayed in Fig. 6.11. A sharp peak near the band edge was observed in all the curves for different  $V_g$ . This carries the information that the charge

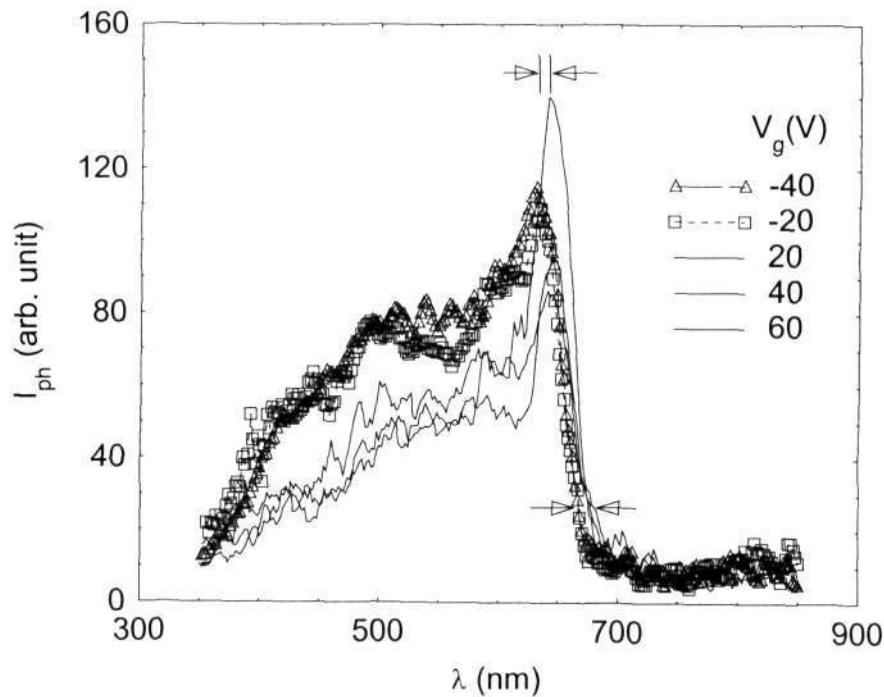
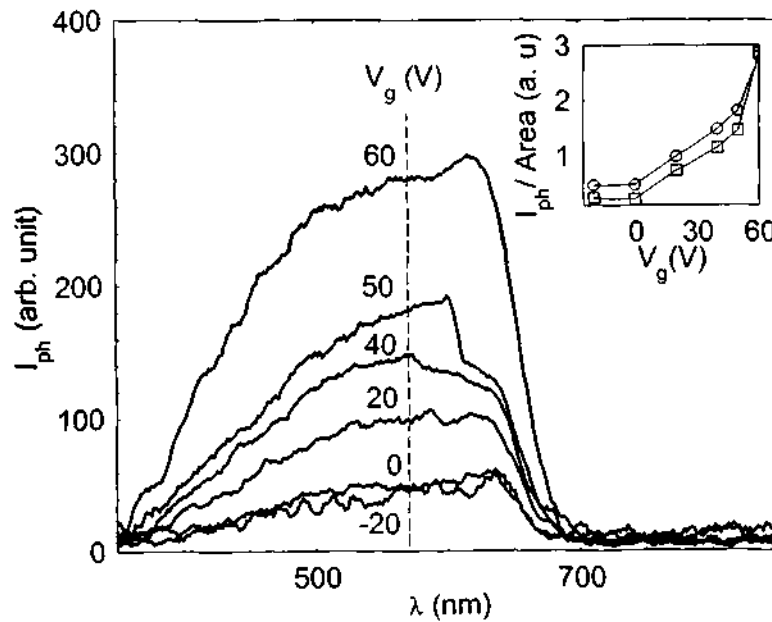


Fig. 6.11  $I_{ph}(\lambda)$  as a function of  $V_g$  for the light incident from the top.

carriers are generated near the interface region making the response at the band edge region higher as compared to that at high absorbing region. A red shift of spectral response corresponding to depletion mode was also identified similar to the Al-gated device. It is to be noted that the amount of shift in ITO-gated FET is less than its Al-gated counterpart, which may be due to the reduction of back reflection in the former.

#### 6.4.2 Photocurrent Spectrum of Transparent PFET for Bottom-illumination

A distinct difference in spectral response was observed upon illuminating the light from the bottom. In this case, a uniform featureless response was observed covering the entire visible region (Fig. 6.12). The nature of the spectrum corresponds to the absorption without showing any explicit maximum near the band edge. The asymmetry, observed in the spectral response



**Fig. 6.12**  $I_{ph}(\lambda)$  as a function of  $V_g$  for the light incident from the bottom. Inset shows  $I_{ph}(\circ)$  at  $\lambda = 570$  nm and the area under the curve ( $\square$ ) with respect to  $V_g$ .

depending on the direction of exposure, can be attributed to the fact that the generation of photoinduced charge carriers is limited to a specific region and not throughout the sample. The increase in magnitude of the photocurrent with  $V_g$  ( $V_g > 0$ ) ensures that the photogeneration is likely to be within the depletion region and the quantum efficiency can be controlled by the field associated with the gate voltage. These spectral properties also suggest that the device can be used as a three-terminal photodetector with a complete control over the responsivity through the gate terminal.

In particular, dark  $I_d$  can be decreased by operating the FET in depletion mode along with a simultaneous-synergistic increase of the modulated

photocurrent. In analogy with the conventional reverse-biased photodiodes, the present device structure can also be understood in the framework of exciton quenching under sizable field ( $> 10^6$  V/cm) associated with the depletion region. But the primary difference is that the light propagation is transverse to the carrier-transport plane in case of PFET, whereas it is in the same direction in case of photodiode. Hence, the process leading to generation and transport in PFET can be decoupled in the first order approximation.

The other plausible sources, such as, field dependent variation of absorption coefficient [106] and interference effects [20] due to reflections at the interfaces, as the primary factors for the spectral features can be ruled out. The change in absorption can be ignored to contribute to the photocurrent since bias dependent change in absorption or transmission was observed to be on the order of 0.01% with a decrease in the absorbance for incident energy beyond 1.9 eV for the depletion mode [106]. However, for further justification, the absorption spectrum of the device was measured for different gate voltages showing no significant differences. In contrast, an increase in the absolute magnitude of  $I_{ph}$  with bias was observed near the band-edge. The contributions from the optical interference effects due to the multiple layers of materials with different dielectric constants ( $V_g$ -independent) is estimated to be not more than 5% and was not substantial enough to modify the  $V_g$ -dependent spectral features.

#### 6.4.3 Estimation of Depletion Width and Associated Electric Field from Spectral Analysis

The photocurrent spectrum of PFET can be analyzed using the rate equation that include the generation, diffusion, recombination and the bimolecular recombination processes as follows

$$\frac{dn(x)}{dt} = \alpha\phi_0\eta \exp(-\alpha x) - D\frac{d^2n(x)}{dx^2} - \frac{n(x)}{\tau} - \gamma n^2(x) \quad (6.1)$$

where  $\alpha$  is the linear absorption coefficient,  $\eta$  the average quantum efficiency,  $\phi_0$  the incident photon flux density per unit area per unit time,  $D$  the diffusion

coefficient,  $\tau$  the average lifetime of the exciton and  $\gamma$  the rate constant of bimolecular recombination. Let us assume that within the depletion region the

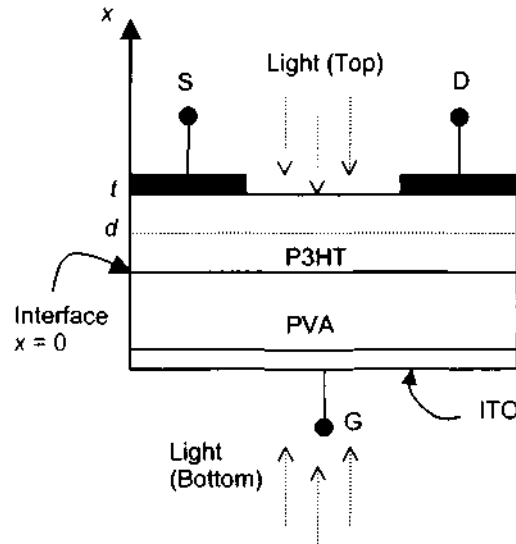


**Fig. 6.13** The schematic of ITO-gated PFET with staggered geometry. The dotted line at  $x = d$  represents the extent of the depletion layer, while  $x = 0$  corresponds to the interface between the insulator and semiconductor.

diffusion can be ignored and there is no bimolecular recombination. At the steady state condition, Eq. 6.1 thus provides the expression for the number of photogenerated charge carriers  $n_{ph} = \eta G \tau$  [50], where the generation rate is the product of  $\alpha(\lambda)$  and  $\phi$ . On the assumption that the charge generation predominantly takes place within the depletion region (active region) i.e.  $\eta \neq 0$  for  $0 \leq x \leq d$  and  $\eta \approx 0$  for  $d \leq x \leq t$  and that  $I_{ph}(\lambda)$  is primarily controlled by the generation process in the regime above the band edge,  $I_{ph}(\lambda)$  can be written in terms of

$$I_{ph}(\lambda) \sim n_{ph}(\lambda) = \alpha(\lambda) \eta \tau \int_{\text{active region}} d\phi(x, \lambda) = \frac{\alpha(\lambda) \eta \tau \lambda}{hc} \int_{\text{active region}} dP(x, \lambda) \quad (6.2)$$

where  $t$  is the thickness of semiconductor and  $d$  is the extent of the depletion region (i.e.  $t-d$  represents the bulk region with residual conductivity, as shown in Fig. 6.13), and  $P$  is the power density per unit area per unit time. One can then express photocurrent for light incident from the two sides as follows:

$$I_{\text{ph}}(\lambda) \sim n_{\text{ph}}(\lambda) = K_{\lambda} (e^{-\alpha_{\lambda}(t-d)} - e^{-\alpha_{\lambda}t}) \quad \text{for light from top} \quad (6.3a)$$

$$= K_{\lambda} (1 - e^{-\alpha_{\lambda}d}) \quad \text{for light from bottom} \quad (6.3b)$$

where,  $K_{\lambda} = (\alpha_{\lambda} \eta \tau \mathcal{N}P_0)/(hc)$  and let  $R = I_{\lambda}/I_{\text{max}}$ , where  $I_{\text{max}}$  represents the current corresponding to the wavelength ( $\lambda \sim 525$  nm) at maximum absorption ( $\alpha_m$ ). It is to be noted that  $I_{\text{max}}$  need not correspond to the maximum value of the current. The ratio of  $R$ -parameter for the light incident from the two sides can be simplified and expressed as:

$$\frac{R_{\text{top}}}{R_{\text{bottom}}} = \exp[(\alpha_m - \alpha_{\lambda})(t - d)] \quad (6.4)$$

This form is useful in extracting the depletion width,  $d$  from the measurements by plotting  $\log(R_{\text{top}}/R_{\text{bottom}})$  against  $\alpha_{\lambda}$ . An estimate of the depletion zone  $d \approx$

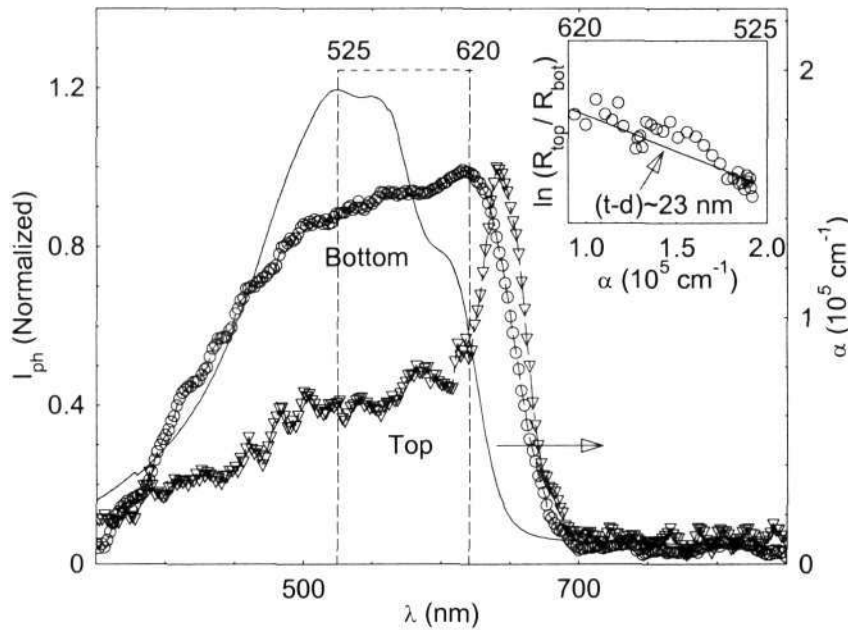


**Fig. 6.14** Normalized  $I_{\text{ph}}(\lambda)$  at  $V_d = -60$  V and  $V_g = 60$  V for light incident from the top (V) and the bottom (O) with absorption spectrum (solid curve) for a device with  $d_{\text{sem}} \approx 200$  nm. Inset shows the plot of  $\ln(R_{\text{top}}/R_{\text{bottom}})$  versus the absorption coefficient  $\alpha$ .

177 nm, is extracted analyzing the experimental results (Fig. 6.14). The charge carrier concentration within the zone of thickness  $t-d \approx 23$  nm is then evaluated using FET characteristics displayed in Fig. 1b, which is  $\sim 10^{16} \text{ cm}^{-3}$ . It is to be



noted that this model does not take into account the transverse field variation, which is expected since the degree of structural-electronic order reduces beyond few layers along with the appearance of deeper trap-sites. The model also does not take exciton diffusion and the geometrical factors i.e. from drain-source electrode placement in the top contact configuration. However, the analysis provides an insight into the primary processes that are active in the depletion mode of the device.

The electric field associated with the depletion width (estimated  $\sim 180$  nm), which is essentially responsible for photogeneration of charge carriers, can be easily calculated in the present case. In particular, the effective capacitance of the system is given by  $1/C_{\text{eff}} = 1/C_{\text{PVA}} + 1/C_{\text{dep}}$  and the voltage across the

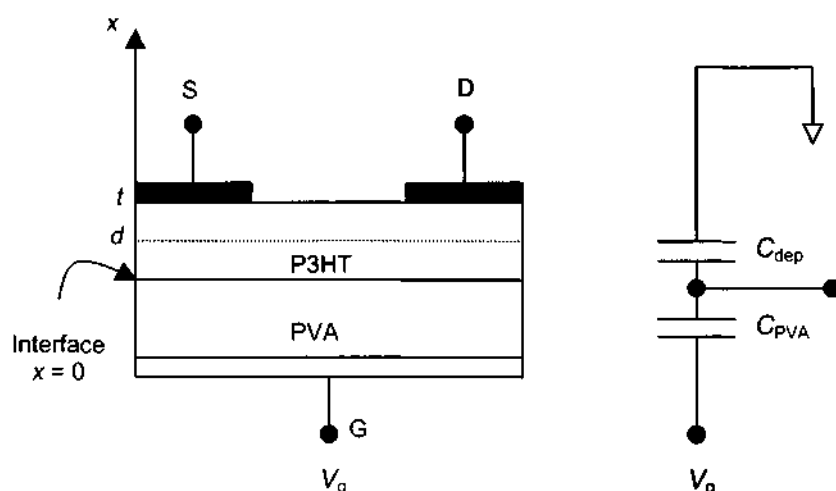


**Fig. 6.15** Schematic of P3HT-based FET and the equivalent circuit.

depleted region can be expressed as  $V_{\text{dep}} = (C_{\text{eff}} \times V_g)/C_{\text{dep}}$ , following the equivalent circuit shown in Fig. 6.15. Using the following parameters  $d_{\text{PVA}} \approx 600$  nm,  $d_{\text{dep}} \approx 180$  nm,  $\epsilon_{\text{PVA}} \approx 8$  [169],  $\epsilon_{\text{P3HT}} \approx 3.2$  [190], one gets  $V_{\text{dep}} \approx 25$  V for  $V_g = 60$  V, and correspondingly the field within the depletion region is  $> 10^6$  V/cm. This is sufficient to dissociate exciton into polarons [20].

#### 6.4.4 Resolved Spectral Features of Photocurrent in Depletion Mode

Substantial spectral features with highly resolved structures were observed in depletion mode of the polymer transistor upon illumination from the top side.

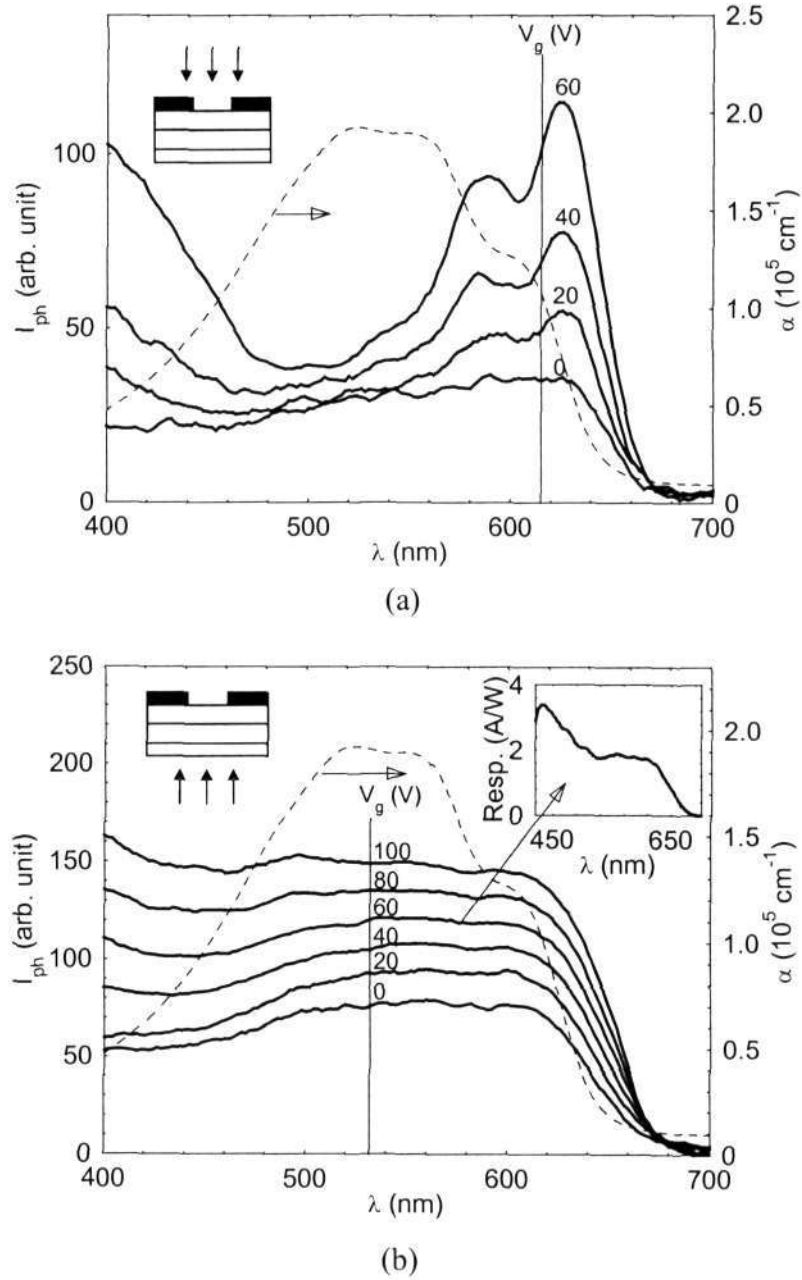


**Fig. 6.16** (a)  $I_{ph}(\lambda)$  as a function of  $V_g$  for the light incident from the top for device  $t \approx 150$  nm. The right ordinate displays for the absorption spectra (dashed line). Inset is the schematic representation of the illumination from the top. (b)  $I_{ph}(\lambda)$  as a function of  $V_g$  with absorption spectra (dashed line). Inset (left) shows the schematic representation of bottom illumination; Inset (right) is the responsivity curve corresponding to  $V_g = 60$  V,  $V_d = -60$  V.

The signature of the field at the interface was more evident in the spectral studies carried out upon illuminating from the top, as depicted in Figure 6.16(a). A strong dependence of  $I_{ph}(\lambda)$  on  $V_g$  was observed in low absorption region near the band-edge. The spectral responses were appeared to be more resolved with the increase of  $V_g$ . These features indicate the presence of competing processes contributing to  $I_{ph}(\lambda)$ , and essentially are controlled by  $V_g$  and incident  $\lambda$ . It was also observed that the resolution of these band edge features is also related to the interface quality and was observed only in the devices consisting of higher values of  $\mu$  and on/off ratio and lower thickness of the polymer semiconductor. On the contrary, the structureless spectra were observed upon photoexcitation from the bottom-ITO-electrode side. The responsivity was in the range of 1–10 A/W depending on  $V_g$ , as shown in Fig. 6.16(b).

#### 6.4.5 Simulated Photocurrent Spectrum in Depletion Mode and Analysis

The analysis, which was used to estimate the depletion width, has several limitations. Firstly, the method was adopted in the wavelength range of 525–620 nm and cannot explain the sharp peak near the band edge. Eventually estimated depletion width was observed to decrease with  $V_g$  in the depletion mode. This discrepancy in the model arises due to the assumption of constant quantum efficiency  $\eta$ , which is likely to depend on the position from the insulator-semiconductor interface. The spatial dependence of  $\eta$  may come from the non-uniform field distribution within the depletion region. The efficient way to point out this effect is *device simulation*. The spectral response of drain current was simulated from Eq. 6.2 using MATLAB. The spectrum becomes structure-less with a single value of  $\eta$ , as shown in Figure 6.17 (dashed line). On the other hand, the two characteristic peaks for top-illumination were obtained by considering two different discrete values of  $\eta$  with decreasing order from the interface to the bulk, suggesting non-uniform field distribution within the depletion width (Fig. 6.17). This can be regarded as the unique and efficient method to obtain the field distribution in depletion mode.

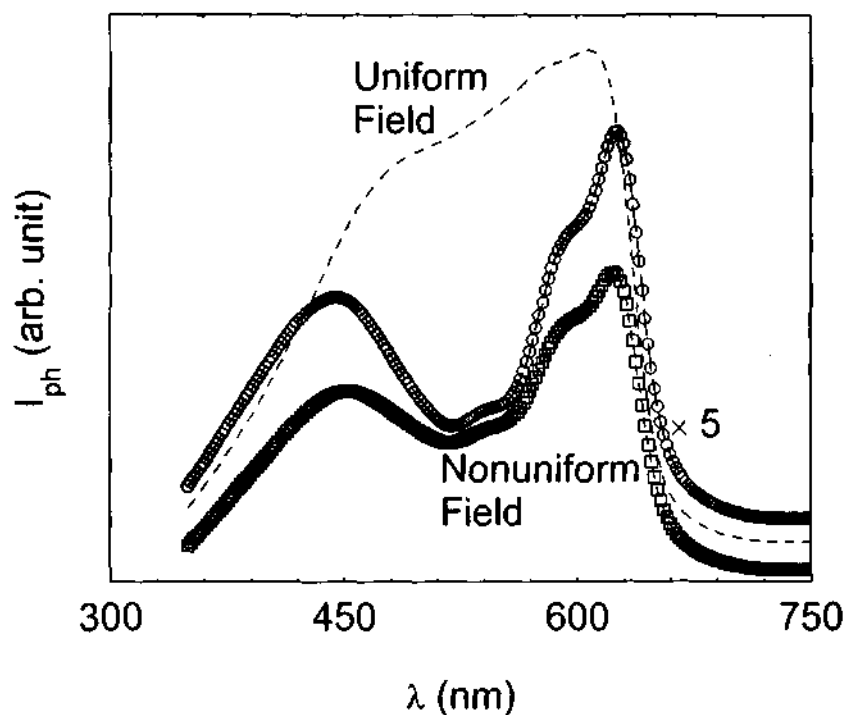


Fig. 6.17 Simulated  $I_{ph}(\lambda)$  for single value of  $\eta$  (dashed line) and two discrete values of  $\eta$  (markers).

### 6.5 SUMMARY

The spectroscopic study of photoinduced drain current was carried out to obtain a detailed understanding of the origin of photoinduced charge generation. Spectroscopic signature of photoinduced charge carrier and the influence of  $V_g$  on photocurrent were prominent at room temperature. The distinct spectral shift of the onset of  $I_{ph}(\lambda)$  along with significant magnification of the magnitude in depletion mode was observed. The results were explained in the context of excitonic framework. The asymmetry in charge distribution depending on  $V_g$  and its impact on the photogeneration were explicitly observed in transparent ITO-gated PFET upon photoexcitation from either side of the device, operated in depletion mode. The spectroscopic analysis was used to extract the extent of the depletion width in a novel manner. The flat spectrum over the entire visible range for the bottom illumination provided the possibility of a photodetector with voltage-controlled photoresponsibility. Finally, further investigation on the spectral pattern using device simulation showed the signature of the non-

uniform field distribution within the depletion region. A comprehensive drift-diffusion model with self-consistent protocol can give better knowledge of the field distribution inside the device.

## Chapter 7

### Summary and Future Directions

Measurements, results and analysis of photoinduced effects in PFET have been studied thoroughly in the present thesis. The overall results and the relevant remarks on the photogeneration of charge carriers, their recombination and the electrical transport properties as a function of gate bias can be summarized as follows:

The slow relaxation of photoinduced charge carriers was observed in poly(3-hexylthiophene)-based FETs after terminating the light source. The dynamics of the photoinduced drain current ( $I_d^{\text{light}}$ ) in the device, operated in the accumulation mode, was completely traced at low temperature (100 K). Several possible models representing the observed results were discussed in detail. The decay of  $I_d^{\text{light}}$  over a longer time scale of several hours was primarily fitted to typical Kohlrausch's law (stretched exponential decay law). But the inconsistency in the fitting parameters led to look for more powerful and appropriate model. The model, based on the spatial separation of charge carriers following serial relaxation due to hierarchy of the system, was adopted to interpret slow dynamics of the photoinduced charge carriers. In the context of this model, the spatially separated positive (hole) and negative (electron) charge carriers were assumed to follow different routes after photogeneration. Upon termination of light, the decay dynamics was completely dictated by the distribution of less mobile electrons, which were trapped in the bulk. On the contrary, the mobile holes contributed to the persistent photocurrent in the device. The model was further modified by using gradually decreasing electron distribution within the bulk. The experimental curves were fitted to this model consistently over the entire range of time scale.

A different relaxation behavior of photoinduced drain current was observed in the depletion mode. Upon termination of illumination, the current decayed from 10 nA to 3 nA and persisted for several hours showing apparent

metastable state at  $V_g = 60$  V. The initial dark state (0.5 nA) was recovered by applying a gate pulse of  $-60$  V for 15 sec followed by the reversal of  $V_g$  back to 60 V. These features can be regarded as memory effect with definite writing, storing, reading and erasing operations. The metastable state was observed to be independent of light intensity and the duration of exposure. A qualitative interpretation was produced to explain the memory effect. In particular, the photogenerated holes were likely to drift away from interface by the sizable electric field associated with depletion width. On the other hand the electrons got trapped within the depletion region. The high electric field in the depletion region opposed the holes to recombine with the trapped electrons restricting current in the metastable state after terminating light source. The equilibrium dark state was recovered by turning the device into the accumulation mode to expedite the recombination process. But the memory effect was not observed at room temperature due to the thermalization of the trapped electrons, which in turn enhances the recombination rate.

The unique combination of light and gate bias as the controlling parameters for the charge transport property was studied using intensity modulated photocurrent spectroscopy (IMPS). The effect of light and  $V_g$  to manipulate the photogeneration and consequently the transportation of charge carriers was observed to be more evident at room temperature. The spectral shift of the onset of the photoinduced drain current  $I_{ph}(\lambda)$  accompanied by a significant increase in the magnitude of  $I_{ph}(\lambda)$  was observed in IMPS under the depletion mode. The results were discussed in terms of excitonic framework following the Onsager theory. The spatial information of photogeneration of charge carriers was traced in ITO-gated PFET using photoexcitation through either side of the device. The photoinduced charge carriers were predominantly generated near the interface in association with the high electric field. The standard spectral analysis was employed to extract the extent of the depletion width, which was estimated approximately 180 nm for a transistor with 200 nm layer of P3HT. Further analysis of the spectral features using device simulation provided the signature of the non-uniform field distribution within the depletion region.

The photoinduced processes investigated in this thesis can be further taken up to understand and quantify the photophysical and the electrical transport processes in PFET. In this context, the primary observation can be the effect of overlapping between the gate and the drain/source in deciding the photogeneration and the recombination processes. The major findings of this thesis work related to the interaction of light with the field in the FET structure can be used to probe the distribution of the charge and the field with more precise resolution. For example, the field profile along the vertical direction is a challenging problem, which would essentially be carried out by solving Poisson's equation and Boltzman transport equation in a self-consistent manner. The field profile along the channel, which has already been investigated by different techniques, can be further verified by scanning light along the channel region. Moreover, the scanning of light source with different polarizations can add more information about photoinduced transport processes in this device architecture. It is noteworthy to mention in this aspect that the recombination process along the channel region has become an important issue after the invention light emitting FET, where the position of the recombination zone was altered depending on gate bias. Those features can be understood in more detail by projecting light spot in different positions of the channel and monitoring the corresponding photoinduced current. This study can be further improved using more powerful technique like far-field and near-field scanning optical microscopy. From the angle of application perspective, the photoresponsivity can essentially be improved by introducing a top gate structure to define the region of photogeneration with better control.





---

## Bibliography

- [1] A. J. Heeger, *Rev. Mod. Phys.* **73**, 681 (2001).
- [2] A. G. Macdiarmid, *Rev. Mod. Phys.* **73**, 701 (2001).
- [3] H. Shirakawa, *Rev. Mod. Phys.* **73**, 713 (2001).
- [4] T. A. Skotheim, *Handbook of Conducting Polymers* (New York: Marcel Dekker) Vol. I and Vol. II (1986).
- [5] J. H. Edwards and W. J. Feast, *Polymer Commun.* **21**, 595 (1980).
- [6] F. Garnier and G. Horowitz, *Synth. Met* **18**, 693 (1987).
- [7] C. W. Tang, *Appl. Phys. Lett.* **48**, 183 (1986).
- [8] J. H. Burroughes, D. D. C. Bradley, A. R. Brown, R. N. Marks, K. Mackay, R. H. Friend, P. L. Burn, and A. B. Holmes, *Nature* **347**, 539 (1990).
- [9] F. Ebisawa, T. Kurokawa, and S. Nara, *J. Appl. Phys.* **54**, 3255 (1983).
- [10] A. Tsumara, H. Koezuka, and T. Ando, *Appl. Phys. Lett.* **49**, 1210 (1986).
- [11] J. H. Burroughes, C. A. Jones and R. H. Friend, *Nature* **335**, 137 (1988).
- [12] R. H. Friend, R. W. Gymer, A. B. Holmes, J. H. Burroughes, R. N. Marks, C. Taliani, D. D. C. Bradley, D. A. Dos Santos, J. L. Brédas, M. Lögdlund, and W. R. Salaneck, *Nature* **397**, 121 (1999).
- [13] C. D. Dimitrakopoulos and D. J. Mascaró, *IBM J. Res. Dev.* **45**, 11 (2001).
- [14] A. Dodabalapur, Z. Bao, A. Makhija, J. G. Laquindanum, V. R. Raju, Y. Feng, H. E. Katz, and J. Rogers, *Appl. Phys. Lett.* **73**, 142 (1998).
- [15] H. Sirringhaus, N. Tessler, and R. H. Friend, *Science* **280**, 1741 (1998).

- [16] Z. L. Li, S. C. Yang, H. F. Meng, Y. S. Chen, Y. Z. Yang, C. H. Liu, S. F. Horng, C. S. Hsu, L. C. Chen, J. P. Hu, and R. H. Lee, *Appl. Phys. Lett.* **84**, 3558 (2004).
- [17] G. Yu, K. Pakbaz, and A. J. Heeger, *Appl. Phys. Lett.* **64**, 3422 (1994).
- [18] G. Yu, J. Wang, J. McElvain, and A. J. Heeger, *Adv. Mat.* **10**, 1431 (1998).
- [19] G. Yu, G. Srdanov, J. Wang, H. Wang, Y. Cao, A. J. Heeger, *Synth. Met.* **111-112**, 133 (2000).
- [20] P. Peumans, A. Yakimov, and S. R. Forrest, *J. Appl. Phys.* **93**, 3693 (2003).
- [21] G. Yu, J. Gao, J. C. Hummelen, F. Wudl, and A. J. Heeger, *Science* **270**, 1789 (1995).
- [22] C. Winder and N. S. Sariciftci, *J. Mater. Chem.* **14**, 1077 (2004).
- [23] C. J. Drury, C. M. J. Mutsaers, C. M. Hart, M. Matters, and D. M. de Leeuw, *Appl. Phys. Lett.* **73**, 108 (1998).
- [24] F. Garnier, R. Hajlaoui, A. Yassar, and P. Srivastava, *Science* **265**, 1648 (1994).
- [25] Z. Bao, Y. Feng, A. Dodabalapur, V. R. Raju, and A. J. Lovinger, *Chem. Mater.* **9**, 1299 (1997).
- [26] A. Hepp, H. Heil, W. Weise, M. Ahles, R. Schmechel, and H. V. Seggern, *Phys. Rev. Lett.* **91**, 157406 (2003).
- [27] H. E. Katz, X. M. Hong, A. Dodabalapur, and R. Sarpeshkar, *J. Appl. Phys.* **91**, 1572 (2002).
- [28] B. Crone, A. Dodabalapur, A. Gelperin, L. Torsi, H. E. Katz, A. J. Lovinger, and Z. Bao, *Appl. Phys. Lett.* **78**, 2229 (2001).
- [29] H. Morkoc, *Advanced Semiconductor and Organic Nano-Techniques* (Academic Press) Part II (2003).
- [30] R. Peierls, *Quantum Theory of Solids* (Clarendon, Oxford 1955).
- [31] A. J. Heeger, S. Kivelson, J. R. Schrieffer, and W. P. Su, *Rev. Mod. Phys.* **60**, 781 (1988).

- 
- [32] W. P. Su, J. R. Schrieffer, and A. J. Heeger, *Phys. Rev. Lett.*, **42**, 1698 (1979).
- [33] W. P. Su, J. R. Schrieffer, and A. J. Heeger *Phys. Rev. B* **22**, 2099 (1980).
- [34] W. P. Su and J. R. Schrieffer, *Proc. Natl. Acad. Sci. USA*, **77**, 5626 (1980).
- [35] J. L. Brédas, R. R. Chance, and R. Silbey, *Mol. Cryst. Liq. Cryst.*, **77**, 319 (1981).
- [36] B. R. Weinberger, J. Kaufer, A. J. Heeger, A. Pron, and A. G. MacDiarmid, *J. Chem. Phys.* **72**, 4749 (1980).
- [37] A. Miller and E. Abrahams, *Phys. Rev.* **120**, 745 (1960).
- [38] N. F. Mott and E. A. Davis, *Electronic Processes in Non-Crystalline Materials*, (Oxford: Clarendon Press) 2<sup>nd</sup> Ed. (1979).
- [39] P. Sheng, *Phys. Rev. B* **21**, 2180 (1980).
- [40] K. Ehinger and S. Roth, *Phil. Mag. B* **53**, 301 (1986).
- [41] A. L. Efros and B. I. Shklovskii, *J. Phys. Chem* **8**, L49 (1975).
- [42] B. I. Shklovskii and A. L. Efros, *Electron Properties of Doped Semiconductors*, (Springer-Verlag, Heidelberg) (1984).
- [43] H. Bässler, *Phys. Status Solidi (b)* **175**, 15 (1993).
- [44] V. I. Arkhipov, P. Heremans, E. V. Emelianova, G. J. Adriaenssens, and H. Bässler, *J. Phys.: Condens. Matter* **14**, 9899 (2002).
- [45] D. H. Dunlap, P. E. Parris, and V. M. Kenkre, *Phys. Rev. Lett.* **77**, 542 (1996).
- [46] S. D. Baranovskii, H. Cordes, F. Hensel, and G. Leising, *Phys. Rev. B* **62**, 13081 (1998).
- [47] J. Frenkel, *Phys. Rev.* **54**, 647 (1938).
- [48] D. A. Vermilyea, *Acta. Metall.* **2**, 346 (1954).
- [49] N. F. Mott and R. W. Gurney, *Electronic Processes in Ionic Crystals* (London: Oxford University Press) (1940).
- [50] C. H. Lee, G. Yu, and A. J. Heeger, *Phys. Rev. B* **47**, 15543 (1993).

- [51] T. W. Hagler, K. Pakbaz, and A. J. Heeger, *Phys. Rev. B* **49**, 10968 (1994).
- [52] I. H. Campbell, T. W. Hagler, D. L. Smith, and J. P. Ferraris, *Phys. Rev. Lett.* **76**, 1900 (1996).
- [53] E. A. Silinsh and V. Čápek, *Organic Molecular Crystals* (American Institute of Physics, New York) (1994).
- [54] L. Onsager, *J. Chem. Phys.* **2**, 599 (1934).
- [55] L. Onsager, *Phys. Rev.* **54**, 554 (1938).
- [56] Z. D. Popovic and J. H. Sharp, *J. Chem. Phys.* **66**, 5076 (1977).
- [57] J. Noolandi and K. M. Hong, *J. Chem. Phys.* **70**, 3230 (1979).
- [58] J. Merski and C. J. Eckhardt, *J. Chem. Phys.* **75**, 3705 (1981).
- [59] J. Merski and C. J. Eckhardt, *J. Chem. Phys.* **75**, 3731 (1981).
- [60] H. Antoniadis, B. R. Hsieh, M. A. Abkowitz, S. A. Jenehke, and M. Stolka, *Synth. Met.* **62**, 265 (1994).
- [61] C. J. Brabec, G. Zerza, G. Cerullo, S. De Silvestri, S. Luzzati, J. C. Hummelen, and S. Sariciftci, *Chem. Phys. Lett.* **340**, 232 (2001).
- [62] C. J. Brabec, N. S. Sariciftci, and J. C. Hummelen, *Adv. Func. Mat.* **11**, 15 (2001).
- [63] N. S. Sariciftci, L. Smilowitz, A. J. Heeger, F. Wudl, *Science* **258**, 1474 (1992).
- [64] S. R. Forrest, *MRS Bull.* **30**, 28 (2005).
- [65] J. Xue, S. Uchida, B. P. Rand, and S. R. Forrest, *Appl. Phys. Lett.* **86**, 5757 (2005).
- [66] M. R. Reyes, K. Kim, and D. L. Carroll, *Appl. Phys. Lett.* **87**, 083506 (2005).
- [67] C. W. Tang and S. A. V. Slyke, *Appl. Phys. Lett.* **51**, 913 (1987).
- [68] H. S. Nalwa and L. S. Rohwer, *Handbook of Luminescence, Display materials and Devices, ORGANIC LIGHT-EMITTING DEVICES* (American Scientific Publishers, California, USA) Vol. 1 (2003) [references therein].

- [69] N. C. Greenham, S. C. Moratti, D. D. C. Bradley, R. H. Friend, and A. B. Holmes, *Nature* **365**, 628 (1993).
- [70] J. S. Wilson, A. S. Dhoot, A. J. A. B. Seeley, M. S. Khan, A. Köhler, and R. H. Friend, *Nature* **413**, 828 (2001).
- [71] C. W. Tang and S. A. V. Slyke, C. H. Chen, *J. Appl. Phys.* **65**, 3610 (1989).
- [72] M. A. Baldo, D. F. O'Brien, Y. You, A. Shoustikov, S. Sibley, M. E. Thompson, and S. R. Forrest, *Nature* **395**, 151 (1998).
- [73] K. Ziemelis, *Nature* **399**, 408 (1999).
- [74] U. Mitschke and P. Baeuerle, *J. Mater. Chem.*, **10**, 1471 (2000) [references therein].
- [75] J. E. Lilienfeld, US Patent 1745175 (1930).
- [76] S. M. Sze, *Physics of Semiconductor Devices* (John Wiley, New York) (1981).
- [77] P. K. Weimer, *Proc. IRE* **50**, 1462 (1962).
- [78] J. Kanicki, *Amorphous & Microcrystalline Semiconductor Devices: Materials and Device Physics* (Artech House, Boston) (1992).
- [79] C. Rost, D. J. Gundlach, S. Karg, and W. Rieb, *J. Appl. Phys.* **95**, 5782 (2004).
- [80] L. L. Chua, J. Zaumseil, J. F. Chang, E. C. W. Ou, P. K. H. Ho, H. Sirringhaus, and R. H. Friend, *Nature* **434**, 194 (2005).
- [81] K. S. Narayan and N. Kumar, *Appl. Phys. Lett.* **79**, 1891 (2001).
- [82] D. F. Barbe and C. R. Westgate, *J. Phys. Chem. Solids* **31**, 2679 (1970).
- [83] H. Koezuka, A. Tsumura, and T. Ando, *Synth. Met.* **18**, 699 (1987).
- [84] A. Tsumura, H. Koezuka, and T. Ando, *Synth. Met.* **25**, 11 (1988).
- [85] C. Clarisse, M. T. Riou, M. Gauneau, and M. L. Contellec, *Electron. Lett.* **24**, 674 (1988).
- [86] G. Horowitz, D. Fichou, X. Peng, Z. Xu, and F. Garnier, *Solid State Comm.* **72**, 381 (1989).

- [87] K. E. Ziemelis, A. T. Hussain, D. D. C. Bradley, R. H. Friend, J. R uhe, and G. Wegner, *Synth. Met.* **41**, 1045 (1991).
- [88] G. Horowitz, *Adv. Mat.* **10**, 365 (1998).
- [89] F. Garnier, G. Horowitz, D. Fitchou, and X. Peng in *Science and Applications of Conducting Polymers*, edited by W. R. Salaneck, D. T. Clark, and E. J. Samuelsen (Adam Hilger, USA) (1990).
- [90] G. Horowitz in *Semiconducting Polymers*, edited by G. Hadziioannou and P. F. van Hutten (Wiley-VCH) (1999).
- [91] A. R. Brown, D. M. de Leeuw, E. E. Havinga, and A. Pomp, *Synth. Met.* **68**, 65 (1994).
- [92] A. R. Brown, C. P. Jarrett, D. M. de Leeuw, and M. Matters, *Synth. Met.* **88**, 37 (1997).
- [93] G. Paasch, T. Lindner, and S. Scheinert, *Synth. Met.* **132**, 97 (2002).
- [94] G. Horowitz, R. Hajlaoui, H. Bouchriha, R. Bourguiga, and M. Hajlaoui, *Adv. Mat.* **10**, 923 (1998).
- [95] G. Horowitz, M. E. Hajlaoui, and R. Hajlaoui, *J. Appl. Phys.* **87**, 4456 (2000).
- [96] E. J. Meijer, C. Tanase, P. W. M. Blom, E. van Veenendaal, B. H. Huisman, D. M. de Leeuw, and T. M. Klapwijk, *Appl. Phys. Lett.* **20**, 3838 (2002).
- [97] E. J. Meijer, C. Detcheverry, P. J. Baesjou, E. van Veenendaal, D. M. de Leeuw, and T. M. Klapwijk, *J. Appl. Phys.* **93**, 4831 (2003).
- [98] M. Shur, *Physics of Semiconductor Devices*, (Prentice-Hall, Englewood Cliffs) (1990).
- [99] G. Horowitz and P. Delannoy, *J. Appl. Phys.* **70**, 469 (1991).
- [100] G. Horowitz, R. Hajlaoui, P. Delannoy, *J. Phys. III (Paris)* **5**, 355 (1995).
- [101] G. Horowitz, R. Hajlaoui, D. Fichou, and A. E. Kassmi, *J. Appl. Phys.* **85**, 3202 (1999).
- [102] M. C. J. M. Vissenberg and M. Matters, *Phys. Rev. B* **57**, 12964 (1998).

- 
- [103] P. Stallinga, H. L. Gomes, F. Biscarini, M. Murgia, and D. M. de Leeuw, *J. Appl. Phys.* **96**, 5277 (2004).
- [104] R. H. Friend, J. H. Burroughes, and K. E. Ziemelis in *Science and Applications of Conducting Polymers*, edited by W. R. Salaneck, D. T. Clark, and E. J. Samuelsen (Adam Hilger, USA) (1990).
- [105] K. E. Ziemelis, A. T. Hussain, D. D. C. Bradley, R. H. Friend, J. R u he, and G. Wegner, *Phys. Rev. Lett.* **66**, 2231 (1991).
- [106] P. J. Brown, H. Sirringhaus, M. Harrison, M. Shkunov, and R. H. Friend, *Phys. Rev. B* **63**, 125204 (2001).
- [107] K. Marumoto, Y. Muramatsu, S. Ukai, H. Ito, and S. Kuroda, *Synth. Met.* **154**, 45 (2005).
- [108] M. Ahles, A. Hepp, R. Schmechel, and H. von Seggern, *Appl. Phys. Lett.* **84**, 428 (2004).
- [109] R. A. Street and A. Salleo, *Appl. Phys. Lett.* **81**, 2887 (2002).
- [110] C. D. Dimitrakopoulos, B. K. Furman, T. Graham, S. Hegde, and S. Purushothaman, *Synth. Met.* **92**, 47 (1998).
- [111] P. R. L. Malenfant, C. D. Dimitrakopoulos, J. D. Geloreme, L. L. Kosbar, T. O. Graham, A. Curioni, and W. Andreoni, *Appl. Phys. Lett.* **80**, 2517 (2002).
- [112] C. D. Dimitrakopoulos, A. R. Brown, and A. R. Brown, and A. Pomp, *J. Appl. Phys.* **80**, 2501 (1996).
- [113] Z. Bao, A. Dodabalapur, and A. J. Lovinger, *Appl. Phys. Lett.* **69**, 4108 (1996).
- [114] G. M. Wang, J. Swensen, D. Moses, and A. J. Heeger, *J. Appl. Phys.* **93**, 6137 (2003).
- [115] G. Xu, Z. Bao, and J. T. Groves, *Langmuir* **16**, 1834 (2000).
- [116] M. Willander, A. Assadi, and C. Svensson, *Synth. Met.* **57**, 4099 (1993).
- [117] H. Fuchigami, A. Tsumura, and H. Koezuka, *Appl. Phys. Lett.* **63**, 1372 (1993).



- [118] H. Siringhaus, P. J. Brown, R. H. Friend, M. M. Nielsen, K. Bechgaard, B. M. W. Langeveld-Voss, A. J. H. Spiering, R. A. J. Janssen, E. W. Meijer, P. Herwig, and D. M. de Leeuw, *Nature* **401**, 685 (1999).
- [119] J. Paloheimo, P. Kuivalainen, H. Stubb, E. Vuorimaa, and P. Yli-Lahti, *Appl. Phys. Lett.* **56**, 1157 (1990).
- [120] J. Matsui, S. Yoshida, T. Mikayama, A. Aoki, and T. Miyashita, *Langmuir* **21**, 5343 (2005).
- [121] A. Salleo, M. L. Chabinyc, M. S. Yang, and R. A. Street, *Appl. Phys. Lett.* **81**, 4383 (2002).
- [122] L. L. Chua, P. K. H. Ho, H. Siringhaus, and R. H. Friend, *Adv. Mat.* **16**, 1609 (2004).
- [123] S. Nariola, H. Ishii, D. Yoshimura, M. Sei, Y. Ouchi, K. Seki, S. Hasegawa, T. Miyazaki, Y. Harima, and K. Yamashita, *Appl. Phys. Lett.* **67**, 1899 (1995).
- [124] H. Ishii, and K. Seki, *IEEE Electron Devices* **44**, 1295 (1997).
- [125] I. G. Hill, A. Rajagopal, and A. Kahn, *Appl. Phys. Lett.* **73**, 662 (1998).
- [126] I. G. Hill, J. Schwartz, and A. Kahn, *Org. Electron.* **1**, 5 (2000).
- [127] I. H. Campbell, S. Rubin, T. A. Zawodzinski, J. D. Kress, R. L. Martin, D. L. Smith, N. N. Barashkov, and J. P. Ferraris, *Phys. Rev. B* **54**, 14321 (1996).
- [128] I. H. Campbell, J. D. Kress, R. L. Martin, D. L. Smith, N. N. Barashkov, and J. P. Ferraris, *Appl. Phys. Lett.* **71**, 3528 (1997).
- [129] A. Assadi, C. Svensson, M. Willander, and O. Inganäs, *Appl. Phys. Lett.* **53**, 195 (1988).
- [130] A. Tsumura, H. Fuchigami, and H. Koezuka, *Synth. Met.* **41**, 1181 (1991).
- [131] J. Paloheimo, H. Stubb, P. Yli-Lahti, and P. Kuivalainen, *Synth. Met.* **41-43**, 563 (1991).

- 
- [132] G. Wang, T. Hirasa, D. Moses, and A. J. Heeger, *Synth. Met.* **146**, 127 (2004).
- [133] H. Sirringhaus, R. J. Wilson, R. H. Friend, M. Inbasekaran, W. Wu, E. P. Woo, M. Grell, and D. D. C. Bradley, *Appl. Phys. Lett.* **77**, 406 (2000).
- [134] H. Sirringhaus, T. Kawase, R. H. Friend, T. Shimoda, M. Inbasekaran, W. Wu, and E. P. Woo, *Science* **290**, 2123 (2000).
- [135] H. Akimichi, K. Waragai, S. Hotta, H. Kano, H. Sakati, *Appl. Phys. Lett.* **58**, 1500 (1991).
- [136] F. Garnier, A. Yassar, R. Hajlaoui, G. Horowitz, F. Deloffre, B. Servet, S. Ries, and P. Alnot, *J. Am. Chem. Soc.* **115**, 8716 (1993).
- [137] A. Dodabalapur, L. Torsi, and H. E. Katz, *Science* **268**, 270 (1995).
- [138] G. Horowitz, X. Peng, D. Fichou, and F. Garnier, *Synth. Met.* **51**, 419 (1992).
- [139] A. R. Brown, A. Pomp, C. M. Hart, and D. M. de Leeuw, *Science* **270**, 972 (1995).
- [140] A. J. Salih, J. M. Marshall, and J. M. Maud, *Phil. Mag. Lett.* **75**, 169 (1997).
- [141] Y. Y. Lin, D. J. Gundlach, S. Nelson, and T. N. Jackson, in *54<sup>th</sup> Annual Device Research Conference Digest*, p.80 (1996).
- [142] Y. Y. Lin, D. J. Gundlach, S. Nelson, and T. N. Jackson, *IEEE Electron Device Lett.* **18**, 606 (1997).
- [143] G. Guillaud, M. A. Sadound, and M. Maitrot, *Chem. Phys. Lett.* **167**, 503 (1990).
- [144] R. C. Haddon, A. S. Perel, R. C. Morris, T. T. M. Palstra, A. F. Hebard, and R. M. Fleming, *Appl. Phys. Lett.* **67**, 121 (1995).
- [145] S. Kobayashi, T. Takenobu, S. Mori, S. Fujiwara, and Y. Iwasa, *Appl. Phys. Lett.* **82**, 4581 (2003).
- [146] A. Babel and S. A. Jenekhe, *Adv. Mater.* **14**, 371 (2002).
- [147] A. Babel and S. A. Jenekhe, *J. Am. Chem. Soc.* **125**, 13656 (2003).
- [148] A. Babel and S. A. Jenekhe, *J. Phys. Chem. B* **106**, 6129 (2002).

- [149] C. Waldauf, P. Schilinsky, M. Perisutti, J. Hauch, and C. J. Brabec, *Adv. Mater.* **15**, 2084 (2003).
- [150] A. Dodabalapur., H. E. Katz, , L. Torsi, and R. C. Haddon, *Appl. Phys. Lett.* **68**, 1108 (1996).
- [151] C. Rost, D. J. Gundlach, S. Karg, and W. Rieb, *J. Appl. Phys.* **95**, 5782 (2004).
- [152] E. J. Meijer, D. M. de Leeuw, S. Setayesh, E. van Vessendaal, B. H. Huisman, P.W. M. Blom, J. C. Hummelen, U. Scherf, and T. M. Klapwijk, *Nat. Mater.* **2**, 678 (2003).
- [153] T. D. Anthopoulos, C. Tanase, S. Setayesh, E. J. Meijer, J. C. Hummelen, P. W. M. Blom, and D. M. deLeeuw, *Adv. Mater.* **16**, 2174 (2004).
- [154] T. Yasuda, T. Goto, K. Fujita, and T. Tsutsui, *Appl. Phys. Lett.* **85**, 2098 (2004).
- [155] V. C. Sundar, J. Zaumseil, V. Podzorov, Etienne Menard, R. L. Willett, T. Someya, M. E. Gershenson, J. A. Rogers, *Science* **303**, 1644 (2004).
- [156] H. G. O. Sandberg, T. G. Bäcklund, R. Österbacka, M. Shkunov, D. Sparrowe, I. McCulloh, and H. Stubb, *Organic Electronics* **6**, 142 (2005).
- [157] Y. Zhang, J. R. Petta, S. Ambily, Y. Shen, D. C. Ralph, and G. G. Malliaras, *Adv. Mater.* **15**, 1632 (2003).
- [158] J. Z. Wang, J. F. Chang, and H. Sirringhaus, *Appl. Phys. Lett.* **87**, 083503 (2005).
- [159] A. L. Deman and J. Tardy, *Organic Electronics* **6**, 78 (2005).
- [160] K. Y. Jen, R. Oboodi, and R. L. Elsenbaumer, *Polym. Mater. Sci. Eng.* **53**, 79 (1985).
- [161] R. D. McCullough, *Adv. Mater.* **10**, 93 (1998).
- [162] T. A. Chen, X. Xu, and R. D. Rieke, *J. Am. Chem. Soc.* **117**, 233 (1995).

- [163] T. J. Prosa, M. J. Winokur, J. Moulton, P. Smith, and A. J. Heeger, *Macromolecules* **25**, 4364 (1992).
- [164] D. H. Kim, Y. D. Park, Y. Jang, H. Yang, Y. H. Kim, J. I. Han, D. G. Moon, S. Park, T. Chang, C. Chang, M. Joo, C. Y. Ryu, and K. Cho, *Adv. Func. Mater.* **15**, 77 (2005).
- [165] J. H. Fell, E. J. Samuelsen, J. Als-Nielsen, G. Grübel, and J. Mårdalen, *Solid State Commun.* **94**, 843 (1995).
- [166] S. S. Venkatraman, T. O. Murdock, and S. Pudjijanto, *Pharmaceutical hydrogel formulations, and associated drug delivery devices and methods*, United States Patent 6,039,977 (1997).
- [167] J. Chatterjee, Y. Haik, and C. J. Chen, *BioMagnetic Research and Technology* **2**, 2 (2004).
- [168] M. Lösche, G. Feher, and M. Y. Okamura, *Proc. Nati. Acad. Sci. USA* **84**, 7537 (1987).
- [169] S. Franzen and S. G. Boxer, *J. Phys. Chem.* **97**, 6304 (1993).
- [170] R. H. Wiley, *Ind. Eng. Chem.* **38**, 959 (1946).
- [171] Th. B. Singh, N. Marjanović, G. J. Matt, N. S. Sariciftci, R. Schwödiauer and S. Bauer, *Appl. Phys. Lett.* **85**, 5409 (2004).
- [172] B. D. Vogt, C. L. Soles, H. J. Lee, E. K. Lin, W. Wu, *Polymer* **46**, 1635 (2005).
- [173] W. Pisula, A. Menon, M. Stepputat, I. Lieberwirth, U. Kolb, A. Tracz, H. Sirringhaus, T. Pakula, and K. Müllen, *Adv. Mat.* **17**, 684 (2005).
- [174] B. Dulieu, J. Wéry, S. Lefrant, and J. Bullot, *Phys. Rev. B* **57**, 9118 (1998).
- [175] G. Williams and D. C. Watts, *Trans. Faraday Soc.* **66**, 80 (1970).
- [176] R. G. Palmer, D. L. Stein, E. Abrahams, and P. W. Anderson, *Phys. Rev. Lett.* **53**, 958 (1984).
- [177] H. X. Jiang and J. Y. Lin, *Phys. Rev. Lett.* **64**, 2547 (1990).
- [178] J. Kakalios, R. A. Street, and W. B. Jackson, *Phys. Rev. Lett.* **59**, 1037 (1987).

- [179] B. Sturman, E. Podivilov, and M. Gorkunov, *Phys. Rev. Lett.* **91**, 176602 (2003).
- [180] H. J. Queisser, *Phys. Rev. Lett.* **54**, 234 (1985).
- [181] H. J. Queisser and D. E. Theodorou, *Phys. Rev. B* **33**, 4027 (1986).
- [182] N. A. Schultz, M. C. Scharber, C. J. Brabec, and N. S. Sariciftci, *Phys. Rev. B* **64**, 245210 (2001).
- [183] H. J. Queisser and D. E. Theodorou, *Phys. Rev. Lett.* **43**, 401 (1979).
- [184] Y. Yang, L. Ma, and J. Wu, *MRS Bull.* **29**, 833 (2004) [References therein].
- [185] A. Bandyopadhyay and A.J. Pal, *Appl. Phys. Lett.* **82**, 1215 (2003).
- [186] L. P. Ma, J. Liu, S. M. Pyo, and Y. Yang, *Appl. Phys. Lett.* **80**, 362 (2002).
- [187] V. Podzorov and M. E. Gershenson, *Phys. Rev. Lett.* **95**, 016602 (2005).
- [188] M. G. Harrison, J. Grüner, and G. C. W. Spencer, *Phys. Rev. B* **55**, 7831 (1997).
- [189] T. Tokumoto, J. S. Brooks, R. Clinite, X. Wei, J. E. Anthony, D. L. Eaton, and S. R. Parkin, *J. Appl. Phys.* **92**, 5208 (2002).
- [190] I. Torres, D. M. Taylor, and E. Itoh, *Appl. Phys. Lett.* **85**, 314 (2004).

---

## List of Publications

1. Photocurrent spectroscopy under depletion mode of transparent polymer field effect transistors. S. Dutta and K. S. Narayan (Appl. Phys. Lett. **87**, 193505-1 – 193505-3, 2005).
2. Spectroscopic studies of photoinduced transport in polymer field effect transistors. S. Dutta and K. S. Narayan (Synth. Met. **155**, 328 – 331, 2005).
3. Photoinduced charge transport in polymer field effect transistors. S. Dutta and K. S. Narayan (Synth. Met. **146**, 321 - 324, 2004).
4. Polymer based photodetectors. K. S. Narayan, D. Kabra, and S. Dutta (Mat. Res. Soc. Symp. Proc. Vol. **814**, I13.5.1 – I13.5.9, 2004).
5. Gate voltage control of optically-induced charges and memory effects in polymer field effect transistors. Soumya Dutta and K. S. Narayan (Adv. Mater. **16**, 2151 – 2155, 2004).
6. Nonexponential relaxation of photoinduced conductance in organic field effect transistors. Soumya Dutta and K. S. Narayan (Phys. Rev. B **68**, 125208-1 – 125208-4, 2003).
7. Photoinduced relaxation effects in three-terminal polymer based device structures. S. Dutta, Th. B. Singh, and K. S. Narayan (Synth. Met. **139**, 553 – 556, 2003).
8. Strategies for efficient photo-induced charge separation and transport in Semiconducting Polymer Systems. K. S. Narayan, Th. B. Singh, A. G. Manoj, V. K. Basavaraj, and S. Dutta (Photonics 2002).

621.381 528 4

P06

